INWARD-FLOWING FRACTION OF ABSORBED SOLAR RADIATION FOR VENETIAN BLINDS

by

MICHAEL R. COLLINS

A thesis submitted to the Department of Mechanical Engineering in conformity with the requirements for the degree of Master of Science (Engineering)

Queen's University
Kingston, Ontario, Canada
November, 1997

0-612-28186-8

ABSTRACT

Michael Ronald Collins: Inward-Flowing Fraction of Absorbed Solar Radiation for Fenestration with Venetian Blinds. M.Sc. thesis, Queen's University at Kingston, November 1997.

A test apparatus and method for determining the inward-flowing fraction of absorbed solar energy was successfully evaluated for use with any calorimeter. Electrical heating of the shade layer can be used to calculate N_S under specific test conditions. Input powers of about 250 W per m^2 of projected blind area produced precise results under all circumstances. Lower power inputs resulted in increased data uncertainty. Results were dependent on the interior / exterior temperature gradient. Realistic test conditions would be advisable. Results indicate that the exterior air film coefficient did not have any significant effect on results. Wind speed should be controlled to accepted standard test conditions as dictated by the ASHRAE HOF.

A predictive model found in the literature was also evaluated. Measured and calculated radiative and convective heat transfer coefficients were input to the model and compared with test data. Results showed that the model was an excellent predictor of both inward-flowing fraction and solar heat gain. As such, calorimetric testing may be unnecessary if heat transfer coefficients can be determined for all cases. Therefore, further development in this area is needed. Particularly, convective heat transfer coefficients between the glass and the interior air require closer analysis.

More testing is required for various complex fenestration systems. This testing would include both inward-flowing fraction and heat transfer coefficient measurements. A major problem encountered during this analysis was the lack of measured inward-flowing fraction data. In addition, full validation of the model requires further work, especially in regard to the effects of the interior / exterior temperature gradient.

ACKNOWLEDGMENTS

I wish to express my gratitude to my research advisor Professor Stephen J. Harrison for his support and guidance.

I would also like to express my appreciation to others who helped:

To CANMET, Queen's Department of Graduate Studies, and OGS for providing financial support in the form of scholarships and research grants;

To Queen's Department of Mechanical Engineering for the use of their facilities;

To Lora Feltham for her love, support, patience, and understanding;

To all the members of the Solar Calorimetry Laboratory for their assistance, encouragement, and friendship; and

To my parents, Ron and Genevieve, and my sisters, Lynn and Jeannine, for their love and support.

TABLE OF CONTENTS

1. INTRODUCTION 1

- 1.1 Background 1
- 1.2 Inward-Flowing Fraction 3
- 1.3 Problem Definition 7
  - 1.3.1 Objectives 8
- 1.4 Methodology 8

2. PREVIOUS WORK 11

- 2.1 Complex Glazing Models 11
  - 2.1.1 Experimental Methods 13
  - 2.1.2 Film Resistance Methods 16
  - 2.1.3 Assumed Values of Inward-Flowing Fraction 19
  - 2.1.4 Solar-Thermal Separation 21
- 2.2 Calorimetric Methods 24

3. APPARATUS AND PROCEDURES 25

- 3.1 Queen's Solar Calorimeter 26
- 3.2 Basis of Operation 30
  - 3.2.1 Inward-Flowing Fraction Test 32
  - 3.2.2 Test Uncertainty 33
- 3.3 Heat Transfer Coefficient Determination 33
  - 3.3.1 Exterior Air Film Coefficient Determination 35
  - 3.3.2 Heat Transfer Coefficient Determination for a Shading Layer 35
- 3.4 Test Series 38
  - 3.4.1 Absorbed Irradiance Test 41
  - 3.4.2 Temperature Gradient Test 41
  - 3.4.3 Exterior Air Film Coefficient Test 41
- 3.5 Test Setup 42

4. EXPERIMENTAL RESULTS 46

- 4.1 Typical Test Results 46
- 4.2 Steady-State Results 51
  - 4.2.1 Absorbed Irradiation Level Test Results 52
  - 4.2.2 Temperature Gradient Test Results 55
  - 4.2.3 Exterior Air Film Coefficient Test Results 58
- 4.3 Interior Heat Transfer Coefficient Results 61

5. DISCUSSION OF RESULTS 66

5.1 Steady-State Results....................66
5.1.1 Effects of Slat Angle....................70
5.1.2 Absorbed Irradiation Effects....................72
5.1.3 Temperature Gradient Effects....................73
5.1.4 Exterior Air Film Coefficient Effects....................75
5.2 Interior Heat Transfer Coefficient Results....................76
5.3 Modeling Results....................79
5.3.1 Comparison of Previous Models....................79
5.3.2 Comparison of Model with Test Results....................81
5.3.3 Comparison of Model with Other Experimental Data....................84

6. CONCLUSIONS AND RECOMMENDATIONS....................87

6.1 Conclusions....................87
6.2 Recommendations....................88

REFERENCES....................90

APPENDIX A - EMPIRICAL MODEL DEVELOPMENT....................95

A.1 Determination of Convection and Radiation Heat Gain from Double Glass and Venetian Blind Fenestrations [8]....................96
A.2 RADCAD™ Radiation Shape Factor Results....................100
A.3 Sample Model Calculations....................102
A.3.1 Double Glazings....................103
A.3.2 Single Glazings....................106

APPENDIX B - CALORIMETER CALIBRATION....................110

B.1 Component Calibration....................111
B.1.1 Thermocouple / Thermopile Calibration....................111
B.1.2 Flowmeter Calibration....................113
B.1.3 Pump / Fan Calibration....................114
B.1.4 Glycol Properties....................115
B.2 Test Cell Calibration....................117
B.2.1 Time Constant....................118
B.2.3 Zero Loss Analysis....................120
B.2.4 Loss Analysis....................121
B.2.5 Air Film Coefficient Test Setup....................123

APPENDIX C - UNCERTAINTY ANALYSIS....................126

C.1 General Notes on Uncertainty....................127
C.2 Inward-Flowing Fraction Uncertainty....................128

APPENDIX D - EXPERIMENTAL RESULTS 131

D.1 Example Data Set 132
D.2 Data Result Summary 140

VITA 142

LIST OF TABLES

2-1 Scope of complex glazing models. 12

2-2 Range of application of venetian blind models investigated. 12

2-3 Layer specific N values for use with Eq. (2.11). 21

3-1 Estimated radiative absorption factors from Parmelee et. al. [16] and RADCAD™. 36

3-2 Approximate test conditions used in factorial experiment 40

4-1 Summary of inward-flowing fraction test results for all slat angles 52

5-1 Coefficients and standard error determined using stepwise regression of inward-flowing fraction data. 67

5-2 Coefficients and standard error determined using stepwise regression of inward-flowing fraction data. 69

5-3 Calculated radiative heat transfer coefficients around the shading layer as a function of blind input power 76

5-4 Calculated convective heat transfer coefficients around the shading layer as a function of blind input power. 78

5-5 Layer specific optical data for use in model comparison 79

5-6 Comparison of model calculation of shading coefficient, SC, and inward-flowing fraction, N_S, for various fenestration and venetian blind combinations. 81

5-7 Comparison of experimental results with model by Farber et. al. [8] using original and measured heat transfer coefficients. 85

B-1 Calibration data for thermocouples. 112

B-2 Calibration data for flowmeter. 114

B-3 Temperature effects on 30%/70% propylene glycol and water. 115

B-4 Calculated calorimeter time constants. 119

B-5 Modeled seal losses within the calorimeter. 122

B-6 Generated wind speeds and exterior air film coefficients based of fan input power. 125

C-1 Variable Uncertainties 130

LIST OF FIGURES

1-1 Solar heat gain in a complex fenestration, with emphasis on the inward-flowing fraction of absorbed solar radiation.......5

1-2 Thermal circuit for venetian blinds from Farber et. al. [8]. 5

1-3 Effects of a venetian blind on the convective flow created by a heated planar surface [9]. 6

1-4 General outline used for current study.......10

2-1 Definition of angles for defining the position of an irradiation source and the venetian blind geometry [14]. 15

2-2 Thermal circuit for venetian blinds between glazings by Ozisik and Schutrum [20]. 17

2-3 The MoWiTT test facility [10]. 22

3-1 Queen's Solar Calorimeter. 25

3-2 Queen's solar calorimeter cross-section. 26

3-3 Calorimeter flow-loop schematic.......27

3-4 The absorber plate installed in the calorimeter. 28

3-5 Calorimeter data aquisition system.......29

3-6 Calorimeter energy balance for standard test procedures. 30

3-7 Calorimeter energy balance for inward-flowing fraction testing.......32

3-8 Calibration transfer standard schematic [42]. 34

3-9 Modified thermal circuit for calibration specimen with venetian blind in Queen's solar calorimeter. 36

3-10 Test conditions for face-centered central composite experiment design [11,12].......40

3-11 The wind generator used during testing.......42

3-12 Calibration specimen installation details [55] and photo of the installed calibration transfer standard.......44

3-13 Blind installation details [55] and photo of the installed blind.......44

4-1 Typical test response of flow variables, and calculated energy removed by the flow loop, for test #16 with a 45° slat angle.......47

4-2 Power metering of pump and fan for test #16 with a 45° slat angle. 48

4-3 Power metering of blind power for test #16 with a 45° slat angle. 48

4-4 Thermal guard performance for test #16 with a 45° slat angle. 49

4-5 Response of interior air and surface temperatures for test #16 with a 45° slat angle. 50

4-6 Response of exterior air and window temperatures for test #16 with a 45° slat angle. 50

4-7 Complete results for all tests. 51

4-8 Inward-flowing fraction results plotted verses level of absorbed irradiation effects for a -45° slat angle. 53

4-9 Inward-flowing fraction results plotted verses level of absorbed irradiation effects for a 0° slat angle 53

4-10 Inward-flowing fraction results plotted verses level of absorbed irradiation effects for a 45° slat angle 54

4-11 Inward-flowing fraction results plotted verses level of absorbed irradiation effects for a 70° slat angle 54

4-12 Inward-flowing fraction results plotted verses level of absorbed irradiation effects for all slat angles. 55

4-13 Inward-flowing fraction results plotted verses temperature gradient for a -45° slat angle. 56

4-14 Inward-flowing fraction results plotted verses temperature gradient for a 0° slat angle. 56

4-15 Inward-flowing fraction results plotted verses temperature gradient for a 45° slat angle. 57

4-16 Inward-flowing fraction results plotted verses temperature gradient for a 70° slat angle. 57

4-17 Inward-flowing fraction results plotted verses temperature gradient for all slat angles. 58

4-18 Inward-flowing fraction results plotted verses exterior air film coefficient for a -45° slat angle. 59

4-19 Inward-flowing fraction results plotted verses exterior air film coefficient for a 0° slat angle. 59

4-20 Inward-flowing fraction results plotted verses exterior air film coefficient for a 45° slat angle. 60

4-21 Inward-flowing fraction results plotted verses exterior air film coefficient for a 70° slat angle. 60

4-22 Inward-flowing fraction results plotted verses exterior air film coefficient for all slat angles. 61

4-23 Calculated radiative heat transfer coefficients for a -45° slat angle. 62

4-24 Calculated radiative heat transfer coefficients for a 0° slat angle. 62

4-25 Calculated radiative heat transfer coefficients for a 45° slat angle. 63

4-26 Calculated radiative heat transfer coefficients for a 70° slat angle. 63

4-27 Calculated convective heat transfer coefficients for a -45° slat angle...........64

4-28 Calculated convective heat transfer coefficients for a 0° slat angle. 64

4-29 Calculated convective heat transfer coefficients for a 45° slat angle. 65

4-30 Calculated convective heat transfer coefficients for a 70° slat angle. 65

5-1 Performance of the regression fit, given as Eq. (5.2), on inward-flowing fraction results...68

5-2 Performance of the regression fit, given as Eq. (5.3), on inward-flowing fraction results...70

5-3 Comparison of test results for all angles...71

5-4 Effect of absorbed irradiation for all slat angles by parametric analysis of Eq. (5.2). 72

5-5 Effect of temperature gradient for all slat angles by parametric analysis of Eq. (5.2). 74

5-6 Effect of exterior air film coefficient for all slat angles by parametric analysis of Eq. (5.2). 75

5-7 Blind to glazing temperature difference for all tests....................................77

5-8 Blind to glazing radiative heat transfer coefficient for all tests. 77

5-9 Estimated system optical performance [8]...80

5-10 Calculated verses measured N_S values for -45° slat angle for two blinds.....82

5-11 Calculated verses measured N_S values for 0° slat angle for two blinds. 83

5-12 Calculated verses measured N_S values for 45° slat angle for two blinds. 83

5-13 Calculated verses measured N_S values for 70° slat angle for two blinds. 84

A-1 Heat Transfer Phenomenon for the Convection and Low Temperature Radiation Components of the Total Heat Gain Through a Double Glass and Venetian Blind Fenestration [8]. 97

B-1 Plot of thermocouple temperature calibration...113

B-2 Plot of thermocouple voltage signal calibration. 113

B-3 Plot of best fit volume rate equation for flowmeter..................................114

B-4 Density-temperature relation in 30%/70% by volume propylene glycol and water. 116

B-5 Specific heat-temperature relation in 30%/70% by volume propylene glycol and water. 116
B-6 Calorimeter calibration energy balance. 117
B-7 Calorimeter response to step input. 119
B-8 Calorimeter test accuracy based on calibration data. 120
B-9 Error in calorimeter data based on calibration results. 121
B-10 Loss induced power measurement error. 122
B-11 Thermal circuit for calibration specimen. 123
B-12 Internal radiative and convective heat transfer coefficient results. 125

NOMENCLATURE

A	area, (m^2)
B	calorimeter calibration constant, (dimensionless)
C	conductance, (W/m^{2}K), or
C	specific heat, (J/kg·K)
D	calorimeter calibration constant, (dimensionless)
E	error, (dependent)
F	Solar Heat Gain Coefficient, (dimensionless), or
F	radiation interchange factor, (dimensionless)
h	heat transfer coefficient, (W/m^{2}K)
I	intensity of incident solar radiation, (W/m^2)
m	mass flow rate, (m^3/kg)
N	Inward-Flowing Fraction of absorbed solar radiation, (dimensionless)
P	power, (W)
q	energy flux, (W/m^2)
Q	energy, (W)
R	thermal resistance, (m^{2}K/W), or
R	resistance, (Ω)
S	shape factor (W/m·K)
SC	Shading Coefficient, (dimensionless)
SHG	Solar Heat Gain, (W/m^2)
$SHGF$	Solar Heat Gain Factor, (W/m^2)
t	time
T	Temperature, (K)
U	window U-factor, (W/m^{2}K)
V	voltage (V)

Symbols

α	absorbed solar radiation, (dimensionless)
σ	Stephan-Boltzman constant, (5.669×10^{-8})

τ	transmitted solar radiation, (dimensionless), or
τ	thermal time constant, (s)
ρ	reflected solar radiation, (dimensionless), or
ρ	density, (kg/m^3)
ΔT	indoor air to outdoor air temperature difference, (K)
ΔT_i	layer specific temperature rise, (K)
C_ρ	specific heat, (KJ/kg·K)
θ	solar incident angle, (rad)
ϕ	azimuth angle, (rad)

Subscript

1	warm side of calibration specimen
2	cold side of calibration specimen
a	air space
ap	absorber plate
bridging	bridging losses
c	common window glass
con	convective
cond	conductive
cor	calibration specimen core
d	diffuse solar radiation
D	direct solar radiation
e	element
fan	internal fan
flow	flow loop
g	glass used
g1	exterior glass
g2	interior glass
i	inside
IFF	inward-flowing fraction
input	input to calorimeter

loss	losses
mask	mask wall
o	outside
OFF	outward-flowing fraction
out	outward flow
pump	internal pump
rad	radiative
s	shade
seal	calorimeter seal
shu	shunt
spe	calibration specimen
sys	fenestration system
t	time
tot	total
wall	calorimeter walls

Superscript

$'$	core surface

CHAPTER 1

INTRODUCTION

1.1 Background

The determination of Solar Heat Gain (*SHG*) through fenestration systems is required to evaluate the energy performance of buildings, estimate peak electrical loads, and assess occupant comfort in buildings. *SHG* is the energy which enters a room through directly transmitted solar radiation and the inward flow of absorbed solar radiation. In the past, calculation of *SHG* was undertaken using tables contained in Chapter 27 of the ASHRAE Handbook of Fundamentals [1]. While these tables handle many systems adequately, the prediction of a Shading Coefficient (*SC*) or Solar Heat Gain Coefficient (*SHGC*) for new fenestration systems needs to be developed.

The shading coefficient is defined as the ratio of solar radiant heat gain by a window to the solar radiant heat gain by a 3 mm thick pane of clear double strength glass under summer design conditions [1]. The *SHG* of the reference window is referred to as the Solar Heat Gain Factor (*SHGF*). Therefore

$$SHG = (SC)(SHGF) \tag{1.1}$$

Total energy flux is then determined by

$$q = SHG - U(\Delta T) \tag{1.2}$$

where q is the energy flux through a window, U is the window U-factor, and ΔT is the indoor air to outdoor air temperature difference. In the past, tabulated values of *SC* have provided reasonable estimations of solar and thermal energy transfer through fenestration systems. However, recent trends in thermal analysis have moved away from this method of analysis, and towards the *SHGC* method [2]. *SHGC* (designated "*F*") is defined as the ratio of *SHG* transmitted though a fenestration to the value of solar irradiation incident on its surface. It is usually quoted on a per unit area basis under specified conditions of wind speed and direction, interior and exterior temperature, and solar radiation. It may be shown that, *SHG* is the product of *SHGC* and the intensity of the incident solar irradiation, *I*, i.e.,

$$SHG = F \cdot I \tag{1.3}$$

The *SHGC* of a particular fenestration can be calculated as the sum of solar energy transmitted by the system, plus the inward flow of solar energy absorbed in the system. Therefore

$$F = \tau + N \cdot \alpha \tag{1.4}$$

where $N =$ Inward-Flowing Fraction of absorbed solar radiation

$\tau =$ transmitted solar radiation

$\alpha =$ absorbed solar radiation

The rate of energy transfer through a fenestration is then calculated using Eq. (1.2).

Tables of *SHG* have also been produced for typical fenestration, and are contained in Chapter 27 of the ASHRAE HOF [1]. Unfortunately, they are no longer adequate for a significant number of products currently used on residential and commercial buildings. In particular, fenestration with some type of internal shading intended for privacy, aesthetics, and sun control are not dealt with adequately [3].

The types of shading devices available are very diverse. On the interior of a window there can be drapes, roller shades, or venetian blinds. Venetian blinds can also be placed between glazings, or on the exterior face of a window. These glazing and shade systems, referred to as "complex fenestration," balance the desire to provide privacy and reduce summer cooling load, with the desire to maximize daylighting as a means to control lighting costs. Recent developments in window technology have also resulted in the availability of a wide range of new fenestration products. Spectrally selective glazings, low-e coatings and films, and tints are increasingly common in new energy efficient windows. The combination of these new products and shading devices have made the use of tabulated shading coefficients, or solar heat gain factors, impractical.

Recently, computer simulation [4,5] has been used to estimate the thermal and solar performance of fenestrations consisting of combinations of glazings. These programs, however, were not designed to evaluate shades or blinds combined with glazing assemblies. There are two reasons why the effects of such devices cannot be analyzed effectively: (1) the complex geometry found in venetian blinds and pleated drapery creates directionally dependent optical properties which are not supported within these programs, and (2) air flow around the shading devices complicates the determination of the interior convective heat transfer coefficient.

A need exists for an evaluation technique capable of determining *SHG* values for all systems including complex fenestration. Such a method should also be easily adapted into current simulation software. To aid in the development of such a technique, the behavior of the *SHG* in complex fenestration incorporating interior venetian blinds was investigated. A critical aspect of this endeavor is the characterization of the inward-flowing fraction, *N*.

1.2 Inward-Flowing Fraction

The inward-flowing fraction (*N*) of absorbed solar radiation is the fraction of solar energy absorbed in a fenestration layer which enters the room either by radiation or convection. For each layer of the fenestration, *N* can be determined based on the U-factor of the system, and the convective and radiative heat transfer coefficients found on and between the glazings [6]. For a single glazing, *N* is given by

$$N = \frac{U}{h_o} \tag{1.5}$$

and for double glazing, excluding between glazing shades,

$$N_{g1} = \frac{U}{h_o} \tag{1.6}$$

$$N_{g2} = \frac{U}{h_o} + \frac{U}{h_a} \tag{1.7}$$

where h_o = the combined exterior radiative and convective heat transfer coefficient
h_a = the combined air space radiative and convective air film coefficient
$g1, g2$ = the exterior and interior glazings, respectively

With respect to a single shading layer, inward-flowing fraction is characterized as shown in Fig. 1-1. When solar radiation passes through a window and strikes an internal shading device, some of the energy is transmitted through the device, some reflected (either into the room or back out of the window), and some is absorbed (Fig. 1-1(a)). Absorbed energy causes the temperature of the shading device to increase relative to its surroundings. This in turn causes convection and radiation to the room, and to other glazing layers (Fig. 1-1(b)) [7].

Inward-flowing fraction for most fenestration systems is easily quantified. In systems excluding complex fenestration, each layer can transmit energy only to the layers or environments surrounding them. In addition, convective and radiative heat transfer to the room only occurs from the innermost layer. In complex fenestration, the open nature of the blind creates energy paths directly from the inner glass surface to the room. Therefore, convective and radiative heat transfer to the room is from both the shade and the inner glazing. One thermal resistance network able to describe this system was developed by Farber et. al. [8], and is shown in Fig. 1-2 and Appendix A. This network is more fully examined in later sections of the present analysis.

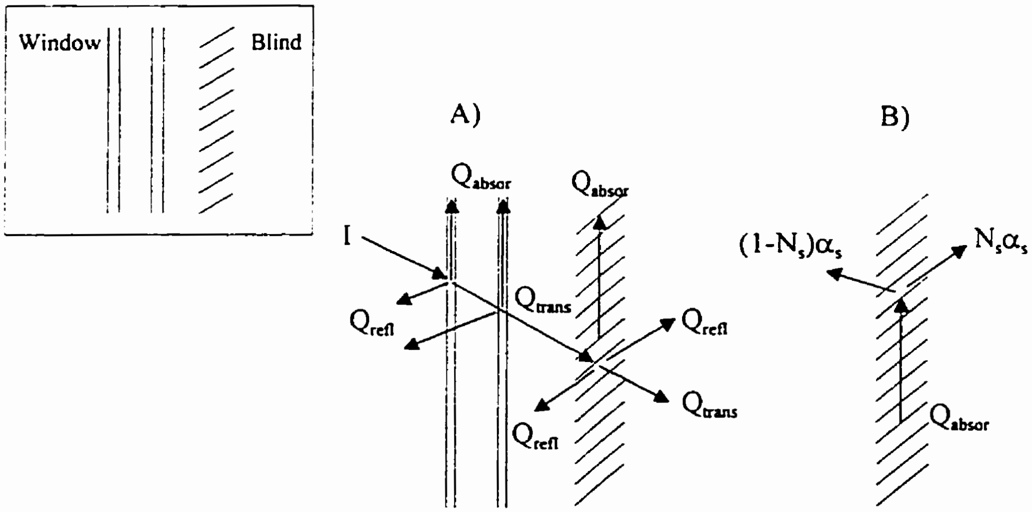

Figure 1-1. Solar heat gain in a complex fenestration, with emphasis on the inward-flowing fraction of absorbed solar radiation. (A) shows the modes of heat flow throughout the system. (B) shows the direction of heat flow resulting from absorbed energy in the shade layer.

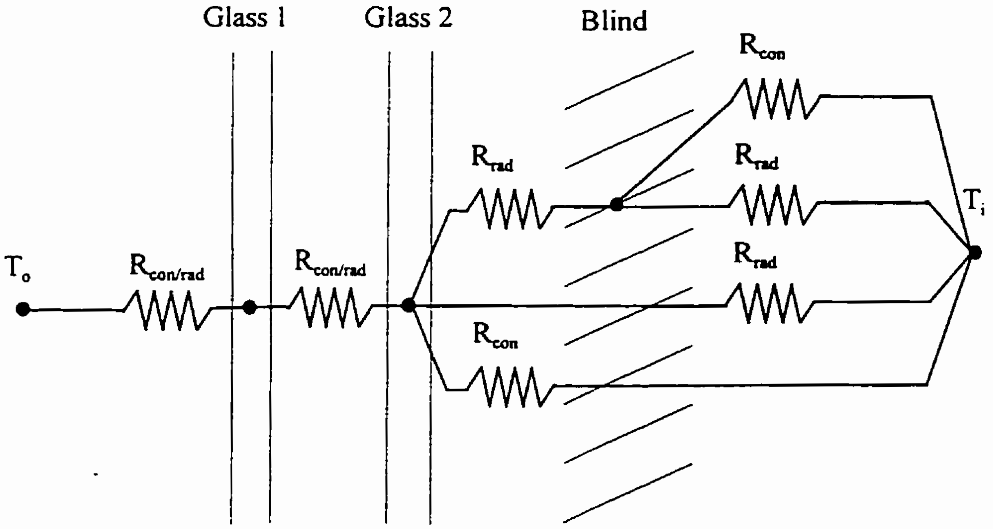

Figure 1-2. Thermal circuit for venetian blinds from Farber et. al. [8]. The model assumes that the air temperature between the glass and the shade, and the interior wall temperature, is the same as the room air temperature. R = 1/h.

An analysis of this thermal network, proposed by Farber et. al. [8], was complicated by a lack of accurate test data, and a reliable predictor of convective heat transfer coefficients. They provide an equation for predicting convective heat transfer coefficients (Eq. A.20), however, they assumed convection from the inner glazing could be represented as occurring from a simple planer surface, i.e., without interference from the slats on the outer edge of the boundary layer. In addition, convective flow from the blind was calculated using the same equation, accounting only for the increase in total surface area. Other geometric considerations are ignored. Such an analysis was undoubtedly imprecise.

The convective flows associated with heat transmission through a blind located adjacent to a glazing were recently investigated by Matchin et. al. [9]. Their analysis, which was conducted for the case of an unheated blind, shows that the convective flows around the blind slats are highly complex (Fig. 1-3), and are dependent on slat angle.

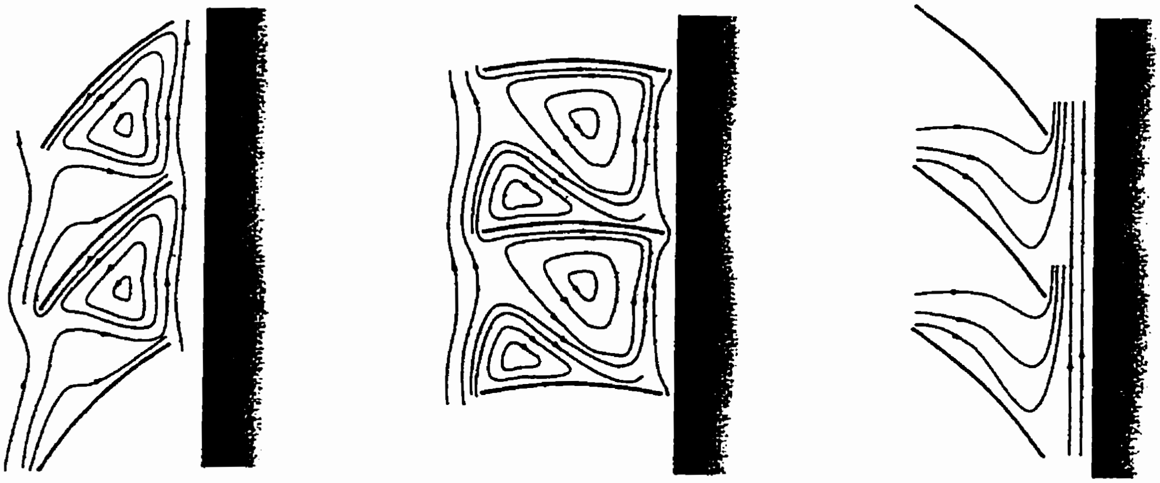

Figure 1-3. Effects of a venetian blind on the convective flow created by a heated planar surface [9].

1.3 Problem Definition

Realizing the complexity of the problems associated with the determination of *SHG* for complex fenestration, a number of advanced calculation methods were proposed. However, with the exception of a new technique called "solar-thermal separation," described in Chapter 2, previous attempts at determining *SHG* in complex fenestration systems have included the inward-flowing fraction of the shading layer without actual investigation of its characteristics. None of these models have become widely used, in part due to the treatment if inward-flowing fraction.

Recent tests, performed at Lawrence Berkeley Laboratory's Mobile Window Thermal Test Facility (MoWiTT) [10], determined the inward-flowing fraction for a limited number of blind and glazing combinations. Results of these tests showed that the inward-flowing fraction of the shade appeared to be unaffected by the level of the irradiation on the system, and was only slightly dependent on the interior / exterior temperature gradient. In addition, the exterior air film coefficient seemed to have little effect on the results. The independence of the inward-flowing fraction for the shade (N_S) to environmental conditions would greatly simplify any proposed test procedure. However, the authors of the study indicate that the level of sensitivity of N_S to these factors needed to be fully investigated if a simplified test method was to be developed.

These recommendations form the basis for the current study, i.e., the determination of the magnitude of the effects of the test conditions on the evaluation of inward-flowing fraction. Using techniques developed by Klems and Kelley [10], these effects may be experimentally investigated.

The general methodology used for this study followed that originally used by Klems in his efforts to develop solar-thermal separation. It is the first model which makes use of accurate calorimetric measurement of inward-flowing fraction for the shading layer [10]. To complete his experimental work, Klems and Kelley [10] used an electrically heated venetian blind to determine inward-flowing fraction values.

1.3.1 Objectives

The activities undertaken in this study extend the work of Klems and Kelley [10]. By conducting controlled experiments with an electrically heated blind (to simulate the effects of absorbed solar radiation), the magnitude of the inward-flowing fraction can be directly determined, and environmental effects can be gauged. The development of this experiment, and the effects of external variables on measured values of inward-flowing fraction, were the primary objectives of this study.

A secondary objective of this study was to develop a model capable of predicting the inward-flowing fraction of a venetian blind. Additional instrumentation was used to determine the convective and radiative heat transfer coefficients around the shade layer. This data, when used with a film resistance method of calculating inward-flowing fraction similar to that shown in Fig. 1-2, would lead to a simplified model. Using this model, it may be possible to accurately predict inward-flowing fraction values for use in the solar-thermal separation method, thereby avoiding calorimetric testing.

1.4 Methodology

To complete the present study, it was divided into three phases consisting of background research, test setup and calibration, and experimental testing and model development.

Background research. This phase commenced with a literature search. Similar studies, performed to date, were examined in an effort to identify previous calorimetric data, theory, and experimental procedures. In particular, results pertaining to the determination of the inward-flowing fraction of absorbed solar radiation for complex fenestration were reviewed. It was hoped that this information would provide an insight into the development of an empirical formulation, and provide baseline data and sample specifications for testing. The search also concentrated on the examination of calorimetric test procedures. Areas of interest included data acquisition and control, uncertainty analysis, calibration methods, and test conditions. With this knowledge, it was possible to develop a test specification, and identify areas requiring further development.

Test setup and calibration. This phase consisted of apparatus development and calibration. Specifically, the Queen's solar calorimeter was modified in an effort to reduce the thermal mass and response time. In addition, the instrumentation and data acquisition systems were calibrated and installed. Since the calorimeter was never used prior to this analysis, a full systems' calibration was required. This included tests to determine overall accuracy, time constant, thermal mass, guard heater performance, interior and exterior heat transfer coefficients, and identification of critical loss areas. This exercise also helped determine control and test parameters, including pump speeds, temperature settings, cooling requirements, external fan settings, and guard heater power requirements.

Experimental testing and model development. This phase focused on sample testing and model development. Specifically, an experimental test program was formulated and analyzed based on a factorial design technique [11,12]. The experiment was designed to calculate N_S for a venetian blind, while focusing on the verification of the findings by Klems and Kelley [10] concerning temperature, exterior air film coefficient, and absorbed solar irradiance dependency. Testing was conducted within this factorial design for a number of blind slat angles. These tests were also developed in a manner that allowed the examination of the interior heat transfer coefficients. The methodology used for this study is shown schematically in Fig. 1-4.

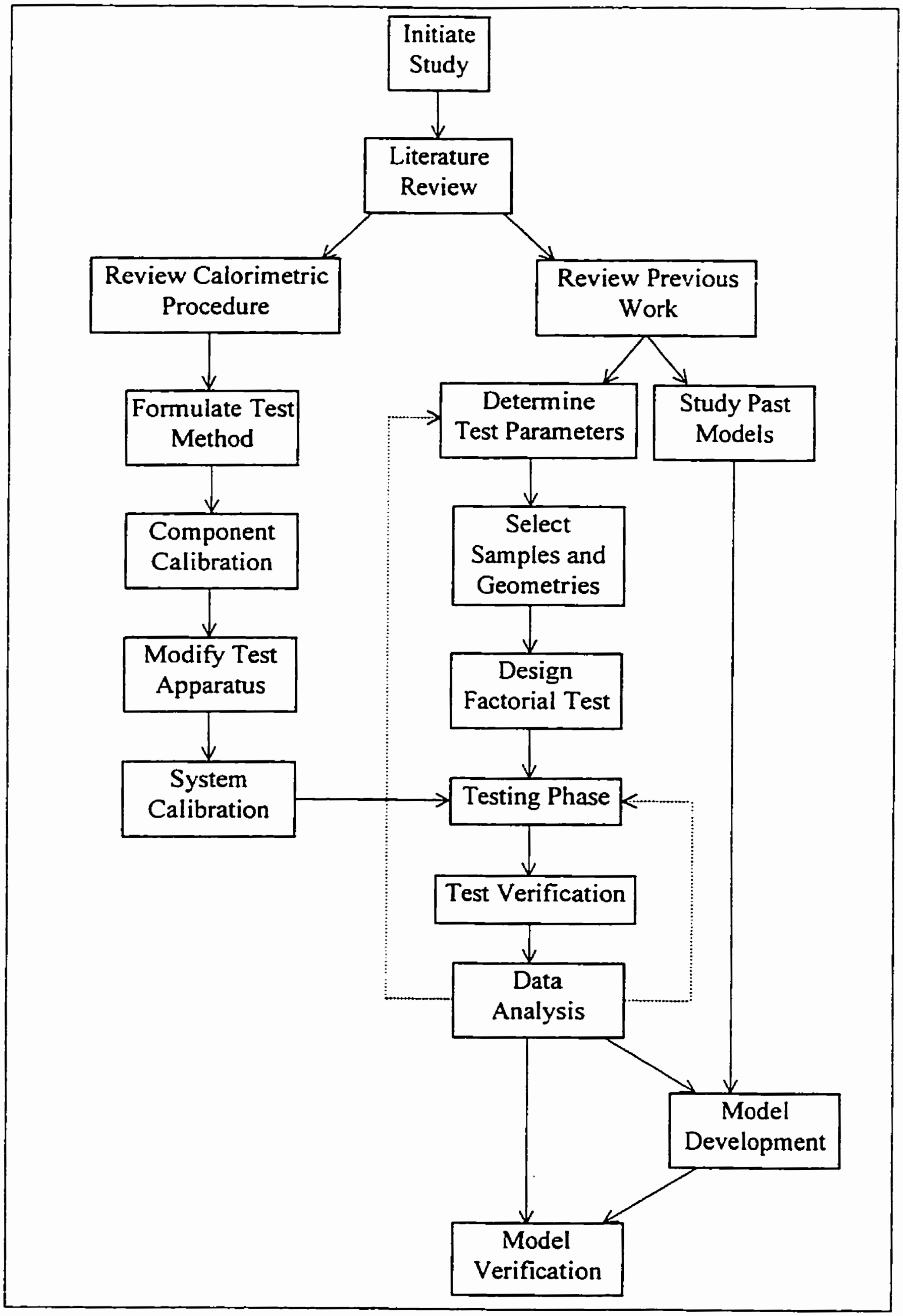

Figure 1-4. General outline used for current study.

CHAPTER 2

PREVIOUS WORK

2.1 Complex Glazing Models

The development of complex fenestration models is not a new endeavor. Since the early 1950's, researchers have attempted to quantify the effects of a shading layer on the solar and thermal performance of a window [3, 7, 8, 14-27]. These models, however, were developed for the purpose of determining *SHG*. Inward-flowing fraction data which was either estimated or measured indirectly, was considered suitable as a model input.

None of these past attempts produced an ideal model of *SHG* for complex fenestration [13]. The reason for this was largely twofold. Firstly, limitations in scope prevented the incorporation of other types of complex systems. As shown in Table 2-1, some of the models were incapable of being used for other blind positions, and fenestration types, or for cases involving multiple glazings. Secondly, poor model assumptions limited a model's accuracy and applicability. Table 2-2 shows that many venetian blind models were limited by geometry, type of light, applicable slat and profile angles, and treatment of inward-flowing fraction for the shading layer.

The versatility of these models is important in determining their level of use. Thus, a single model that can be used on many types of complex fenestration, or for a range of conditions, would be more useful than separate models for each case. The recent efforts of Klems et. al. [10,13,28-32] meets these objectives, but still requires experimentally derived values of inward-flowing fraction.

Table 2-1. Scope of complex glazing models.

Author	Shading Device					Glazing	
	Interior Blinds	Between Blinds	Exterior Blinds	Roller Shades	Drapes	Single	Double
Parmelee et. al. [14-16]	X		X			X	
Jorden and Threlkeld [7]				X		X	
Ozisik and Schutrum [3,17,20]		X		X	X	X	X[a]
Farber et. al. [8,22]	X				X	X	X
Owens [23]	X	X	X	X	X	X	X
Van Dyck and Konen [24]	X	X	X	X	X	X	X[a]
Klems et. al. [10,13,28-32]	X	X	X	X	X	X	X

[a] Double glass used only in conjunction with between glazing shading layers

Table 2-2. Range of application of venetian blind models investigated.

Author	Blind Geometry	Source Light	Slat Angles	Profile Angles	N_S
Parmelee et. al. [14-16]	Various Combinations	Direct Diffuse	0-90°	0-75°	Experimentally Determined Constant
Ozisik and Schutrum [20]	Various Combinations	Direct Diffuse	30,45°	0-80°	Based on Film Coefficients
Farber et. al. [8,22]	Various Combinations	Direct Diffuse	0,30,45°	0-70°	Based on Film Coefficients
Owens [23]	Two Specific	Direct	0,45°	0°	1
Van Dyck and Konen [24]	Various Combinations	Direct Diffuse	0,45,90°	0-45°	1
Klems et. al. [10,13,28-32]	Various Combinations	Direct Diffuse	Any	Any	Experimentally Determined Constant

In the context of this research, the last column of Table 2-2 shows the various ways in which inward-flowing fraction was treated. Each method will be more aptly discussed on a model by model basis. In the following sections, models are divided into groups representing experimental methods, film resistance methods, and assumptions concerning the nature of inward-flowing fraction. Note that the notation originally used by the authors may be modified to maintain consistency and avoid confusion.

2.1.1 Experimental Methods

Experimental methods are those in which the researchers have attempted to directly or indirectly measure the inward-flowing fraction of a shading layer. Using calorimetric methods, inward-flowing fraction was experimentally determined on a number of occasions for many different shade types [3, 13-18].

The earliest model was developed by Parmelee et. al. [14-16]. In an attempt to determine the effectiveness of interior and exterior slat-type sun shades for reducing heat gain through a single pane of sunlit glazing.

The first reference presents the mathematical analysis [14], and the second presents experimental verification [15], of the fenestration system's optical properties. Expressions were obtained for the total heat gain and *SC* in terms of the transmittance and absorptance of the system, and an experimentally determined factor, *n*, used to account for the percent of absorbed solar energy that enters the room.

$$SC = \frac{\tau_{sys,D} \cdot I_D + \tau_{sys,d} \cdot I_d + n[(\alpha_{sys,D} - \alpha_{g,D})I_D + (\alpha_{sys,d} - \alpha_{g,d})I_d]}{\tau_{c,D} \cdot I_D + \tau_{c,d} \cdot I_d} \tag{2.1}$$

where $n =$ 0.75 for indoor shades, 0.05 for outdoor shades

$d, D =$ diffuse and direct solar irradiation respectively

$sys =$ the fenestration system

$g, c =$ the glass used and common window glass respectively

The factor, *n*, was determined based on where the blind was situated in relation to the glazing. In a later work [16], tables of design data for use in predicting *SC* for venetian blinds and sun screens in combination with several types of single flat glass are presented. A method of determining the apparent optical properties of each layer, including radiation shape factors for the shade layer, is also described.

Inward-flowing fraction was not dealt with directly in this case. Although the factor, *n*, may appear to be the inward-flowing fraction, algebraic manipulation shows that it is not. The *SHGC* was found by multiplying the *SC* given in Eq. (2.1) by the *SHG* of the reference window, i.e.,

$$F = \frac{SC \cdot \left(U_c / h_o (\alpha_{c,D} \cdot I_D + \alpha_{c,d} \cdot I_d) + \tau_{c,D} \cdot I_D + \tau_{c,d} \cdot I_d \right)}{I} \tag{2.2}$$

Combining this with Eqs. (1.3) and (1.5), the inward-flowing fraction of a shade is given by

$$N_s = \frac{F - \tau_{sys} - \frac{U_{sys}}{h_o} \alpha_{g1'}}{\alpha_{s'}} \tag{2.3}$$

where the subscript *s* and ' denote the shade layer and the apparent properties of a layer as determined using a method described in reference [8], respectively.

The scope of the investigation by Parmelee et. al. [14-16] was thorough. Test samples were specially chosen to cover a broad range of cases including color, reflection characteristics, and geometry. A number of solar conditions were also investigated. The analysis included testing to determine the effects of diffuse irradiance, and variable incident angle (changing profile and azimuth angles as defined in Fig. 2-1). They concluded that the value, *n*, was constant for all similar systems, and contended that under most situations, incidence angle could be accurately represented by profile angle.

Parmelee et. al. [14-16] did point out that their analysis did not examine situations of high incidence or polarized light, and while *n* appeared constant for the single glazing and shade systems considered in their study, a constant value of *n* may not suitably represent the complexity of a multiple glazing and shade combination.

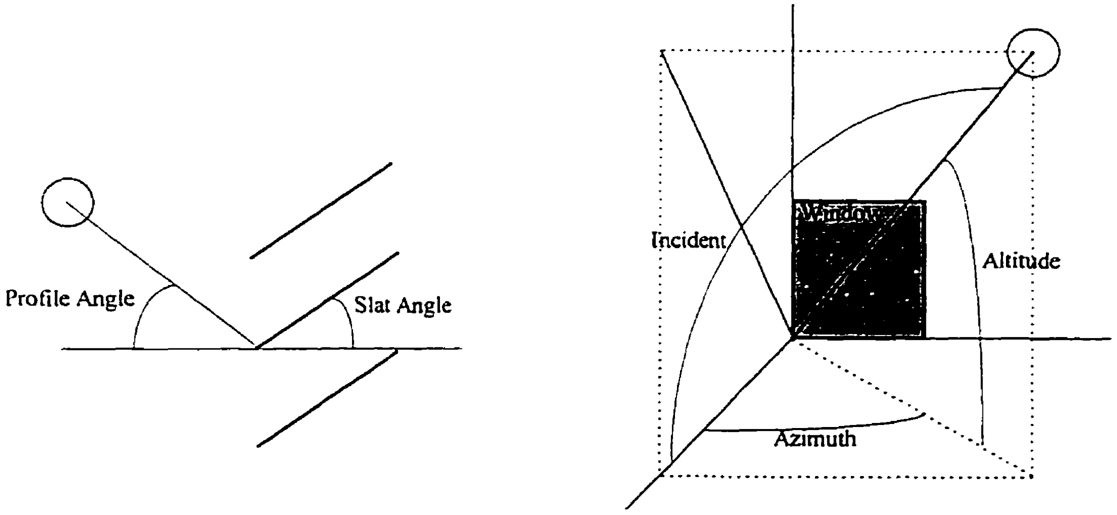

Figure 2-1. Definition of angles for defining the position of an irradiation source and the venetian blind geometry [14].

A similar investigation was performed by Ozisik and Schutrum [3, 17] with validation completed by Yellott [18]. In their analysis, they determined the *SHG* in single glazings with roller shades and drapes. An experimentally determined value, *b*, was used to find the convective and radiative gain due to absorbed radiation in the shade layer. This factor was used to correlate the inward-flowing fraction of a sealed interior shading layer, (which is easily calculated using Eq. (1.7)) to that of an unsealed layer. Moore and Pennington [20] also presented an equation, proposed by Schutrum, for analyzing complex fenestration using drapery. This equation uses an experimentally determined value of N_S for the drapery layer. Without further experimentation, the factor *b* and the constant used by Schutrum for N_S, cannot be determined for venetian blinds, and therefore, will not be analyzed here.

The most comprehensive analysis of a widely applicable model has been presented by Klems et. al. [10,13,28-32] (the solar-thermal separation method). As stated, the method employed in the present analysis builds on this method. It is therefore discussed separately in Section 2.1.4.

2.1.2 Film Resistance Methods

Film resistance methods are those in which the researchers have attempted to estimate the convective and radiative heat transfer coefficients between fenestration layers, and apply them to a classical resistance analogy. Such analyses were well established for single and double glazings, and were previously described in Eqs. (1.5) to (1.7). The extension of this analysis to incorporate a shading layer is a difficult task that was largely avoided in the literature.

Two research groups did attempt to calculate inward-flowing fraction based on the heat transfer coefficients present in a complex fenestration system [8, 20-22]. In much the same way that inward-flowing fraction is handled for normal fenestration, both Ozisik and Schutrum [20], and Farber et. al. [8, 22] and Smith and Pennington [21] attempted to apply a film resistance method.

The model developed by Ozisik and Schutrum attempted to determine *SHG* for the case where blinds were installed between the glazings of a double glazed window [20]. Although this type of complex fenestration is outside the scope of the present analysis, its treatment of the shade layer provides insight into the development of a mathematical solution. It was based on the calculated optical and thermal properties of each layer. Optical properties were determined using well established theory, while thermal properties were calculated from the heat balance equations under steady-state conditions. As with other models, the total *SHG* was then given as the sum of the transmitted solar energy, and some fraction of the energy absorbed by the fenestration. For between glass shades, the authors presented the equation

$$\begin{aligned}F = [U \cdot I_D[G_3 \cdot \alpha_{g2',D} + G_2 \cdot \alpha_{s',D} + G_1 \cdot \alpha_{g1',D}] \\ + U \cdot I_d[G_3 \cdot \alpha_{g2',d} + G_2 \cdot \alpha_{s',d} + G_1 \cdot \alpha_{g1',d}] \\ + I_D \cdot \tau_{sys,D} + I_d \cdot \tau_{sys,d}] / I\end{aligned} \tag{2.4}$$

where

$$G_1 = \frac{1}{h_o} \tag{2.4a}$$

$$G_2 = \frac{1}{h_o} + \frac{1}{(h_{cr1s} + 2h_{r12})} \tag{2.4b}$$

$$G_3 = \frac{1}{h_o} + \frac{2}{(h_{cr1s} + 2h_{r12})} \tag{2.4c}$$

$$U = \frac{1}{\frac{1}{h_o} + \frac{2}{h_{cr1s} + 2h_{r12}} + \frac{1}{h_i}} \tag{2.4d}$$

and h_{cr1s} = convection / radiation air film coefficient between the shade and glass (estimated as 4.5 W/m^{2}K in reference [20])

h_{r12} = radiation heat transfer coefficient from the interior to exterior glass (estimated as 1.7 W/m^{2}K in reference [20])

It is important to note that the factors G_i presented in Eqs. (2.4a-d) are the summation of film resistances from i^{th} layer to the exterior. These resistances were calculated in reference [20] using the network shown in Fig. 2-2.

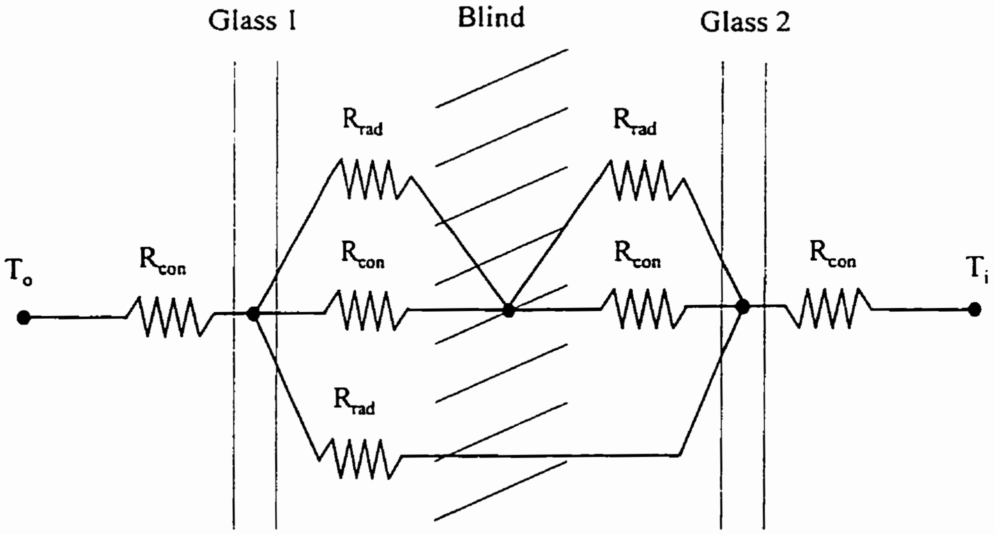

Figure 2-2. Thermal circuit for venetian blinds between glazings by Ozisik and Schutrum [20].

The inward-flowing fraction can be determined using Eq. (2.3) or by

$$N_s = \frac{U}{\left(\frac{1}{h_o} + \frac{1}{h_{cr1s} + 2h_{r12}} \right)^{-1}} \tag{2.5}$$

Ozisik and Schutrum [20] appear to have produced a workable model. Unfortunately, data for use in the equations was limited in scope and availability. Multiple geometries or different types of glass were never tested adequately, and only three types of slats were tested at two different slat angles. However, their model results did agree with calorimetric data. This model was also validated experimentally in a later paper by Smith and Pennington [21]. Such cases provide strong support for a resistance style model.

Farber et. al. [8, 22] presented a mathematical derivation and experimental verification of a *SHG* model for a double glass barrier with shades or drapes. Based on the previously described models by Parmelee et. al. [14-16], and Ozisik and Schutrum [20], the authors attempted to expand the mathematical analysis to better incorporate: gains from diffuse sources; inward-flowing fraction of absorbed solar energy; complex geometries (such as blinds or pleated drapes); and multiple glazings. They expressed *SC* as

$$SC = \frac{(\tau_{sys,D} \cdot I_D + \tau_{sys,d} \cdot I_d) + (N_D \cdot \alpha_{sys,D} \cdot I_D + N_d \cdot \alpha_{sys,d} \cdot I_d)}{U_c / h_o(\alpha_{c,D} \cdot I_D + \alpha_{c,d} \cdot I_d) + \tau_{c,D} \cdot I_D + \tau_{c,d} \cdot I_d} \tag{2.6}$$

where

$$N = f(h_o, h_1, h_2, h_3, h_4, h_5, h_6, \dot{m}C_\rho, \alpha_{g1'}, \alpha_{g2'}, \alpha_{g3'}) \tag{2.6a}$$

and where $\dot{m}$ and C_ρ are the mass flow rate and specific heat of air respectively. System optical properties were determined using reference [8].

The energy balanced developed by Farber et. al. [8, 22] could easily be solved using matrix algebra. The actual system equations, represented by the resistance analogy shown in Fig. 1-2, are outlined in Appendix A. The inward-flow of absorbed radiation for the entire system was one output of the matrix solution. N_S was then determined by

$$N_s = \frac{N_{sys} \cdot \alpha_{sys} - N_{g1} \cdot \alpha_{g1'} - N_{g2} \cdot \alpha_{g21}}{\alpha_{s'}} \tag{2.7}$$

In addition, equations were provided for estimating radiative and convective heat transfer coefficients. Reference [16] was also cited for use in determining radiation shape factors.

Although this method was developed for analyzing double glazings with an interior shade, it was easily modified to incorporate single glazings. Careful manipulation of heat transfer coefficients and optical properties was all that was required.

Other analyses considered utilized a film resistance method. For example, Ozisik and Schutrum [3, 17] used a pseudo-film resistance method to determined the *SHG* in single glazings with roller shades and drapes. Using Eq. (1.7), they determined inward-flowing fraction for a sealed shade layer. Such cases represent the simplest of analyses. The complex fenestration is treated as a triple glazing with an opaque layer. They then provided an experimentally determined correlation factor to associate this with the unsealed case. These models are not considered here.

2.1.3 Assumed Values of Inward-Flowing Fraction

Some of the more recent analyses [23-27] were produced under the assumption that the inward-flowing fraction was a constant. More specifically, all energy absorbed in the blind was assumed to remain within the room, i.e., the inward-flowing fraction was 1. While this assumption may well cause only small errors for systems with excellent thermal performance, it has never been validated for use with poorly performing windows, such as single glazings.

One such analysis, produced by Owens [23], provided a mathematical analysis of blind performance. Using a matrix technique, Owens found the optical properties of the shading layer were based on the properties of the material. He then performed an energy balance to determine heat flow and absorption in each layer. Calculation of layer absorption was accomplished using the matrix formulation

$$[H][\Delta T_i] = [\alpha_{n'}] \tag{2.8}$$

where $H_{1,1} = h_o + h_i$

$H_{i,i} = h_{n-1} + h_n$

$H_{m,m} = h_{i-1} + h_i$ for $i = 2$ to n-1

$H_{i,i-1} = -h_{i-1}$ for $i = 2$ to n

$H_{i,i+1} = -h_i$ for $i = 1$ to n-1

and i and n denote the i^{th} and the inner layer respectively, and ΔT_i is the layer specific temperature rise. For between the glazings blinds, the inward-flowing fraction of the system can be calculated as

$$N_{sys} = \frac{h_i \cdot \Delta T_i}{\alpha_{sys}} \tag{2.9}$$

from this, N_S can then be found using Eqs. (1.6), (1-7), and (2.7).

Although Eq. (2.9) is actually a film resistance method of determining N_S, Owens [23] changes his method of solving for N_S for blinds situated on the inside of the window. By using the calculated effective absorption of each layer, and the film resistance method of determining N_{g1} and N_{g2}, and $N_S = 1$, it was possible to accurately reproduce his data.

This was the first of the models discussed here that was able to perform a wide spectrum of analyses incorporating multiple glazings, coatings, and various types of shades. However, trying to deal with the complexity of the problem, Owens [23] oversimplified the analysis. For example, all properties were calculated at normal incidence, disregarding diffuse sources. Convective effects at the inside window surface were also considered to be inconsequential, i.e., it was assumed that the system was dominated by the transmitted and reflected-through component of the direct solar radiation.

Recently, Van Dyck and Konen [24] developed a mathematical method similar to some of the previous models. They performed the standard optical balance to determine effective transmittance and absorbed energy within each layer. Inward-flowing fraction of the glazing was calculated then using Eq. (1.5). For the blind, they postulated that all energy absorbed by any interior shading layer (blind, roller shade, or drape) will remain in the room. They then produced the following equation for single glazings with internal shading

$$SC = \frac{1}{0.87}\left[\frac{(1-\rho_s)\tau_{g1}}{(1-\rho_{g1}\cdot\rho_s)} + N_{g1}\cdot\alpha_{g1}\left(1+\frac{\rho_s\cdot\tau_{g1}}{(1-\rho_{g1}\cdot\rho_s)}\right)\right] \tag{2.10}$$

where ρ is the reflectivity, and 0.87 is the *SHG* of a reference glazing. McCluney [25] and McCluney and Mills [26] independently reproduced this model.

This work was extended to give predictive equations for single glazings with other types of shading layers [27]. Thus, for any shading layer and single glazing combination, they propose

$$SC = \frac{1}{0.87}\left[\frac{\tau_s\cdot\tau_{g1}}{(1-\rho_{g1}\cdot\rho_s)} + N_{ii}\frac{\alpha_s\cdot\tau_{g1}}{(1-\rho_{g1}\cdot\rho_s)} + N_{g1}\cdot\alpha_{g1}\left(1+\frac{\rho_s\cdot\tau_{g1}}{(1-\rho_{g1}\cdot\rho_s)}\right)\right] \tag{2.11}$$

where Table 2-3 shows the layer specific inputs for inward-flowing fraction.

Table 2-3. Layer specific *N* values for use with Eq. (2.11).

	Exterior Shade	Interior Shade
N_{g1}	0.11	0.267
N_S	0.69	1

The interior blind analysis was completed for single glazings only. The adaptation of such a model to a double glazing scenario would have to be completed to provide a reasonable range of application.

2.1.4 Solar-Thermal Separation

As previously mentioned, a new method was proposed by Klems et. al. [10, 13, 28-32] that attempts to calculate complex fenestration *SHGC* by a combination of calorimetric and first principle methods. Assuming transmissivity and absorptance to be purely optical properties, allowed them to be measured using a scanning radiometer. Similarly, if N_S is considered to be purely a thermal property, then a calorimetric test would suffice for any particular geometry, regardless of material properties. Accounting for the angular dependence of the optical properties, Eq. (1.3) becomes

$$F(\theta,\phi) = \tau(\theta,\phi) + \sum_{i=1}^{M} N_i \cdot \alpha_{i'}(\theta,\phi) \tag{2.12}$$

where θ is the solar incident angle, and ϕ is the azimuth angle.

To determine the inward-flowing fraction of a venetian blind, measurements were take at Lawrence Berkeley Laboratory's, MoWiTT Facility (Fig. 2-3) [10]. In this facility, two complex fenestration samples were placed in adjacent and identical calorimetric cells. In one, the blind was electrically heated to simulate solar absorptance. The increase in metered energy between the two cells could then be attributed to

$$Q = N_s \cdot P \tag{2.13}$$

where Q is the metered energy and P is the input power to the blind.

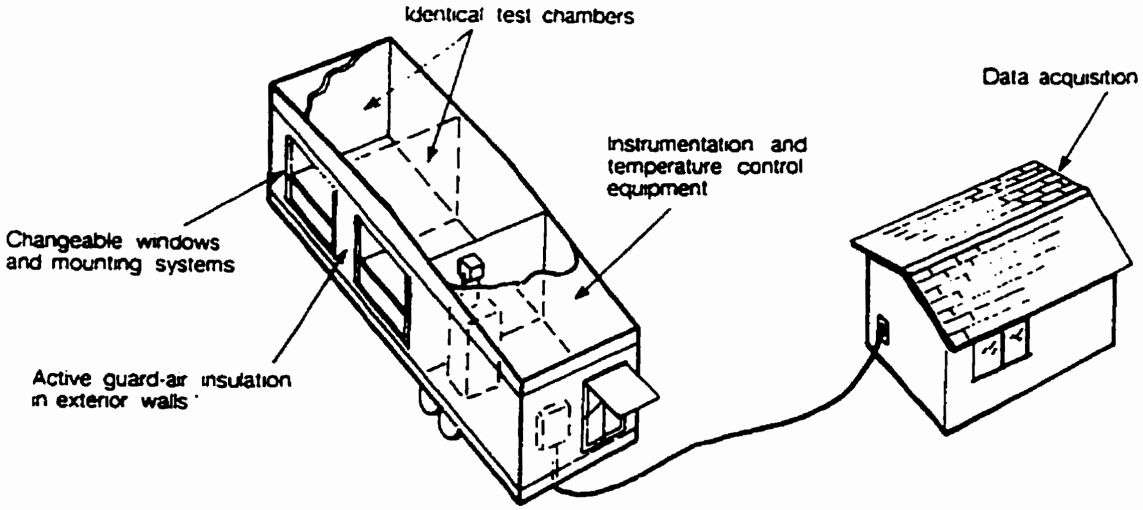

Figure 2-3. The MoWiTT test facility [10].

Solar-thermal separation has shown great potential over previous models [13]. It is potentially applicable to all geometries, all shading devices, with all types and numbers of glazings, in any combination or order. Any system could be analyzed using this method. Also, using solar-thermal separation, the *SHGC* for a complex fenestration can be calculated for any orientation, irradiation direction, or surroundings, where the previously reviewed models only quoted a single *SHGC* applicable over a range of profile angles.

The model by Klems et. al [10, 13, 28-32] seems to be the only model capable of a full analysis of any system. Application of this approach could permit the accurate and repeatable characterization of optically complex fenestration systems, accounting for the spectral and directional dependent properties of individual fenestration components. Unfortunately, solar-thermal separation is still in its infancy, and an extensive program of testing is still necessary to build a data base of inward-flowing fraction and system optical properties.

The experiments of Klems and Kelley [10], completed using MoWiTT, produced some interesting results. Inward-flowing fraction measurements showed no significant change between values taken early and late in the day. Consequently, they found that there was no evidence that N_S was temperature dependent. As such, it may not be necessary to induce a temperature differential during testing. They also found that while the intensity level and the incident angle of irradiation affected the absorption of solar energy in the blind, it did not affect where the absorbed energy went. It may therefore be unnecessary to irradiate the specimen during testing. Finally, it seemed that outdoor weather conditions had either no effect, or compensating effects on N_S. Klems and Kelley [10] theorize that high afternoon wind speeds (and consequently high exterior air film coefficients) would decrease N_S, but were offset by an increase in exterior temperature relative to room temperature. The opposite occurred early in the day when the temperature difference and wind speed were low.

Combining these results, it would appear possible to perform an inward-flowing fraction test indoors with no temperature gradient, and no irradiation. In addition, because all power input is provided through the blind, only one window is needed. An identical control sample, such as the one described in reference [10], would not be necessary.

2.2 Calorimetric Methods

A calorimeter is an instrument for measurement of the total energy flow, independent of the energy type, through a defined sample. The concept of a fenestration calorimeter consists of an idealized closed control volume, a portion of which is formed by the fenestration sample. It is assumed that changes in the energy level inside the control volume and all energy flows across the control volume boundary can be determined, and therefore, the energy flow through the sample can also be determined [33].

Calorimetry and calorimetric methods have long been suggested in the ASHRAE HOF [1] as a method for determining the thermal and solar performance of fenestration systems. These methods rely on thermal measurements to determine performance under realistic conditions. In the past, test facilities have ranged from large room style calorimeters designed to simulate actual fenestration and room interaction, to small sun tracking calorimeters. Test methods have included inducing temperature gradients, and the use of solar or artificial irradiation.

Calorimetric instrumentation, calibration methods, uncertainty analyses, test conditions, and test methods are detailed in a number of sources [34-46]. Solar Calorimetry and *SHG* measurement was described by Parmelee et. al. [34]. Harrison et. al. [35-39] described the design and measurement of *SHG* and thermal performance of windows using artificial irradiation. Another paper described the uncertainty analysis of the same system [40]. Hot box tests are described in papers by Rennekamp [41], Bowen [42], and Harrison and Barakat [43]. A number of window rating authorities have also put forward calorimetric methods and standards. These include the National Fenestration Rating Council [44], the American Society of Testing Materials [45], and CANMET [46].

This selection of references is in no way complete. However, considering the volume of available documentation, and the fact that calorimetric testing of inward-flowing fraction is a new and unproved test procedure, an extensive literature review would not be productive in the context of this project. Instead, where applicable, these procedures will be referenced as they apply to the development and use of the test apparatus described in Chapter 3.

CHAPTER 3

APPARATUS AND PROCEDURES

Testing was performed at the Solar Calorimetry Laboratory at Queen's University at Kingston. The principal apparatus was the solar calorimeter (Fig. 3-1), which was modified to perform inward-flowing fraction tests. A calibration transfer standard was also constructed to aid in heat transfer coefficient determination. A description of this equipment, the theory behind their operation, and the test parameters are discussed in the following sections.

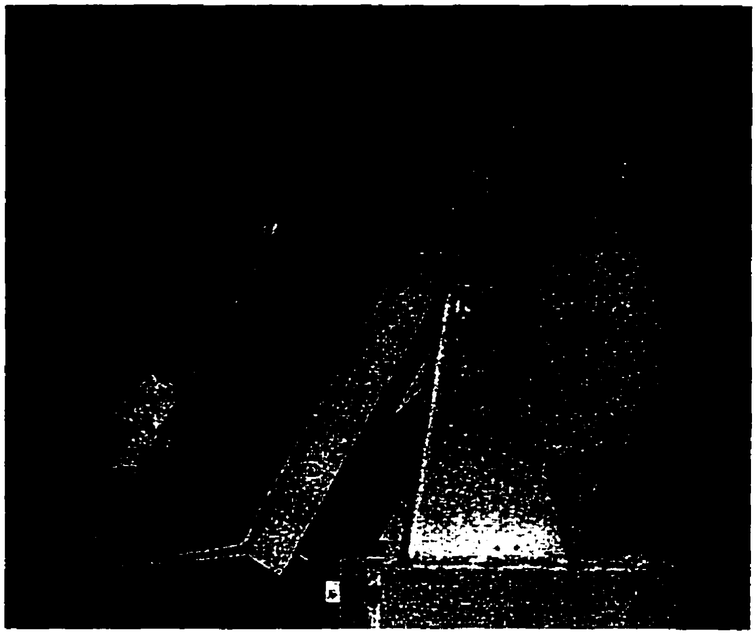

Figure 3-1. Queen's solar calorimeter.

3.1 Queen's Solar Calorimeter

Queen's Solar Calorimeter was constructed at Queen's University in 1995 for the purpose of *SHG* testing (Fig. 3-2). Final construction of the calorimeter was completed in 1997 and included several modifications required for this project.

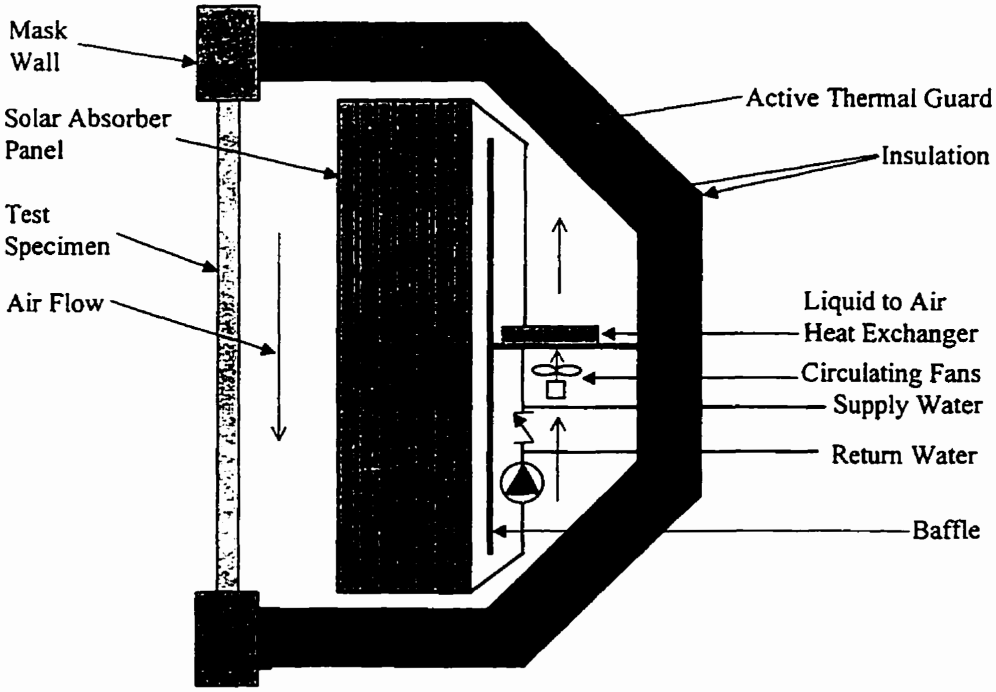

Figure 3-2. Queen's solar calorimeter cross-section.

The calorimeter incorporates many important systems. The active thermal guard, mask wall, liquid flow loop, air circulation system, and DA systems are integral to its successful operation.

The walls of the solar calorimeter are designed to reduce heat loss through the use of an active thermal guard. A series of individually controlled heaters, placed inside the calorimeter wall, are controlled to activate when a temperature gradient is measured between the interior surface of the calorimeter and the heater. Ideally, by eliminating the temperature gradient across the wall, it should be possible to eliminate heat flux.

A mask wall covers the calorimeter aperture. It is an insulated wall in which a test sample is installed (Fig. 3-2).

Energy removal and metering in the calorimeter is primarily accomplished using a liquid circulation loop, as shown in Fig. 3-3. It consisted of two connected flow loops. The interior loop consisted of an absorber plate, air to liquid heat exchanger, and circulating pump. This loop was designed to equalize the interior temperature and to quickly absorb energy input to the calorimeter. From this loop, a second loop was used to remove heated liquid, and replace it with cooler conditioned liquid. Energy metering is accomplished in this loop with integral temperature and flow measurement devices. A constant displacement pump was used to circulate this fluid to a temperature conditioning bath. Warm water, removed from the calorimeter, was cooled by a chiller, and then conditioned in a temperature bath before being returned.

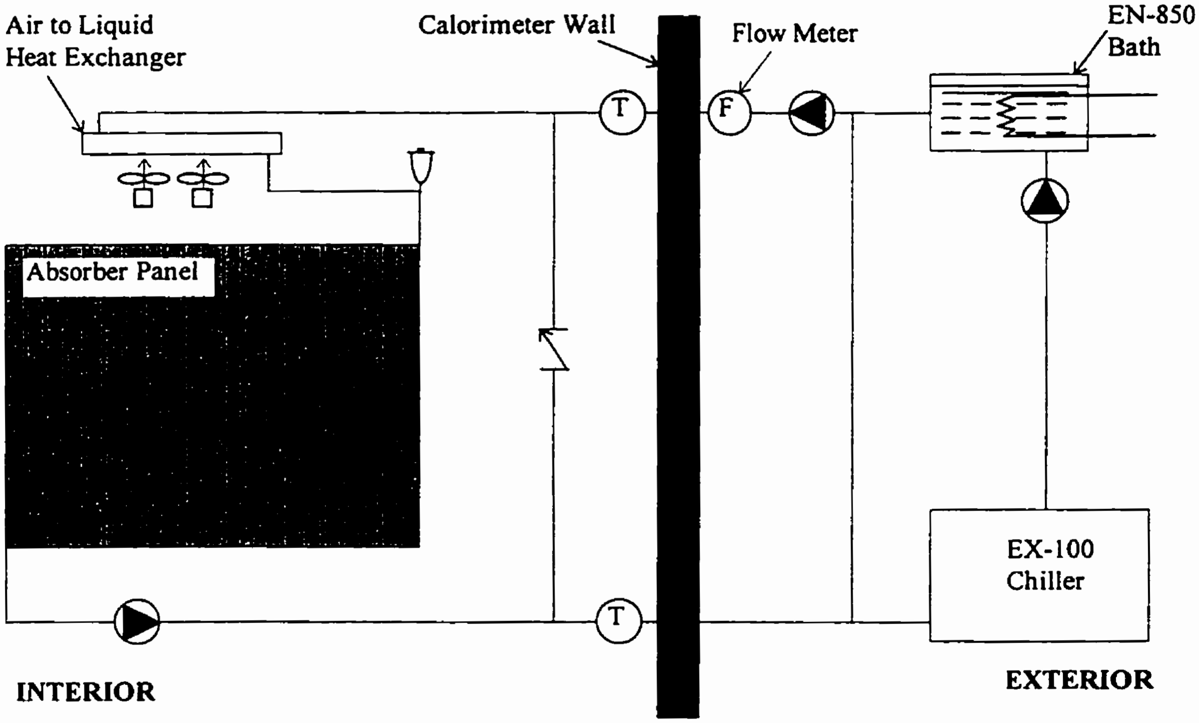

Figure 3-3. Calorimeter flow-loop schematic.

The absorber plate, located in the calorimeter, is the primary energy absorption device within the calorimeter (Fig. 3-4). Essentially, it is a plate heat exchanger placed within the calorimeter to intercept solar radiation. It is constructed of copper fins connected to copper pipes (which are part of the flow loop), and is painted matte black to increase absorptivity.

A second compact heat exchanger was incorporated within the chamber to enhance air to liquid heat transfer and improve response time. Two fans circulate the air around the test cell and through the air to liquid heat exchanger. A baffle located behind the absorber plate ensures that the air flow is upwards through the heat exchanger, and does not short circuit through the absorber plate.

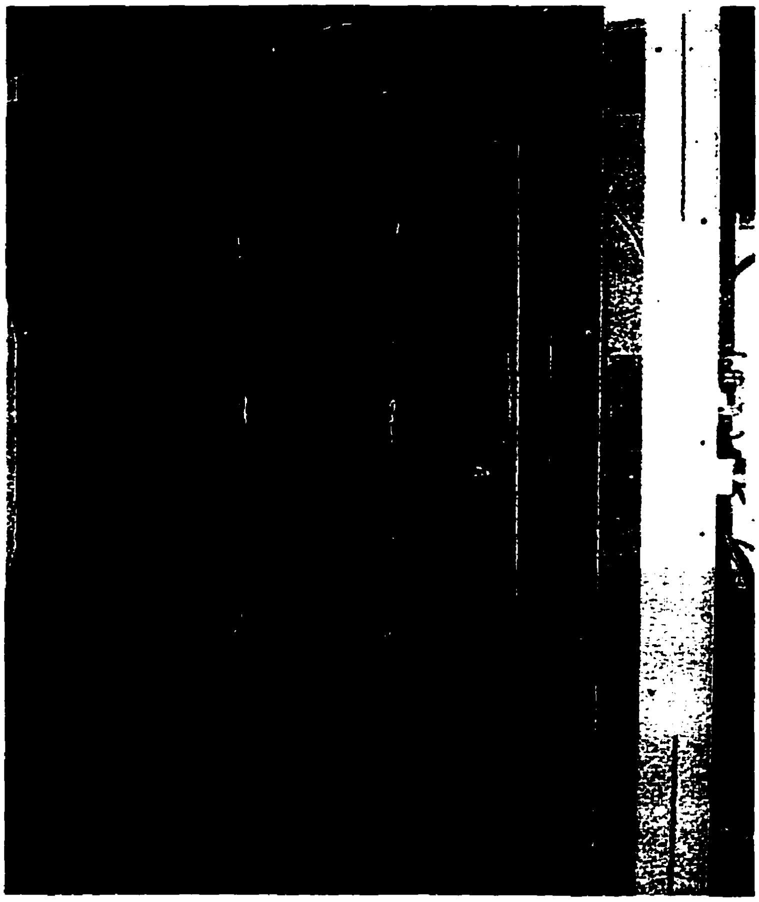

Figure 3-4. The absorber plate installed in the calorimeter

The metering loop contains all equipment necessary to meter removed energy from the calorimeter. Flow volume is metered using a Clorius Combimeter 1.5 FP/VP, magnetic inductive flowmeter [47]. The flowmeter provides a pulse output for each 0.107 L of fluid. During testing, pulses are recorded and counted by the DA system over specified time intervals, Δt, and the mass flow rate of cooling liquid is calculated as

$$\dot{m} = 0.107 \cdot \rho \cdot \frac{\Delta pulse}{\Delta t} \tag{3.1}$$

where ρ is the fluid density. Inlet and outlet temperature wells are located inside the test chamber. The inlet temperature well is located within the wall, and the outlet is just inside the calorimeter. Only the outlet temperature and the change in temperature was recorded. Fluid properties were carefully determined for the working fluid (30% / 70% by volume propylene glycol and water). The fluid density and specific heat were calculated based on the average fluid temperature between the inlet and outlet.

A constant temperature bath was used to condition the calorimeter flow. The temperature bath was an EXACAL 100 constant temperature bath circulator, equipped with an ENDOCAL 850 flow through cooler, and a DCR-1 digital controller / readout [48]. This setup is able to control from -50 to 150°C +/- 0.01°C and has a maximum cooling and heating capacity of 800 W.

Control and data aquisition was provided by a Sciemetrics model 641 and model 7000 [49] data aquisition system connected to a PC computer running the QMON [50] program (Fig. 3-5).

Figure 3-5. Calorimeter data aquisition system.

A detailed description of the calorimeter and its systems can be found in reference [51]. Calibration details for the calorimeter can be found in Appendix B.

3.2 Basis of Operation

To calculate the energy input into a calorimeter due to SHG, careful metering of the input and output energy flows is required. This includes energy removed by the flow loop, energy added by any internal fans and pumps, and losses through the calorimeter walls. The energy balance of the calorimeter can be seen in Fig. 3-6.

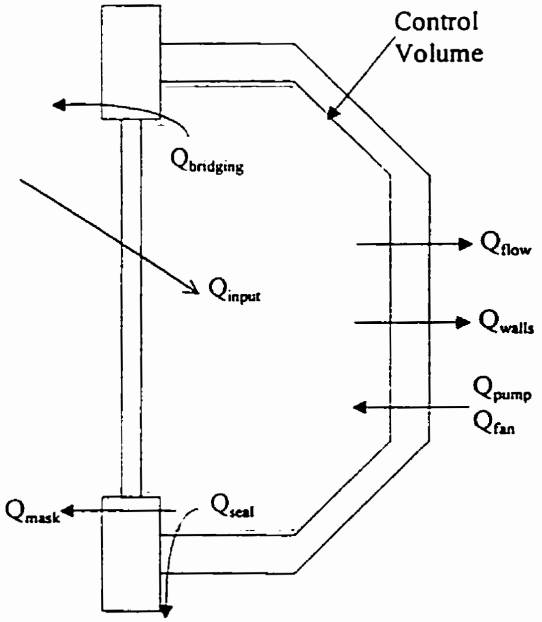

Figure 3-6. Calorimeter energy balance for standard test procedures.

In equation form, energy input is determined by

$$Q_{input} = Q_{flow} - Q_{pump} - Q_{fan} + \sum Q_{loss} \qquad (3.2)$$

where

$$\sum Q_{loss} = Q_{bridging} + Q_{seal} + Q_{walls} + Q_{mask} \qquad (3.3)$$

The first term on the right hand side of Eq. (3.2) represents the energy removed from the calorimeter by the conditioning flow loop. Q_{flow} is calculated as

$$Q_{flow} = \dot{m} \cdot C_p (T_{in} - T_{out}) \qquad (3.4)$$

where $\dot{m}$ is the mass flow rate, C_p is the fluid specific heat, and T_{in} and T_{out} are the temperature of inward flow and outward flow respectively.

The second and third terms on the right hand side of Eq. (3.2) represent the energy added to operate the internal air circulating fans, and the pump for the inner flow loop. It was understood that this power is expended within the calorimeter, and must therefore be monitored. By measuring the voltage and current entering the calorimeter (denoted as *e)*, by using a voltage divider circuit, power is calculated as follows

$$Q_{fan/pump} = V_e \cdot I_e \tag{3.5}$$

Total power input by these devices never accounted for more then 8 W.

The losses expressed in Eq. (3.3) are accounted for in different ways. The easiest to examine were mask losses. Thermopiles were used to measure the temperature difference across sections of the mask wall. Combining this with its thermal resistance and surface area A_{mask} allow the losses to be calculated as

$$Q_{mask} = \frac{A_{mask} \cdot \Delta T}{R_{mask}} \tag{3.6}$$

In a similar manner, wall losses are estimated. The active thermal guard produces a small, but oscillating temperature gradient across the wall. In this case, the average temperature gradient over the course of the test was used in Eq. (3.6). It should be noted that the R-factor in this case was from the calorimeter interior to the guard heater (which is located in the middle of the wall).

Seal and bridging losses were accounted for through calibration of the calorimeter. Seal losses occur at the mask wall and calorimeter junction. Bridging losses occur around the perimeter of the window sample, and are defined as the increase in heat transfer caused by the window and mask wall junction. These losses were incorporated into the data analysis spreadsheet based on the interior / exterior temperature difference.

3.2.1 Inward-Flowing Fraction Test

As shown in the previous section, energy flow in a typical window calorimeter may be estimated. A similar analysis may be used to estimate the losses occurring during the inward-flowing fraction test conducted under this study. Figure 3-7 shows a schematic of the energy balance for inward-flowing fraction tests.

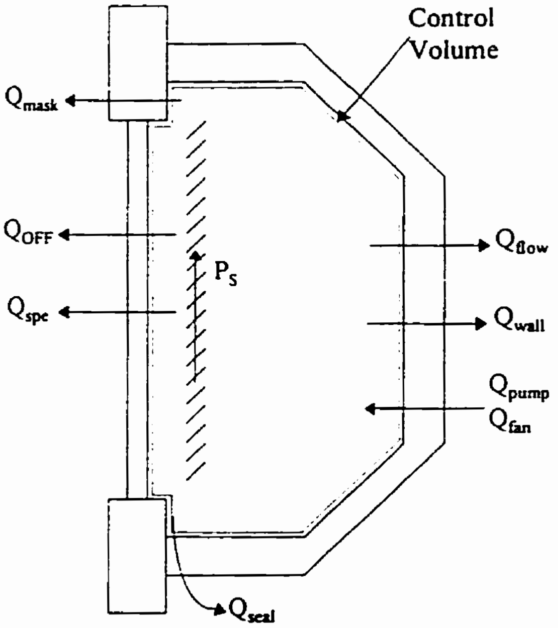

Figure 3-7. Calorimeter energy balance for inward-flowing fraction testing.

In equation form, the energy balance is represented by

$$P_s = Q_{flow} - Q_{fan} - Q_{pump} + Q_{OFF} + \sum Q_{loss} \tag{3.7}$$

In this case, we consider $Q_{input,}$ as expressed in Eq. (3.2), to be the blind input power P_S. It is important to note the inclusion of the outward-flowing fraction, Q_{OFF}, of energy supplied to the blind. Heat transfer through the window now consisted of losses driven by the air to air temperature difference, and the outward-flowing fraction. If we break the power input to the blind into its inward and outward components, Eq. (3.7) becomes

$$(1 - N_s)P_s + N_s \cdot P_s = Q_{flow} - Q_{fan} - Q_{pump} + Q_{OFF} + \sum Q_{loss} \tag{3.8}$$

where $(1-N_S)P_S = Q_{OFF}$. It is also important to note that the losses through the specimen, Q_{spe}, are determined from the air to air temperature difference, and not by the glass surface temperatures. In this way, the outward-flowing fraction was not incorporated as a loss, while losses due to an air to air temperature difference was. Q_{spe} was estimated by

$$Q_{spe} = \frac{A_{spe}}{\frac{1}{h_o} + R_{spe} + \frac{1}{h_i}}(T_i - T_o) \tag{3.9}$$

Equation (3.8) becomes

$$N_s \cdot P_s = Q_{flow} - Q_{fan} - Q_{pump} + \Sigma Q_{loss} \tag{3.10}$$

$$N_s = \frac{\left(Q_{flow} - Q_{fan} - Q_{pump} + \Sigma Q_{loss}\right)}{P_s} \tag{3.11}$$

3.2.2 Test Uncertainty

An uncertainty analysis was performed on the experimental data based on the propagation of the estimated component uncertainties according to the method of Kline and McClintock [52]. Details of the method and the uncertainty analysis can be found in Appendix C.

3.3 Heat Transfer Coefficient Determination

To aid in determining heat transfer coefficients, both with and without an installed blind, a "calibration transfer standard" was built based on the National Research Council Canada / Division of Building Research (NRCC / DBR) recommendations [42]. This consisted of a window specimen constructed using foam insulation as a core. Thermocouple sensors were placed in coincident locations on either side of the core, under the glass, to measure the temperature drop across the foam core. The calibration transfer standard is as shown in Fig. 3-8. With knowledge of the foam core's thermal conductivity [53], and by inducing a temperature gradient across it, interior and exterior heat transfer coefficients, and heat flux through the core can be determined. Calibration is then accomplished by comparison of the calculated heat flow through the calibration transfer standard with that determined from an energy balance on the calorimeter.

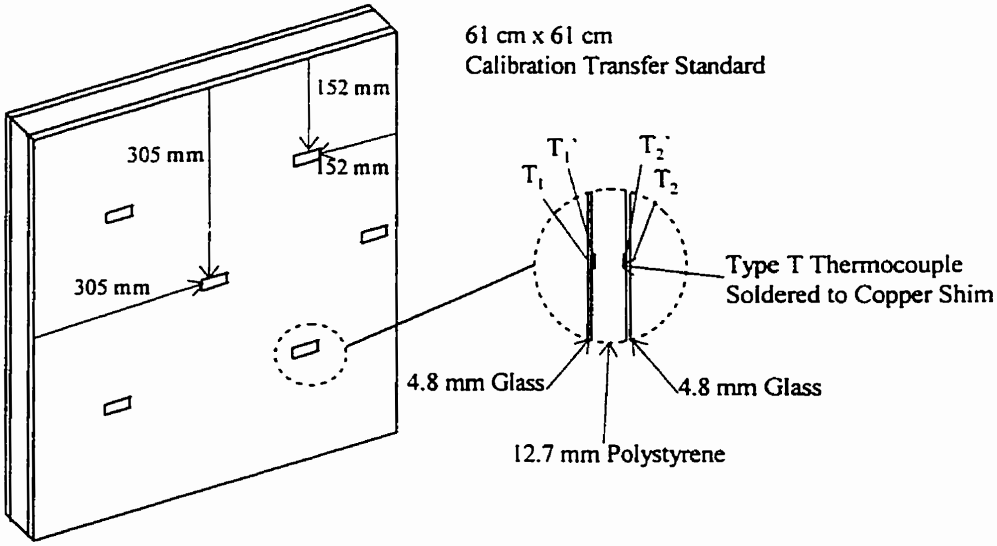

Figure 3-8. Calibration transfer standard schematic [42].

From the data collected, Q_{spe} was determined from

$$Q_{spe} = q_{spe} \cdot A_{spe} = A_{spe} \cdot C_{cor} \cdot \Delta T_{cor} \tag{3.12}$$

where C is the conductance, and the subscript *cor* denotes the polystyrene core of the calibration specimen. The surface temperatures of the glass were then determined by

$$T_1 = T_1' + \frac{C_{cor}}{C_g} \Delta T_{cor} \tag{3.13}$$

$$T_2 = T_2' + \frac{C_{cor}}{C_g} \Delta T_{cor} \tag{3.14}$$

where $T_1, T_2 =$ the interior and exterior surface temperatures of the specimen

$T_1', T_2' =$ the interior and exterior surface temperatures of the specimen core

A goal of this study was to develop an empirical model. To assist in this task, sufficient instrumentation was installed to determine the heat transfer coefficients associated with each calculated N_S value. The data recorded from these sensors were subsequently used as input to the resistance model proposed by Farber et. al. [8].

The use of a calibration transfer standard was integral to this analysis. It was decided that it be used for testing rather than a real window for three reasons: (1) the instrumentation present in the sample allowed easy determination of the glass surface temperatures, temperature distribution, and heat flux; (2) the calibration specimen has a comparable R-factor (0.397 W/m^2K) to that of a real window (0.31-0.63 W/m^2K) [1], and (3) optics were not being investigated so the presence of a foam core should not be problem.

3.3.1 Exterior Air Film Coefficient Determination

External air film coefficients were calculated in order to determine the operating parameters of the wind generator used for this study, and to provide data for the model.

Using the values calculated from Eqs. (3.12) and (3.14), h_O was determined as

$$h_O = \frac{Q_{spe}}{(A_{spe}(T_2 - T_o))} \tag{3.15}$$

3.3.2 Heat Transfer Coefficient Determination for a Shading Layer

The modifications in the model by Farber et. al. [8], shown in Fig. 3-9, reflect the difference between a room and the calorimeter. Rather than assuming a uniform wall and air temperature, the model was changed to reflect the temperature difference between the absorber plate and the air, i.e., the air and surrounding room were not assumed to have the same temperature. This would make calculated heat transfer coefficients more accurate for use in the predictive model given in Fig. 1-2.

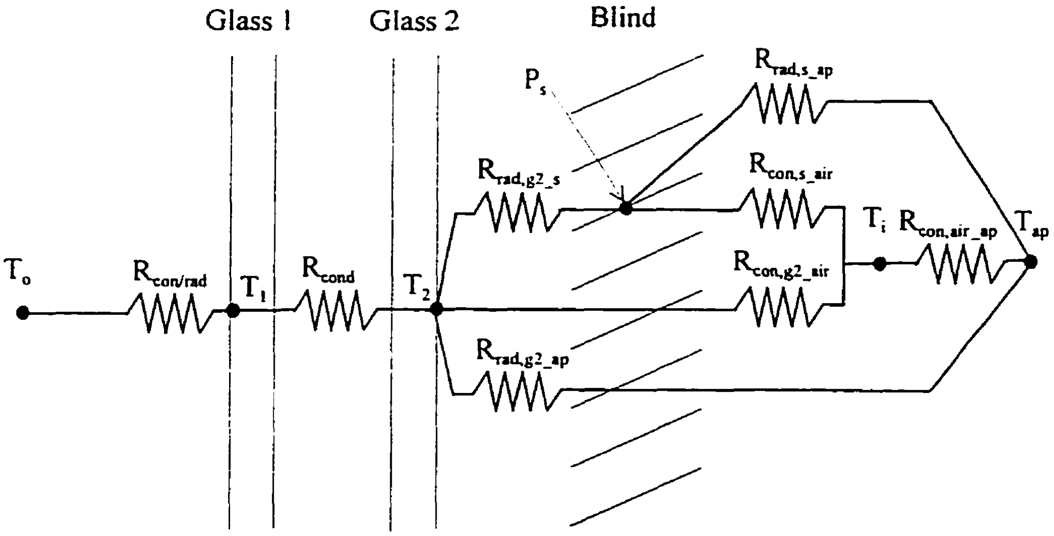

Figure 3-9. Modified thermal circuit for calibration specimen with venetian blind in Queen's solar calorimeter. The model assumes that the air temperature between the glass and the shade is the same as the room air temperature. R = 1/h.

Radiative absorption factors were estimated using a radiation view factor add-in program for AUTOCAD™ called RADCAD™ [54]. Values were confirmed using tables from Parmelee et. al. [16]. Estimated radiative absorption factors are shown in Table 3-1. Results from the RADCAD™ program have been included in Appendix A and Table 3-1.

Table 3-1. Estimated radiative interchange factors (F_{1_2}) from Parmelee et. al. [16] and RADCAD™.

h (W/m^{2}K)	Slat Angle							
	-45°		0°		45°		70°	
	Parmelee	RADCAD	Parmelee	RADCAD	Parmelee	RADCAD	Parmelee	RADCAD
glass to blind	0.71	0.68	0.64	0.60	0.71	0.68	0.81	0.83
glass to absorber	0.14	0.19	0.21	0.29	0.14	0.19	0.04	0.05
blind to absorber	0.67	0.62	0.60	0.52	0.67	0.62	0.77	0.77

Radiative heat transfer coefficients were calculated using the equation

$$h_{rad} = \frac{\sigma(T_2^4 - T_1^4)}{A_1(T_2 - T_1)} \cdot \left(\Sigma(1-\varepsilon_i)/\left(A_i\varepsilon_i\right) + 1/(F_{1\_2}A_1)\right)^{-1} \tag{3.16}$$

where h_{rad} = radiative heat transfer coefficient
F_{1_2} = radiation interchange factor between surface 1 and 2
σ = Stephan-Boltzman constant
ε_i = Emissivity (0.75 for the blind and 0.86 for glass)

and where the temperatures of surfaces 1 and 2 were taken from data collected during each experiment. The heat flux along these paths was then calculated as

$$\frac{Q_{rad}}{A} = q_{rad} = h_{rad} \cdot \Delta T \tag{3.17}$$

The determination of convective heat transfer coefficients was accomplished by performing an energy balance at the inner glass surface, and at the blind surface. At the glass surface, Eq. (3.16) was used to calculate radiative flux, and Eq. (3.12) was used to calculate heat flow through the calibration specimen. The energy balance becomes

$$Q_{con,g2\_air} = -Q_{rad,g2\_s} - Q_{spe} - Q_{rad,g2\_ap} \tag{3.18}$$

where *con* is convective heat flux, and *ap* is the absorber plate. The convective heat transfer coefficient is

$$h_{con,g\_air} = \frac{-Q_{rad,g2\_s} - Q_{spe} - Q_{rad,g2\_ap}}{A_{g2}(T_{g2} - T_{air})} \tag{3.19}$$

The energy balance at the shade is

$$Q_{con,s\_air} = P + Q_{rad,g2\_s} - Q_{rad,s\_ap} \tag{3.20}$$

Based on the surface area of the glass, the convective heat transfer coefficient is

$$h_{con,s\_air} = \frac{P + Q_{rad,g2\_ap} - Q_{rad,s\_ap}}{A_{g2}(T_s - T_{air})} \tag{3.21}$$

Temperatures given in Eq. (3.21) were measured during testing. Thermal resistances were calculated using Eq. (1.4), and the system's R-factor becomes

$$R = \left\{ \left[\left(\frac{1}{R_{rad,s\_ap}} + \frac{1}{R_{con,s\_air}} \right)^{-1} + R_{rad,g2\_s} \right]^{-1} + \frac{1}{R_{con,g2\_air}} + \frac{1}{R_{rad,g2\_ap}} \right\}^{-1} + R_a + R_o \tag{3.22}$$

Farber et. al. [8] assumed that the wall and room temperatures are the same. In this case, the network given in Fig. 3-9 reduces back to the model shown in Fig. 1-2. The energy balance could then be solved using the matrix technique presented by Farber et. al. [8], using the experimentally determined heat transfer coefficients. A full description of this method can be found in reference [8] and Appendix A.

3.4 Test Series

The main intentions of the experimental test sequence were to measure the inward-flowing fraction of a venetian blind with respect to slat angle, and to quantify the effects of external variables. While geometric considerations, such as nominal distance from the window, were not examined due to time constraints, factors such as the level of absorbed irradiation, internal / external temperature difference, and external wind speed or external air film coefficient were analyzed. The test sequence was also intended to collect sufficient data for the determination of heat transfer coefficients between the inner glazing and the room. These coefficients were necessary for the development of an empirical model.

During a test sequence, all three of these intentions could be fullfilled simultaneously. Each test for variable dependency was performed at each of the desired slat angles. For every one of these tests, sufficient data was taken to allow the determination of heat transfer coefficients around the shade layer.

As previously stated, the test method for inward-flowing fraction should be relatively simple when compared to other calorimetric tests. Klems and Kelley [10] conclude that N_S does not appear to be dependent on temperature or level of absorbed irradiation. Parmelee et. al. [15] also made this observation during their tests. They stated that "Experimental work showed that the increase of convection and radiation gain caused by the addition of an indoor shade to common glass was proportional to the solar radiation absorbed by the combination". If this is indeed the case, there should be no need to have any temperature difference across the window, or to irradiate the specimen. Klems and Kelley [10] also stated that wind conditions (h_O) did not have a strong effect on N_S, and that it was possibly compensated for by other variables. One of the goals of this research, however, was to quantify the magnitude of how external factors (i.e., h_O, ΔT, P) affected the inward-flowing fraction for a shading layer. The test series described here were designed to test the effects of these assumptions.

A factorial experiment [11, 12] was chosen to examine these dependencies. Specifically, a face-centered central composite experimental design was laid out to investigate the level of interaction between h_O, ΔT, and P with N_S. Consequently, a series of tests was planned as shown in Fig. 3-10. Such an experiment can be used to examine any series of three variables that are expected to show linear or quadratic effects when they interact. This factorial design was chosen because it could show the interaction of external factors on inward-flowing fraction with a minimum amount of testing. As stated by Klems and Kelley [10], interactions were assumed to have little or no effect. Proof of this would lend validity to the test design.

One additional modification was made to the test series. A single test sequence was run with the fan turned off for each slat angle. The low external heat transfer coefficient created in this test allowed the effect of the exterior film resistance to become more pronounced. Table 3-2 lists the test conditions we used for each test sequence. Each set of tests was repeated for a series of shade angles.

The various test conditions will be more fully described in the following sections.

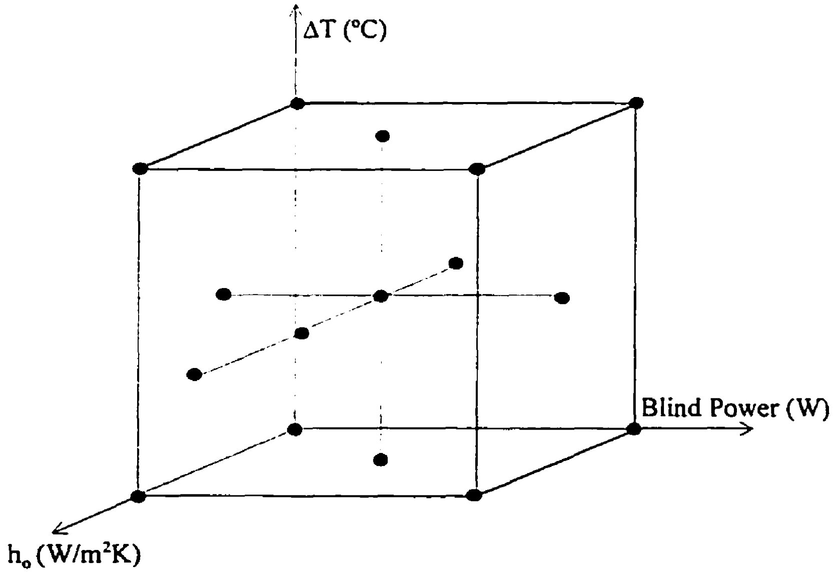

Figure 3-10. Test conditions for face-centered central composite experiment design [11, 12].

Table 3-2. Approximate test conditions used in factorial experiment.

	Blind Power (W)	h_O (W/m^{2}K)	ΔT (°C)
Test #1	50	20	0
Test #2	50	30	0
Test #3	125	25	0
Test #4	200	20	0
Test #5	200	30	0
Test #6	50	25	5
Test #7	125	20	5
Test #8	125	25	5
Test #9	125	30	5
Test #10	200	25	5
Test #11	50	20	10
Test #12	50	30	10
Test #13	125	25	10
Test #14	200	20	10
Test #15	200	30	10
Test #16	125	8	5

3.4.1 Absorbed Irradiance Test

To test the effects of absorbed irradiation, data was collected for three input power levels (50, 125, 200 W) in accordance with the previously mentioned test method. Each power level represented a different amount of absorbed solar energy. The low power level of 50 W is representative of a case corresponding to a reflective blind, whereas the maximum value of 200 W is representative of absorption in a darker, more absorptive blind. The power level of 200 W is representative of 800 W/m^2 passing through two clear glazings of a 0.37 m^2 window (the size of the test specimen).

3.4.2 Temperature Gradient Test

To test the dependence of the temperature gradient across the window assembly, the calorimeter interior temperature was controlled to produce the desired temperature difference relative to the exterior temperature. While it would be preferable to maintain room conditions within the calorimeter and cool the surroundings, the equipment being used did not have that capability. The maximum temperature difference achievable was 10 °C. Tests were run at 0, 5, and 10 °C temperature differences as shown in Table 3-2.

3.4.3 Exterior Air Film Coefficient Test

Klems and Kelley [10] noted that a change in exterior wind speed had little effect on the inward-flowing fraction, but suspected that there were compensating factors involved. It was expected that higher wind speeds will decrease the inward-flowing fraction by decreasing the thermal resistance to the environment.

To test the effect of the exterior air film coefficient, two axial fans were positioned 4 meters in front of the mask wall to produce air flow parallel to the floor and perpendicular to the test sample surface. The external air-film coefficient could be measured directly by the CTS. The fan speed, and therefore the external film coefficient, was adjusted using the values shown in Tables 3-2 and C-7.

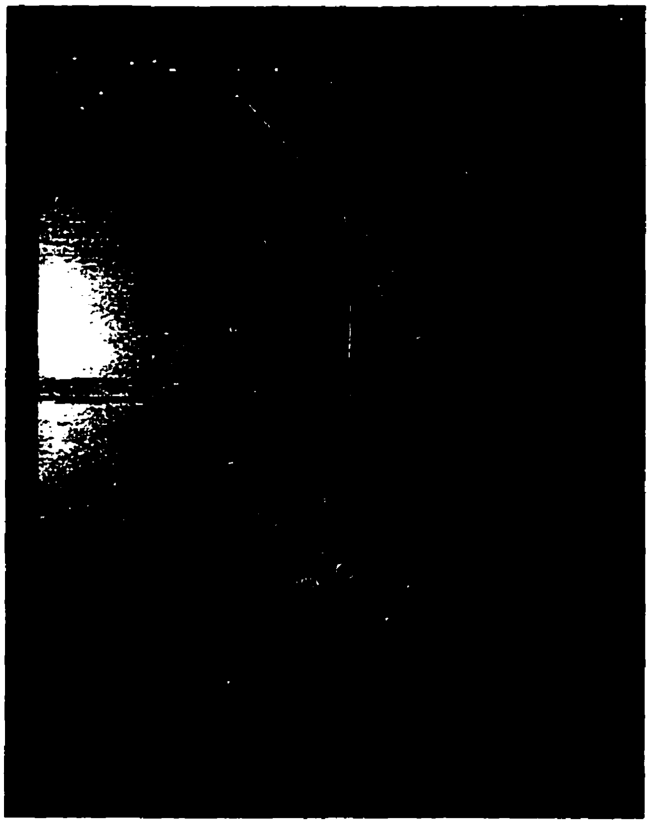

Figure 3-11: The wind generator used during testing.

3.5 Test Setup

The following procedure was followed in setting up and conducting an inward-flowing fraction test.

The specimen was mounted as shown in Fig. 3-12. It was decided from the onset, that the installation of the specimen should be representative of an actual window installation [55]. In that regard, a simple plywood casing was put around the specimen both to protect the mask wall, and to partially simulate the frame. A 25.4 mm square block braced the window from the exterior side. The entire unit was inserted into the mask wall, and shimmed to a tight fit. Any spaces were then filled with insulation, and the inner and outer seams were taped. Due to hardware limitations, only 4 thermocouples were monitored: two on each side of the specimen, with one set each at the center and edge.

A standard aluminum blind with a typical slat geometry and white enameled surface was chosen for the tests. Each slat was 2.54 cm wide and 60.96 cm long. Aluminum blinds were used because they were electrically conductive. Each blind slat was wired together in series to provide the maximum resistance possible. This resulted in a total resistance of about 0.40 ohms, 10% of which was due to the connecting wires. It was assumed that the heat produced by the resistance of these connecting wires would conduct back along the blind slats, and thereby have little effect on the overall results.

Blind installation details are shown in Fig. 3-13. The blind was mounted 17 mm from the inner side of the window, as it would be in a real situation. The slat angle was set to the desired test angles of -45, 0 45, or 70°.

Temperature metering devices were placed in the following manner. Four thermocouples with radiation shields were dedicated to measuring air within the calorimeter. Each was placed at the center of a quadrant defined by the vertical and horizontal centerlines of the calorimeter. Two thermocouples were installed to meter the temperature of the absorber plate. Two more were placed on the blind to measure its temperature. The blind temperature was metered in locations corresponding to window temperature measurements. Mask temperatures were metered in coincident locations both inside and out at two locations along the vertical centerline. One was above the sample, and one below. Extra thermocouples were added to measure the two external mask temperatures, and the ambient air temperature. The air sensing thermocouple was fitted with a radiation shield and was placed at a distance of 75 mm from the center of the window as per reference [45].

To run a test, the following procedure was followed. After starting the DA system, the wind generator was set to supply the required air velocity normal to the window surface. Next, the bath and cooling units were turned on. Once the conditioning loop was controlling to the desired set point, the guard heaters, positive displacement pump, and internal power to the internal fans and pump were started. Finally, the blind power was turned on and adjusted to the desired test level.

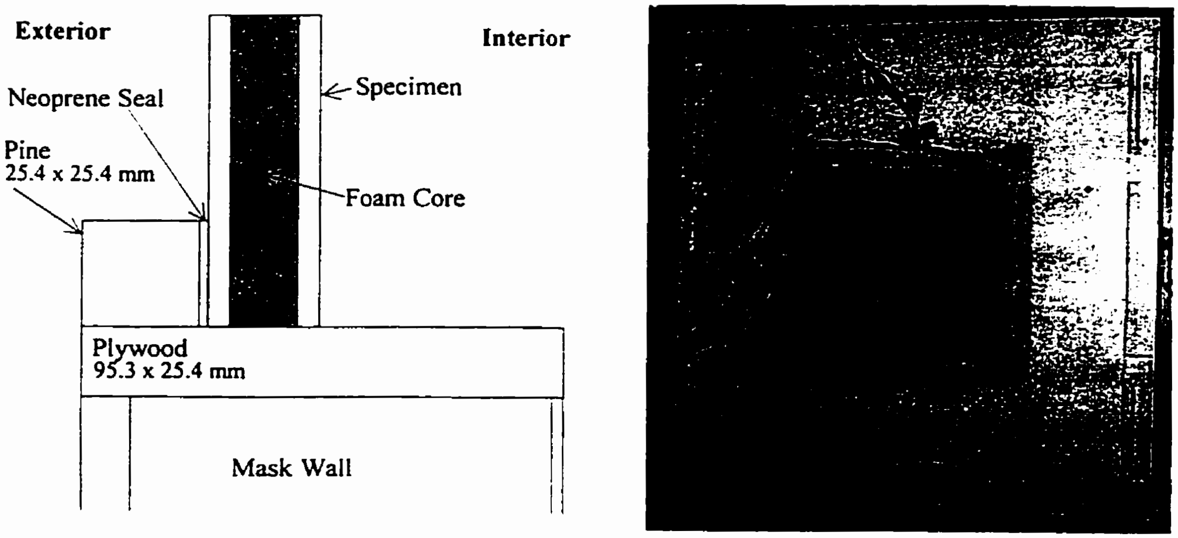

Figure 3-12. Calibration specimen installation details [55] and photo of the installed calibration transfer standard.

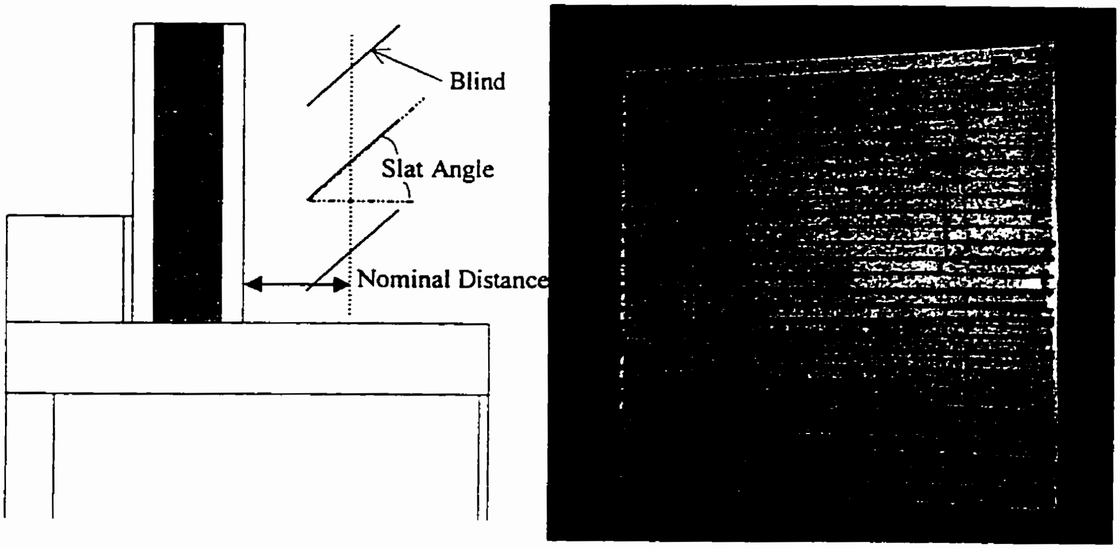

Figure 3-13. Blind installation details [55] and photo of the installed blind.

Stability criterion was based both on accepted practice and calorimeter performance. Due to the relatively fast system response of the calorimeter (Appendix B), the long test periods typically associated with guarded hot box tests were not necessary. Thermal response tests showed that 5 time constants (or 99% of full response) was achieved in approximately 40 minutes. Once the system was given time to respond to a new set of test conditions, steady state conditions were determined based on solar heat gain tests using artificial irradiation [46]. In order to achieve steady state conditions, the heat transfer fluid was circulated through the absorber plate at the appropriate values for inlet temperature and flow rate until they remained constant within ± 0.3 °C and ± 1 W/°C, respectively, for 15 minutes prior to each period in which the data was taken, and for the 15 minutes in which data was collected. Based on this, tests were run a minimum of 2 hours.

CHAPTER 4

EXPERIMENTAL RESULTS

As discussed in Chapter 3, tests were conducted over a range of conditions and blind geometries. Data were collected to determine both the inward-flowing fraction, and the heat transfer coefficients around the shading layer. An analysis of that data is contained in the following sections.

4.1 Typical Test Results

An example of the test results recorded over a time interval of 2 hours demonstrates the stability of recorded data and is helpful in determining the performance of the test apparatus. It also aids in the visualization of what occurs during a test.

Test #16 (125 W, 5 °C, 8 W/m^2K) for a 45° slat angle was chosen for this analysis. This test was chosen because it was mid-range in the temperature and blind power variables. The response of the system, in this case, can be seen in Figs. 4-1 to 4-6.

Accurate flow metering was important for this analysis. The stability of measured flow and temperatures, and proof of steady-state conditions were essential in calculating reliable results. Figure 4-1 shows the transient response of metered flow variables and calculated energy removed by the flow loop. Note that to account for the digital nature of the pulse counter, flow rate has been calculated using the average of three time-steps.

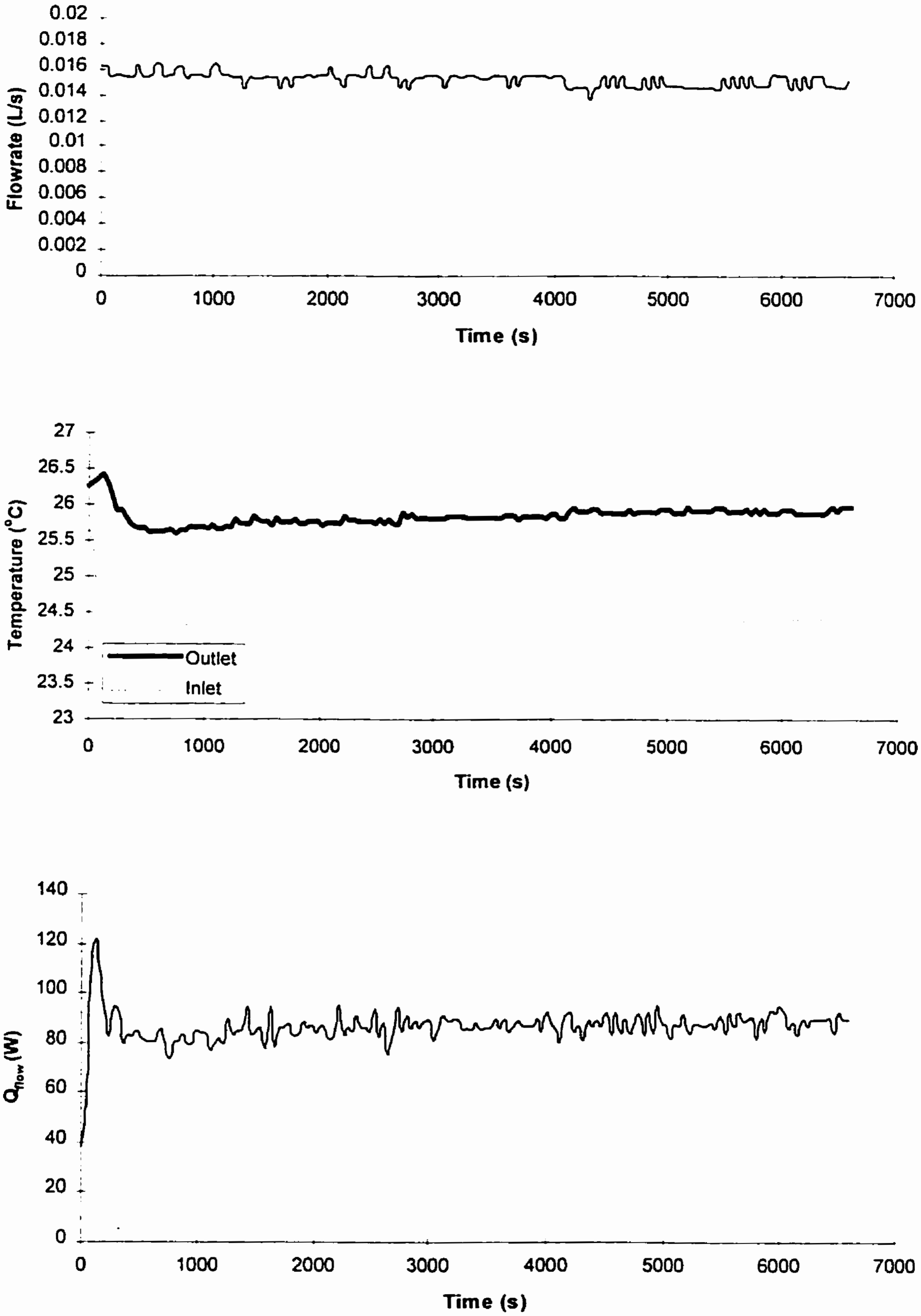

Figure 4-1. Typical test response of flow variables, and calculated energy removed by the flow loop for test #16 with a 45° slat angle.

The stability of all power sources was also a concern. Fluctuations in energy input to the calorimeter could slow the calorimeter response time, and cause inaccuracies in the data. Figures 4-2 and 4-3 show the measured power to the pump and fan, and to the blind respectively.

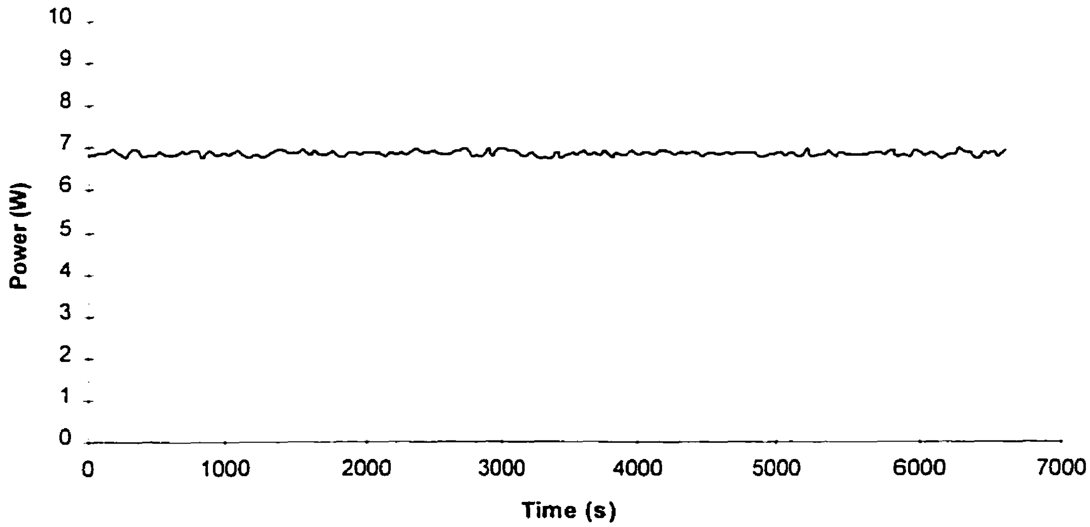

Figure 4-2. Power metering of pump and fan for test #16 with a 45° slat angle.

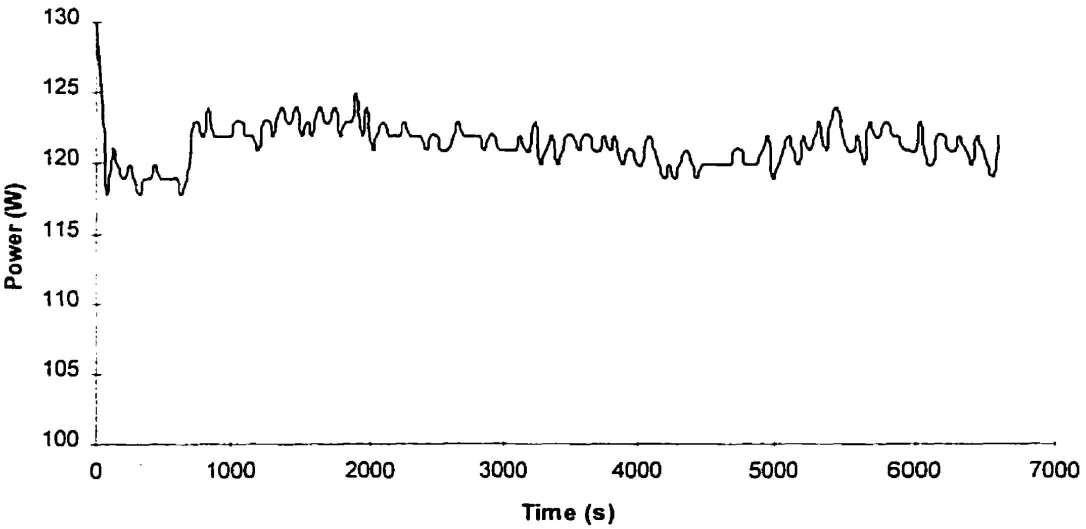

Figure 4-3. Power metering of blind power for test #16 with a 45° slat angle.

The success of the heaters in maintaining a negligible temperature gradient across the walls is integral to the reduction of losses. Figure 4-4 shows the response of just one heater (located at the center-back of the calorimeter). All other heaters performed with a similar frequency and magnitude of temperature oscillation.

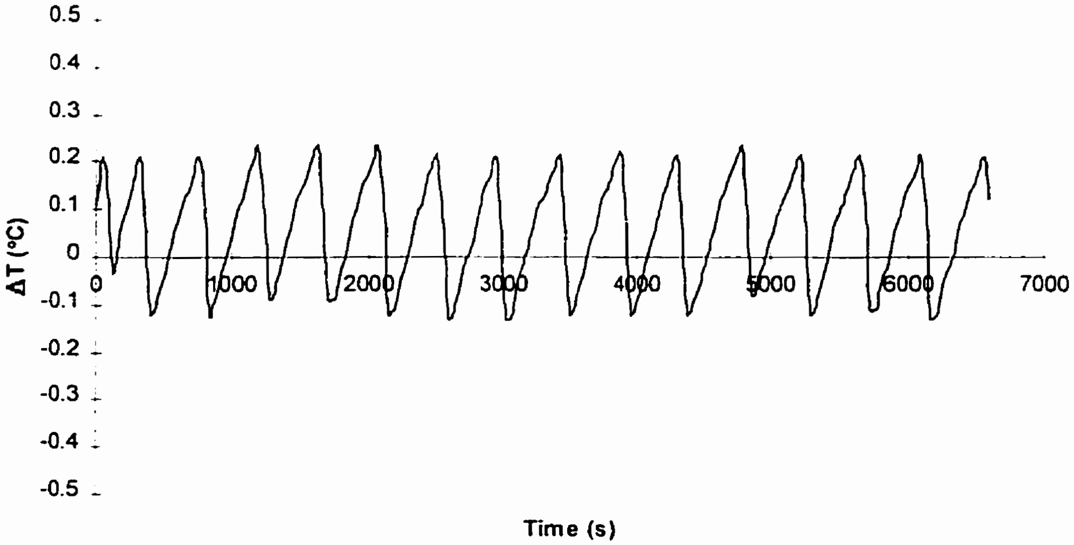

Figure 4-4. Thermal guard performance for test #16 with a 45° slat angle.

The stability of the blind temperature and the response of other temperatures in relation to a change in blind temperature was important to this analysis. Figs. 4-5 and 4-6 show the response of the average interior and exterior temperatures respectively.

Complete test data was analyzed and summarized, and presented as Appendix D.

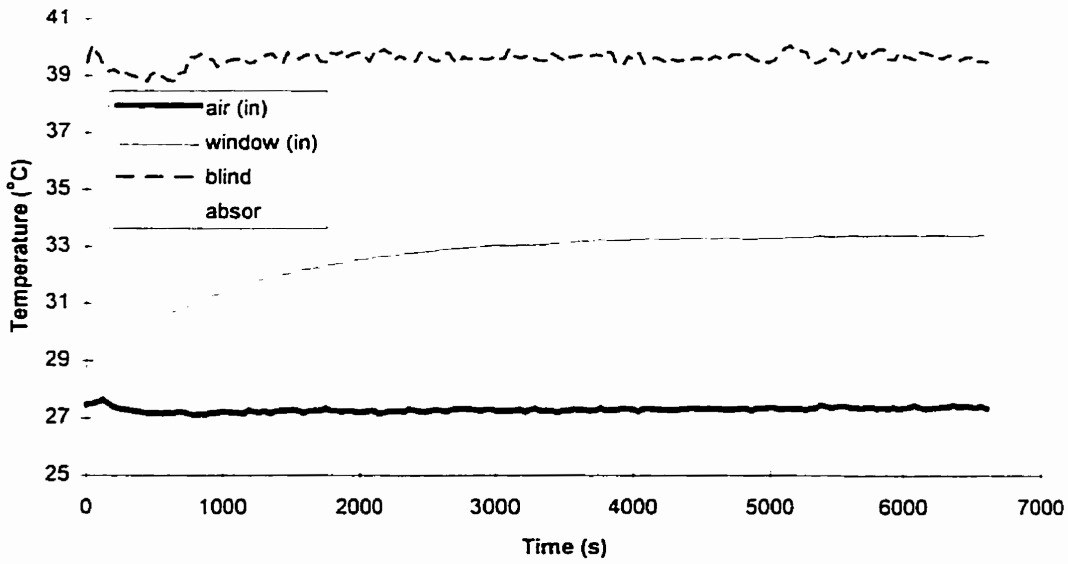

Figure 4-5. Response of interior air and surface temperatures for test #16 with a 45° slat angle.

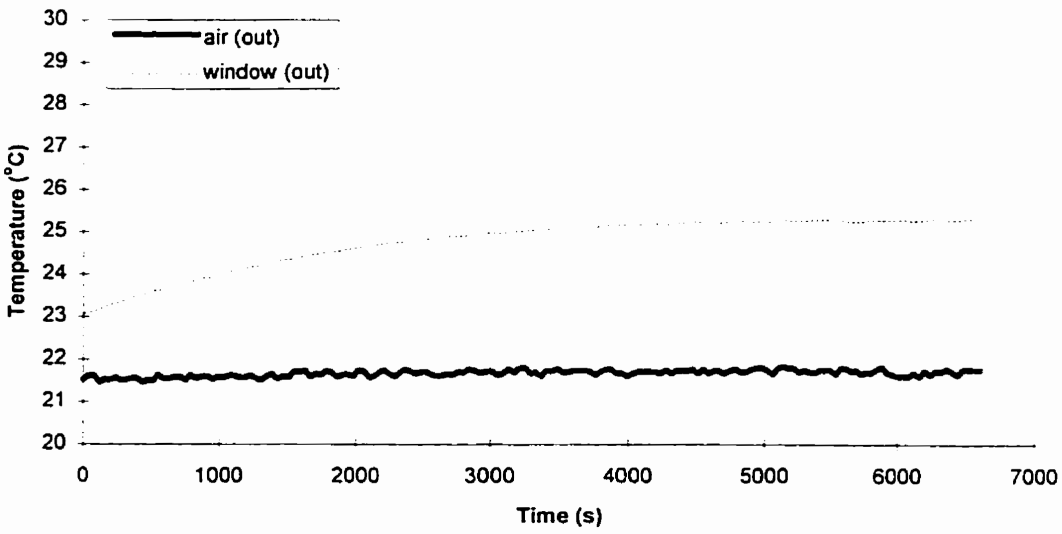

Figure 4-6. Response of exterior air and window temperatures for test #16 with a 45° slat angle.

4.2 Steady-State Results

Test results are presented in the context of the factorial experiment. Figure 4-7 shows the results for the test series at each slat angle. Test conditions are described in Table 3-2.

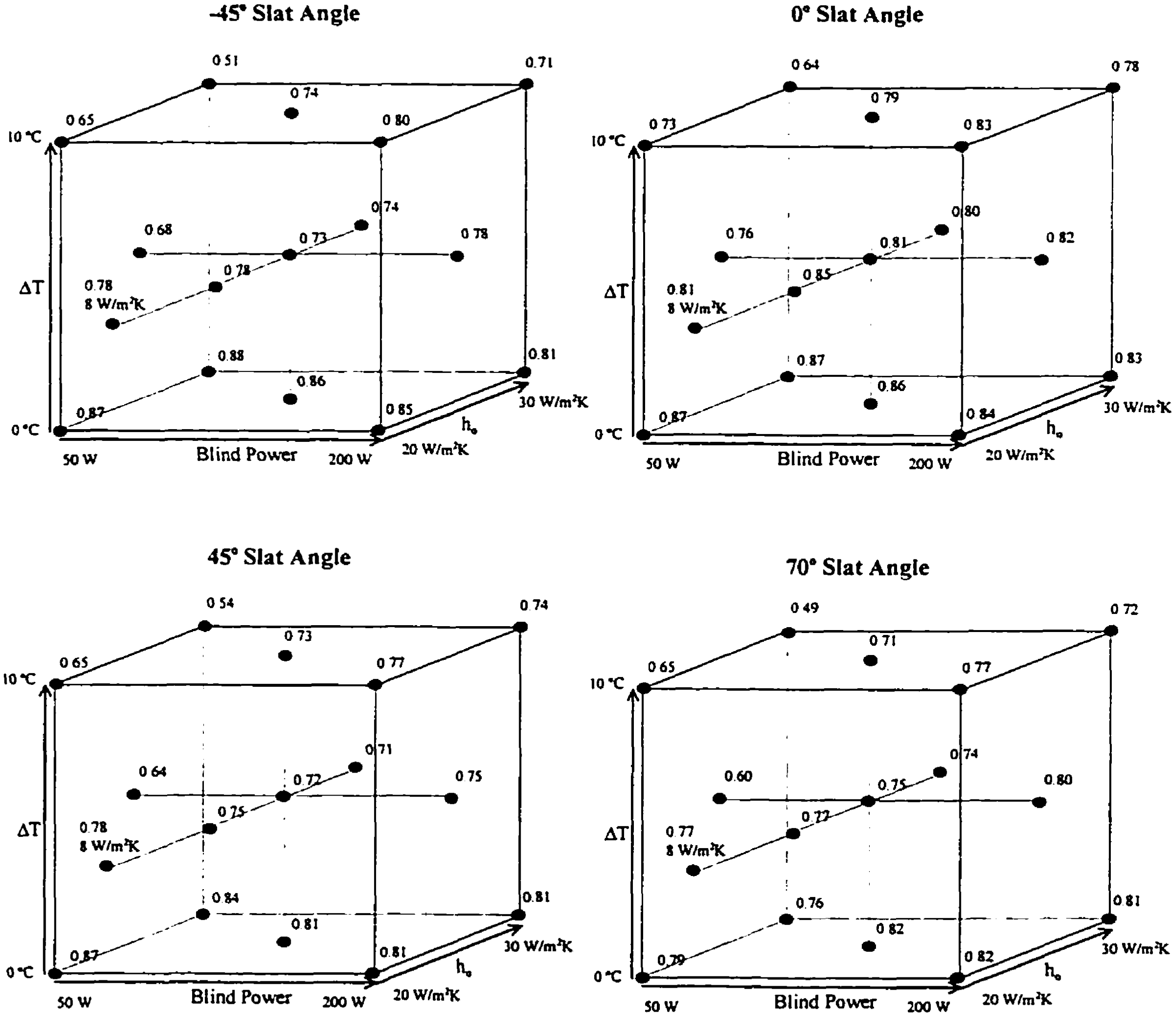

Figure 4-7. Complete results for all tests. Approximate test conditions are as shown on axis.

Table 4-1. Summary of Inward-Flowing Fraction test results for all slat angles. Result uncertainties are as indicated.

			N_S			
Test Conditions			Slat Angle			
P (W)	h^o (W/m^{2}K)	ΔT (°C)	-45°	0°	45°	70°
50	20	0	0.87±0.13	0.87±0.14	0.87±0.13	0.79±0.15
50	30	0	0.88±0.18	0.87±0.17	0.84±0.12	0.76±0.15
125	25	0	0.86±0.07	0.86±0.07	0.81±0.07	0.82±0.07
200	20	0	0.85±0.04	0.84±0.05	0.81±0.03	0.82±0.05
200	30	0	0.81±0.04	0.83±0.05	0.81±0.03	0.81±0.05
50	25	5	0.68±0.15	0.76±0.10	0.64±0.13	0.60±0.14
125	20	5	0.78±0.07	0.85±0.07	0.75±0.05	0.77±0.07
125	25	5	0.73±0.07	0.81±0.07	0.72±0.05	0.75±0.07
125	30	5	0.74±0.07	0.80±0.07	0.71±0.05	0.74±0.07
200	25	5	0.78±0.04	0.82±0.04	0.75±0.03	0.80±0.05
50	20	10	0.65±0.17	0.73±0.19	0.65±0.14	0.65±0.17
50	30	10	0.51±0.18	0.64±0.18	0.54±0.14	0.49±0.16
125	25	10	0.74±0.07	0.79±0.07	0.73±0.06	0.71±0.07
200	20	10	0.80±0.04	0.83±0.05	0.77±0.04	0.77±0.05
200	30	10	0.71±0.04	0.78±0.04	0.74±0.05	0.72±0.05
125	8	5	0.78±0.06	0.81±0.06	0.78±0.05	0.77±0.06

4.2.1 Absorbed Irradiation Level Test Results

Calculated inward-flowing fraction was plotted verses input power. A linear regression line, weighted with respect to measured uncertainty, was fit to the data in an effort to exhibit any trends. Figures 4-8 to 4-11 show these plots for each slat angle. Figure 4-12 is a compilation of all N_S data as it relates to power input. Error bars represent the magnitude of uncertainty in each variable. Uncertainty values were evaluated for each data point based on the analysis presented in Appendix C.

Scatter and high uncertainty at the low power settings is clearly exhibited in these plots by the indicated uncertainty intervals. The effect is typical of all the measurements taken at low power levels, and is largely a result of uncertainties associated with the measurement of ΔT in the flow loop.

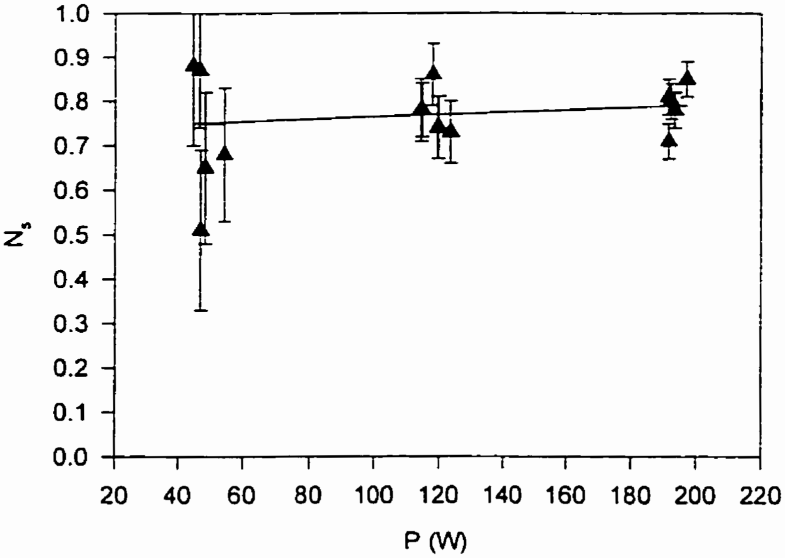

Figure 4-8. Inward-flowing fraction results plotted verses level of absorbed irradiation for a -45° slat angle.

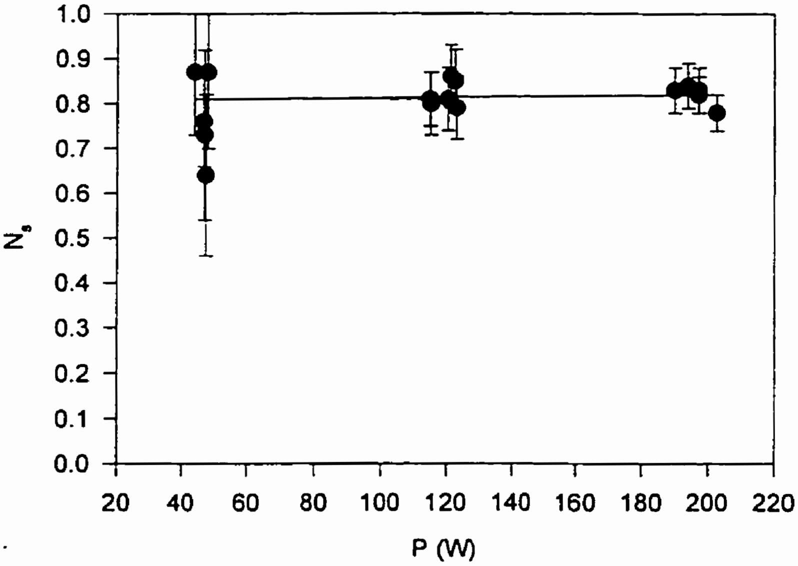

Figure 4-9. Inward-flowing fraction results plotted verses level of absorbed irradiation for a 0° slat angle.

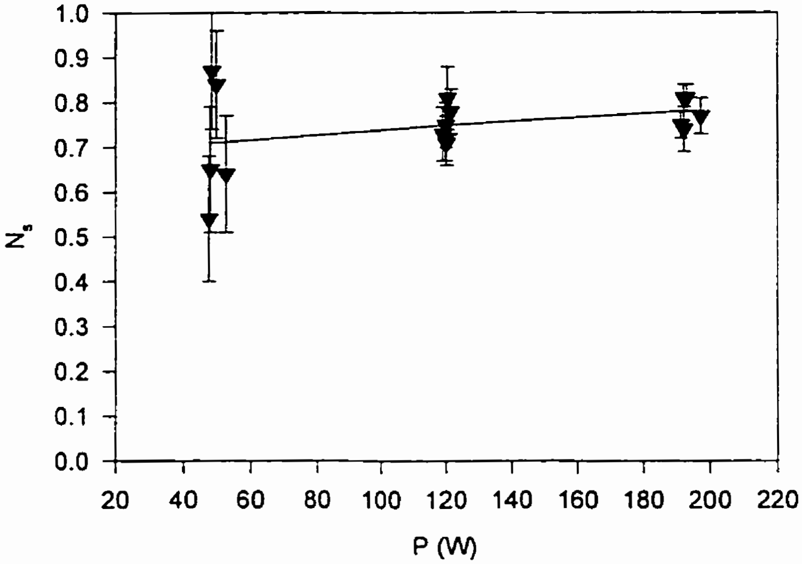

Figure 4-10. Inward-flowing fraction results plotted verses level of absorbed irradiation for a 45° slat angle.

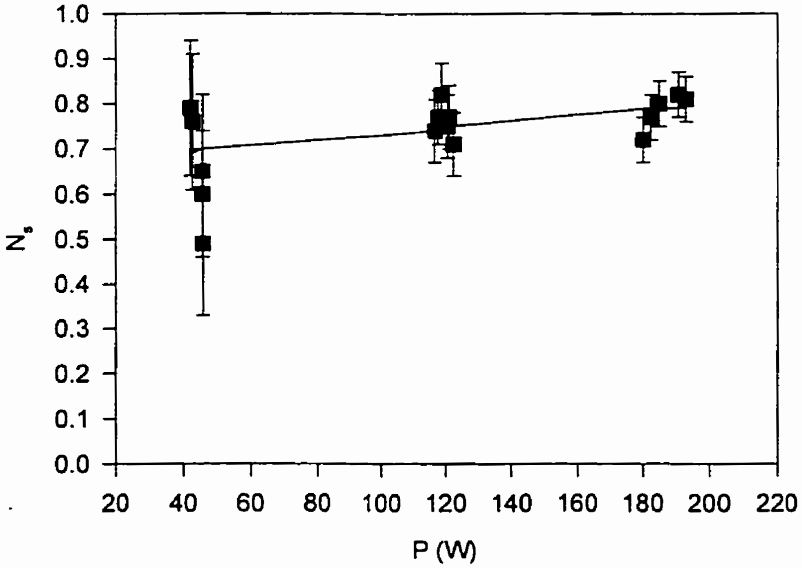

Figure 4-11. Inward-flowing fraction results plotted verses level of absorbed irradiation for a 70° slat angle.

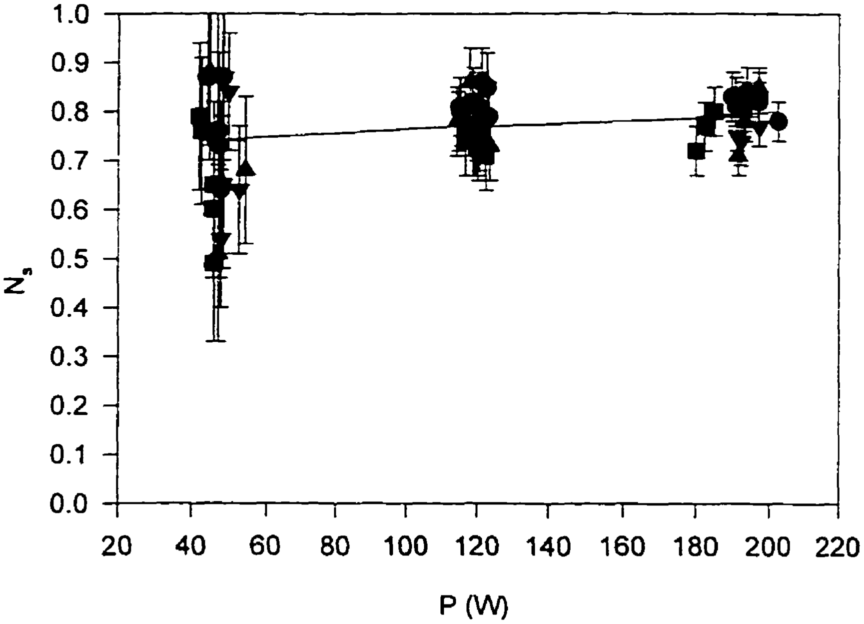

Figure 4-12. Inward-flowing fraction results plotted verses level of absorbed irradiation for all slat angles. ▲ -45° slat angle, ● 0° slat angle, ▼ 45° slat angle, ■ 70° slat angle.

4.2.2 Temperature Gradient Test Results

Calculated inward-flowing fraction was also plotted verses the interior / exterior temperature gradient in an attempt at determining any correlation between these variables. Figures 4-13 to 4-16 show these plots for each slat angle. Figure 4-17 is a compilation of all N_S data as it relates to the temperature differential.

A downward trend exists in the data for all slat angles. This suggests the temperature dependency of inward-flowing fraction. Such dependency will be investigated in the next chapter.

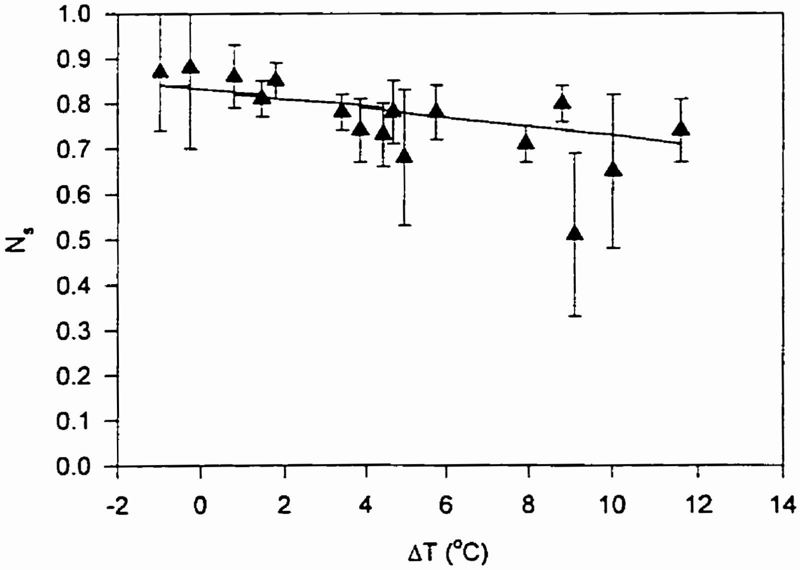

Figure 4-13. Inward-flowing fraction results plotted verses temperature gradient for a -45° slat angle.

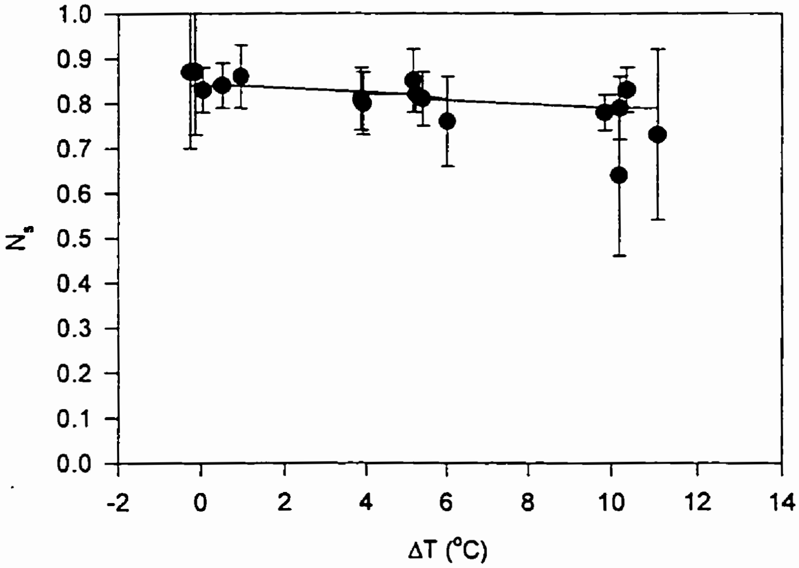

Figure 4-14. Inward-flowing fraction results plotted verses temperature gradient for a 0° slat angle.

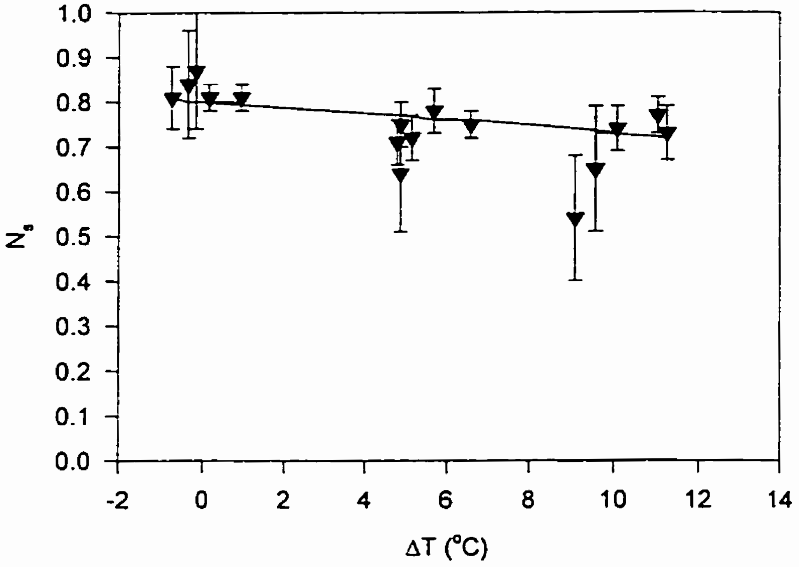

Figure 4-15. Inward-flowing fraction results plotted verses temperature gradient for a 45° slat angle.

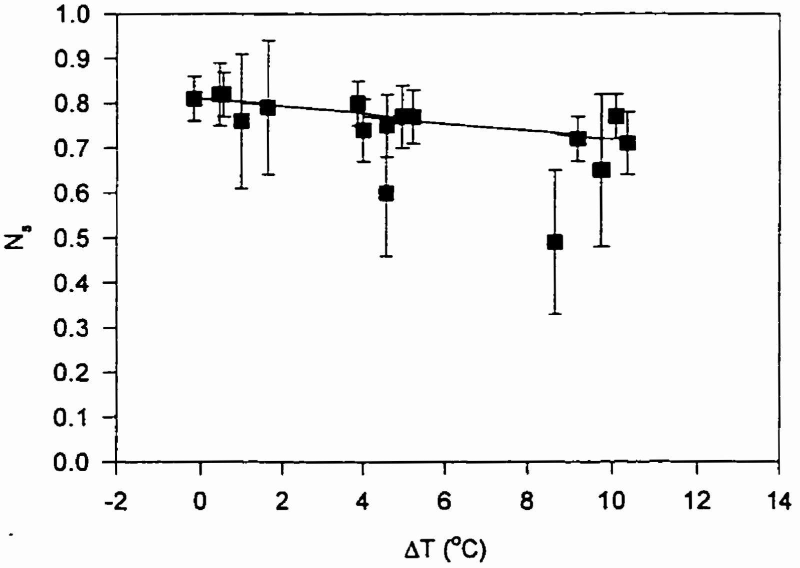

Figure 4-16. Inward-flowing fraction results plotted verses temperature gradient for a 70° slat angle.

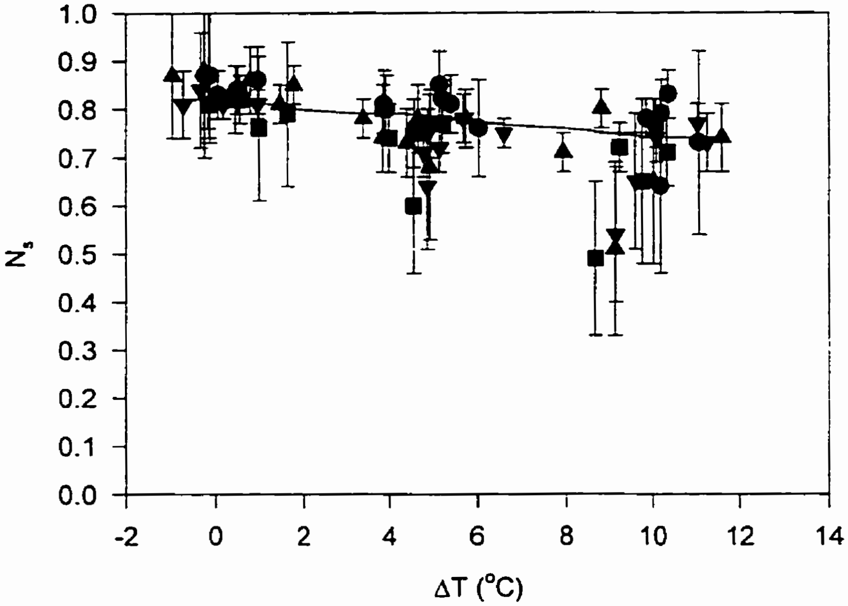

Figure 4-17. Inward-flowing fraction results plotted verses temperature gradient for all slat angles. ▲ -45° slat angle, ● 0° slat angle, ▼ 45° slat angle, ■ 70° slat angle.

4.2.3 Exterior Air Film Coefficient Test Results

Calculated inward-flowing fraction was again plotted verses the exterior air film coefficient to view any correlation between these variables. Figures 4-18 to 4-21 show these plots for each slat angle. Figure 4-22 is a compilation of all N_S data as it relates to the exterior air film coefficient.

Little effect is exhibited by these plots. While simple heat transfer theory would dictate a reduction in N_S as h_O increased, N_S proves to be only slightly dependent on this variable.

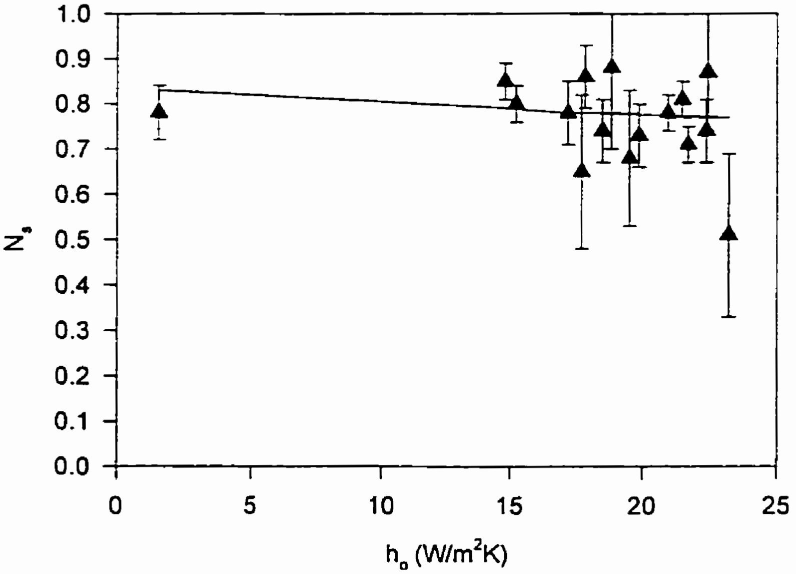

Figure 4-18. Inward-flowing fraction results plotted verses exterior air film coefficient for a -45° slat angle.

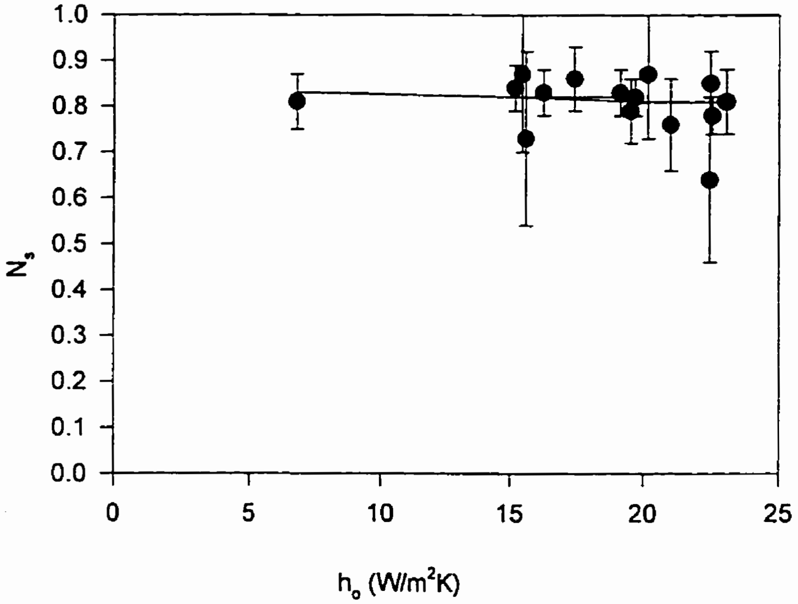

Figure 4-19. Inward-flowing fraction results plotted verses exterior air film coefficient for a 0° slat angle.

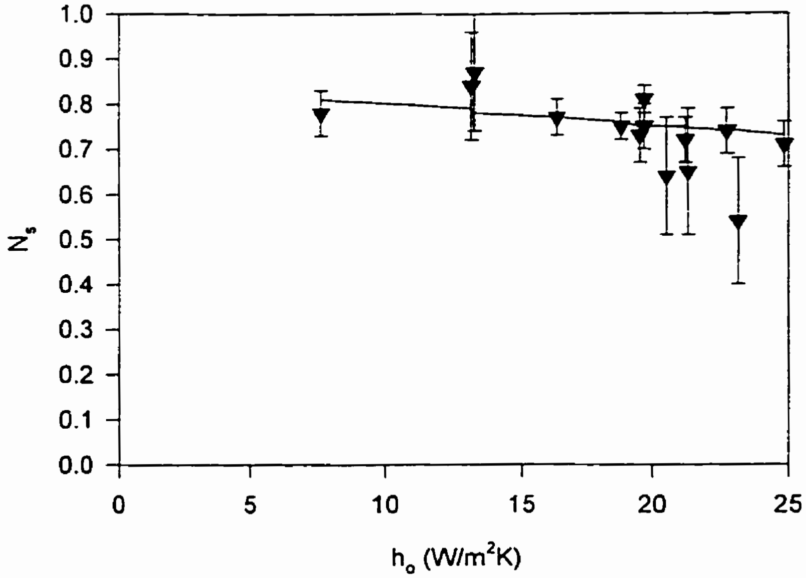

Figure 4-20. Inward-flowing fraction results plotted verses exterior air film coefficient for a 45° slat angle.

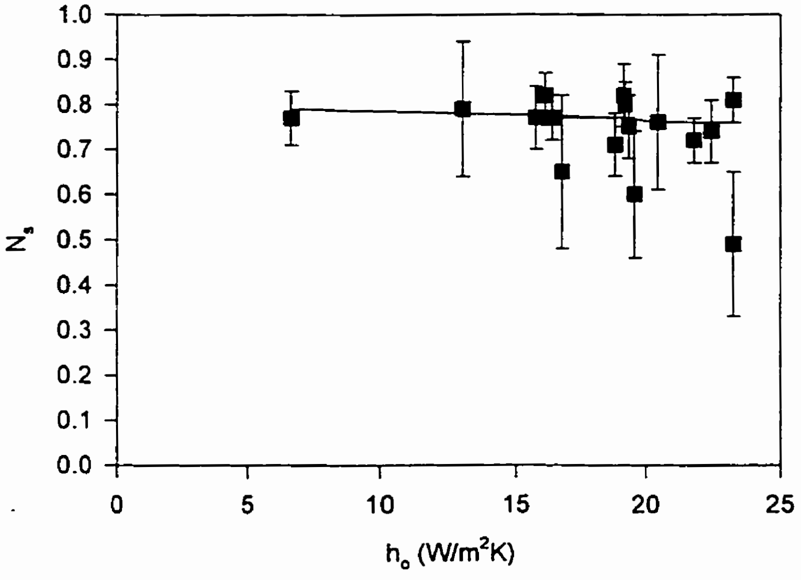

Figure 4-21. Inward-flowing fraction results plotted verses exterior air film coefficient for a 70° slat angle.

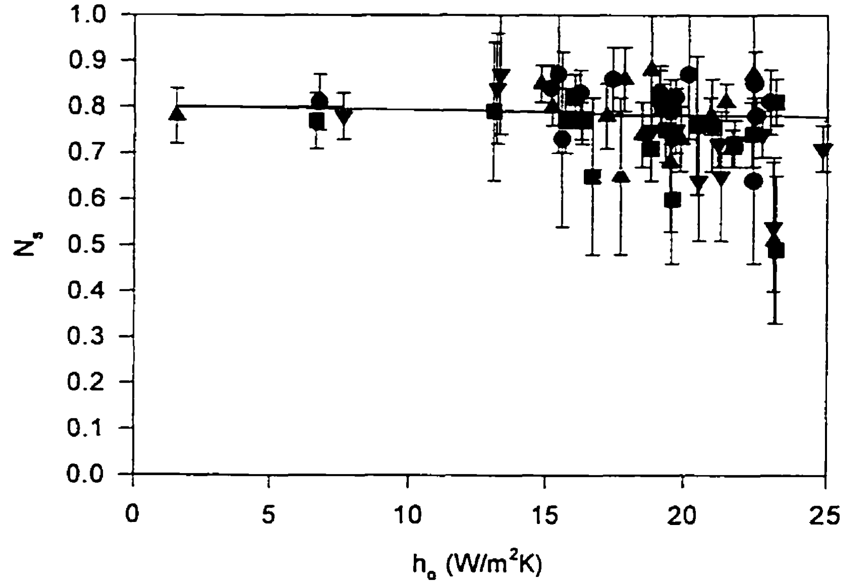

Figure 4-22. Inward-flowing fraction results plotted verses exterior air film coefficient for all slat angles. ▲ -45° slat angle, ● 0° slat angle, ▼ 45° slat angle, ■ 70° slat angle.

4.3 Interior Heat Transfer Coefficient Results

The examination of interior film coefficients was needed to produce approximate data for the development of a predictive model. Using the method described in Section 3.3, radiative and convective heat transfer coefficients were determined.

Convective and radiative heat transfer coefficients are represented using Figs. 4-23 to 4-30. All of these results were presented as a function of power input to the blind. Plots of convective and radiative heat transfer coefficients verses exterior air film coefficients or temperature gradients showed no clear trends between these variables.

A regression has been performed on each heat transfer coefficient at each slat angle. Equations of fit can be found in Figs. 4-23 to 4-30. When considering convective heat transfer from the glass to the air, however, plotted results generally showed little or no deviation from $h_{g2_air} = 0$W/m^{2}K. Accurate and repeatable measurement of this variable may require equipment modification.

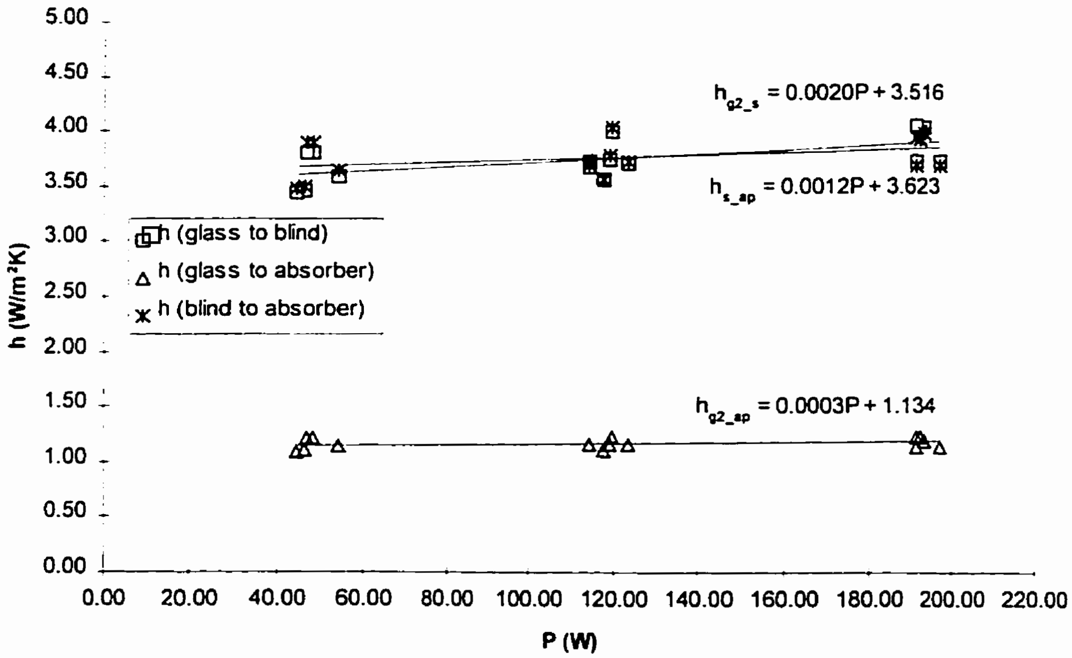

Figure 4-23. Calculated radiative heat transfer coefficients for a -45° slat angle as a function of blind power.

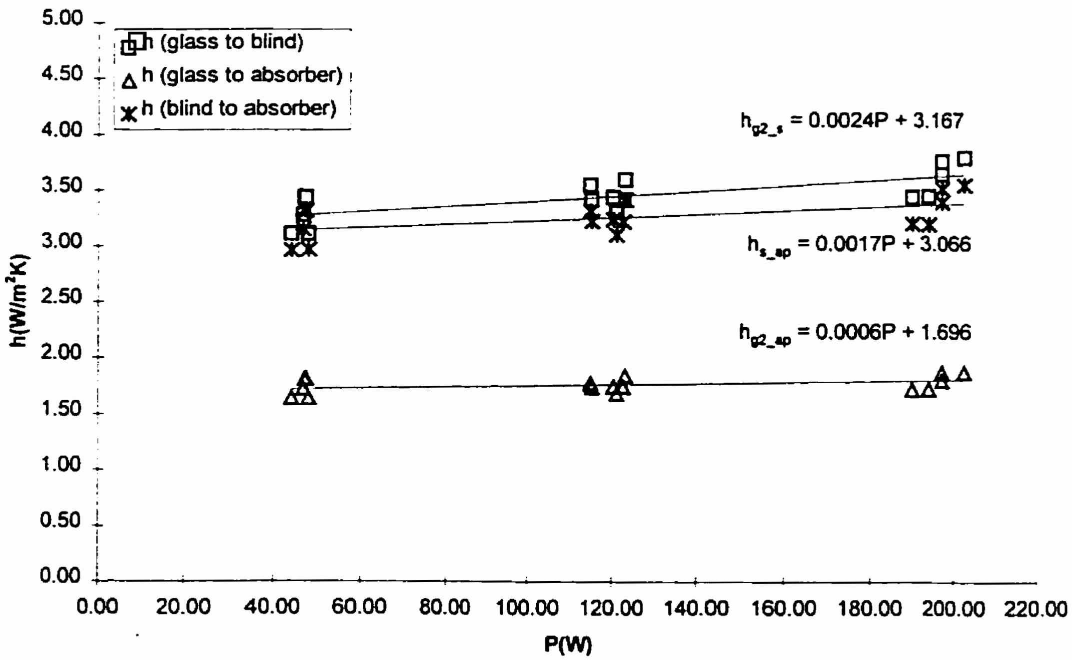

Figure 4-24. Calculated radiative heat transfer coefficients for a 0° slat angle as a function of blind power.

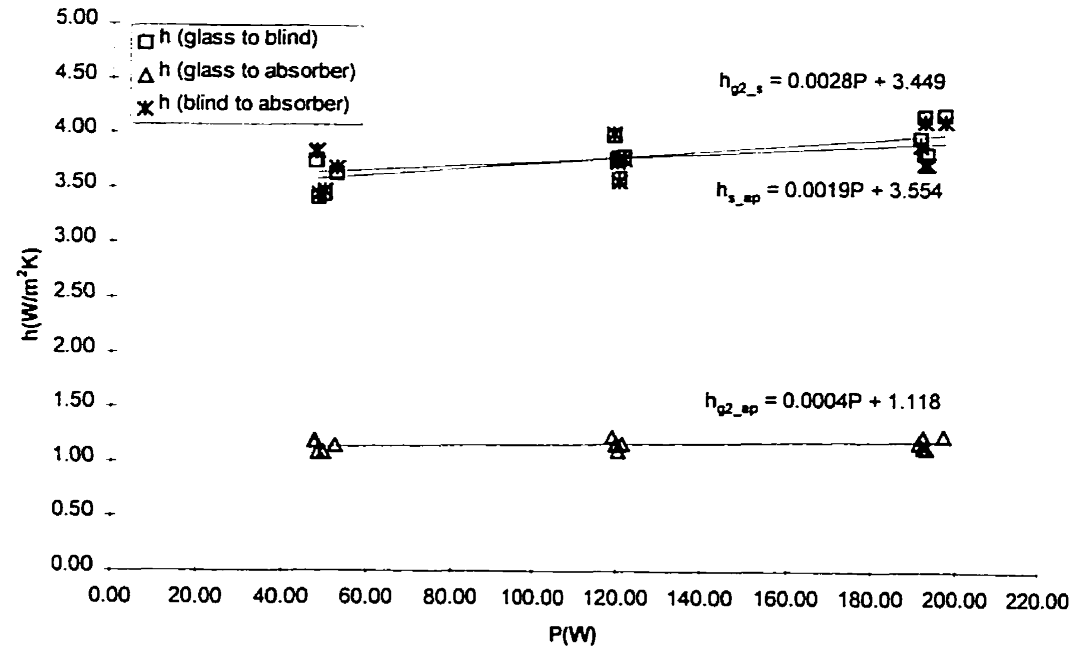

Figure 4-25. Calculated radiative heat transfer coefficients for a 45° slat angle as a function of blind power.

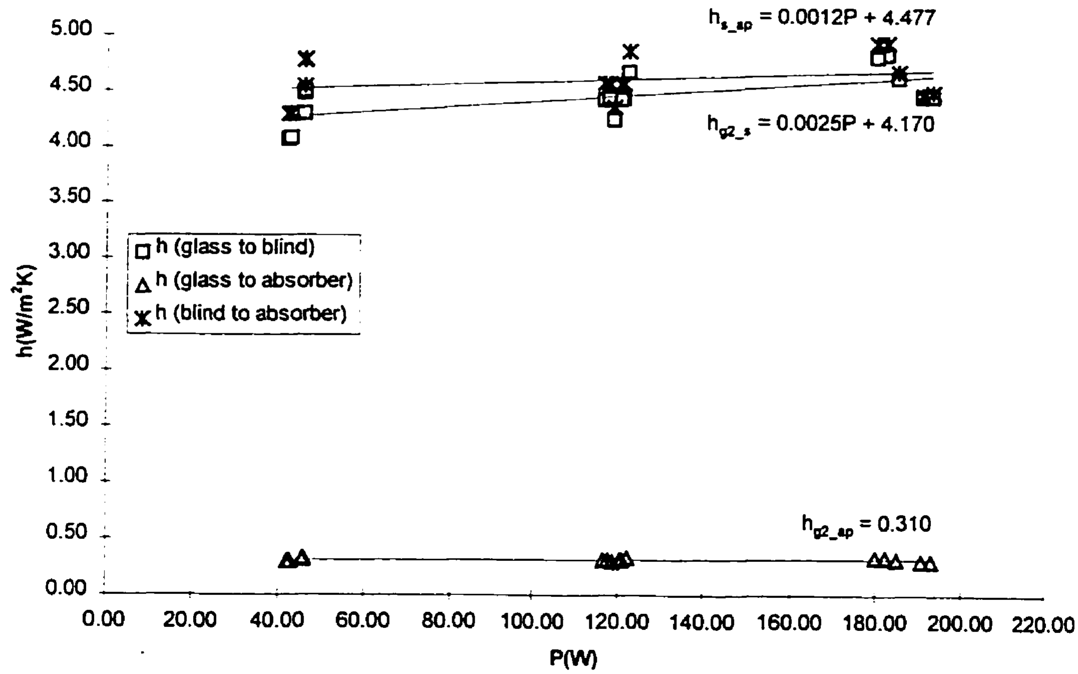

Figure 4-26. Calculated radiative heat transfer coefficients for a 70° slat angle as a function of blind power.

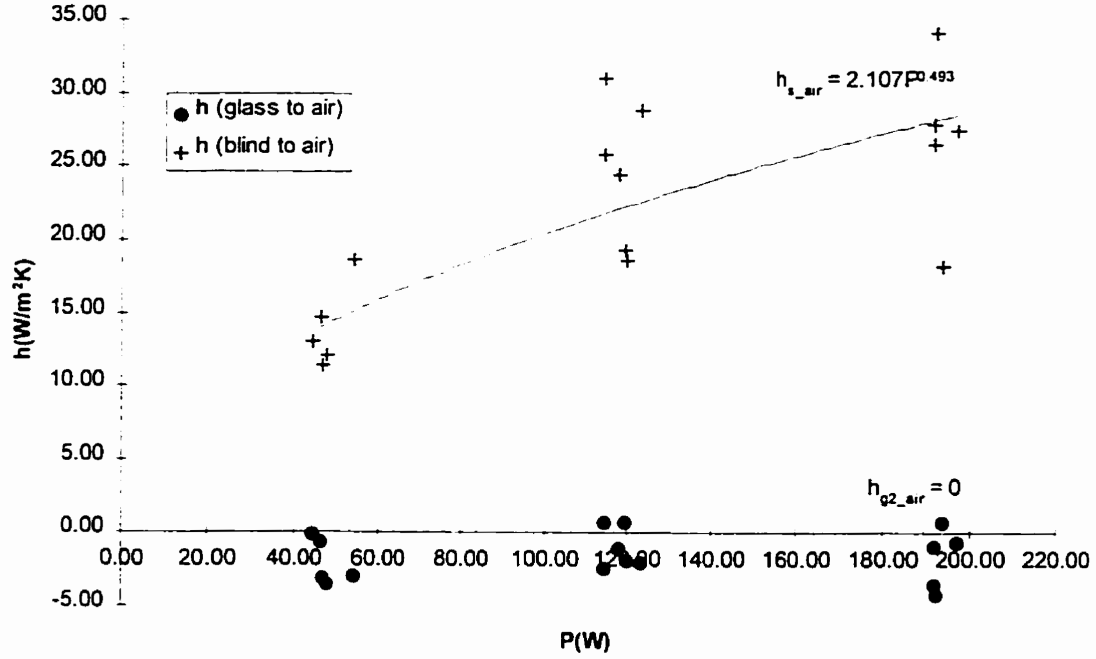

Figure 4-27. Calculated convective heat transfer coefficients for a -45° slat angle as a function of blind power.

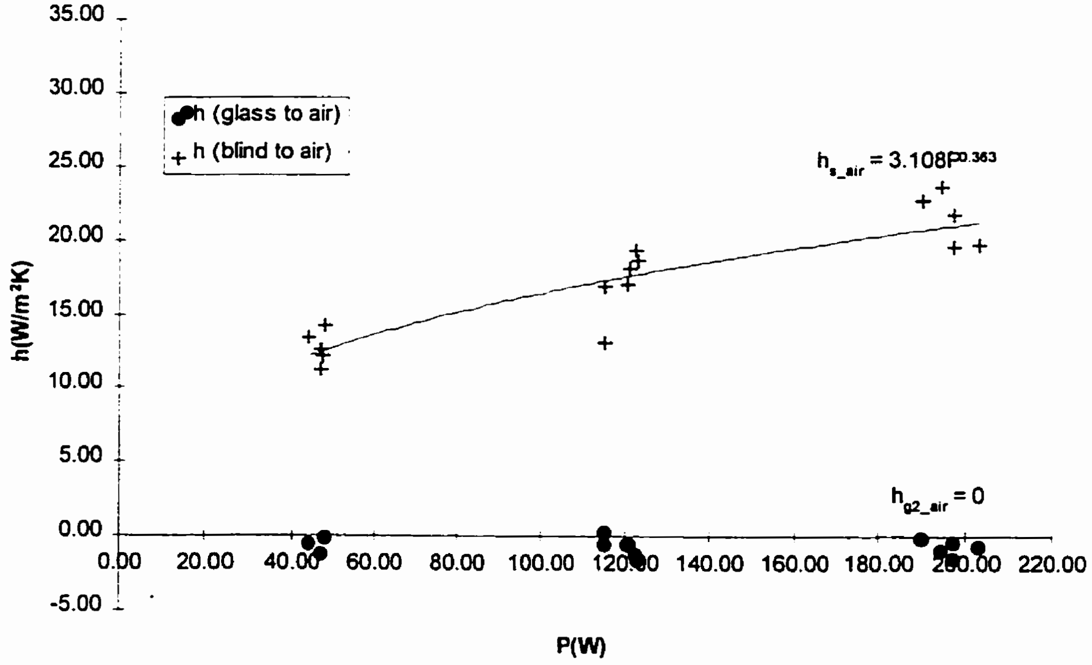

Figure 4-28. Calculated convective heat transfer coefficients for a 0° slat angle as a function of blind power.

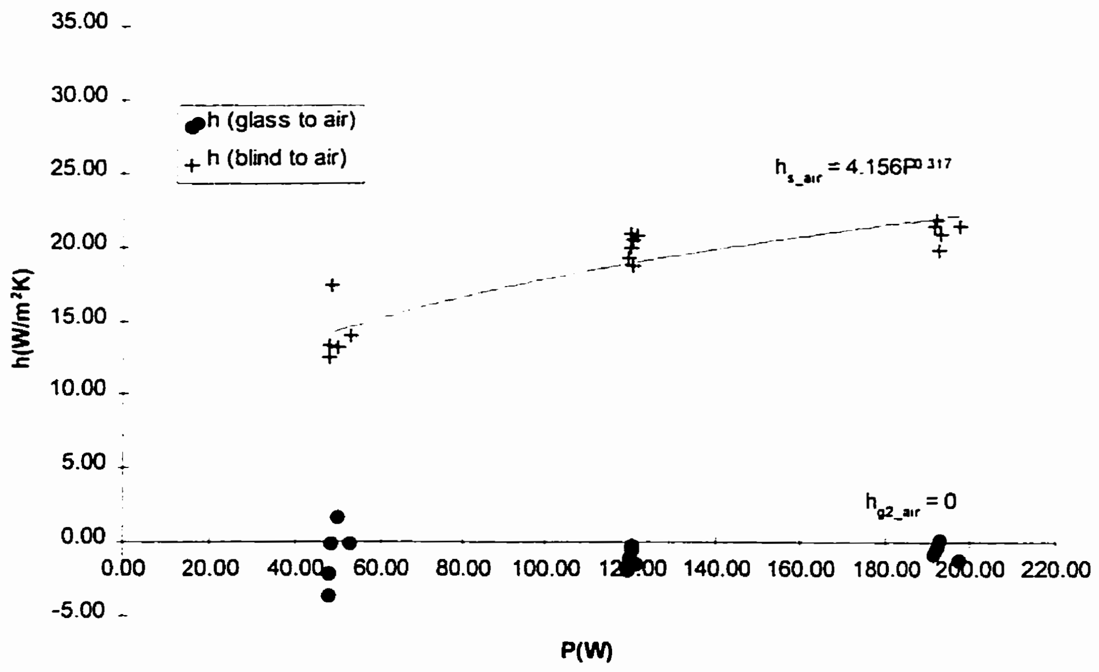

Figure 4-29. Calculated convective heat transfer coefficients for a 45° slat angle as a function of blind power.

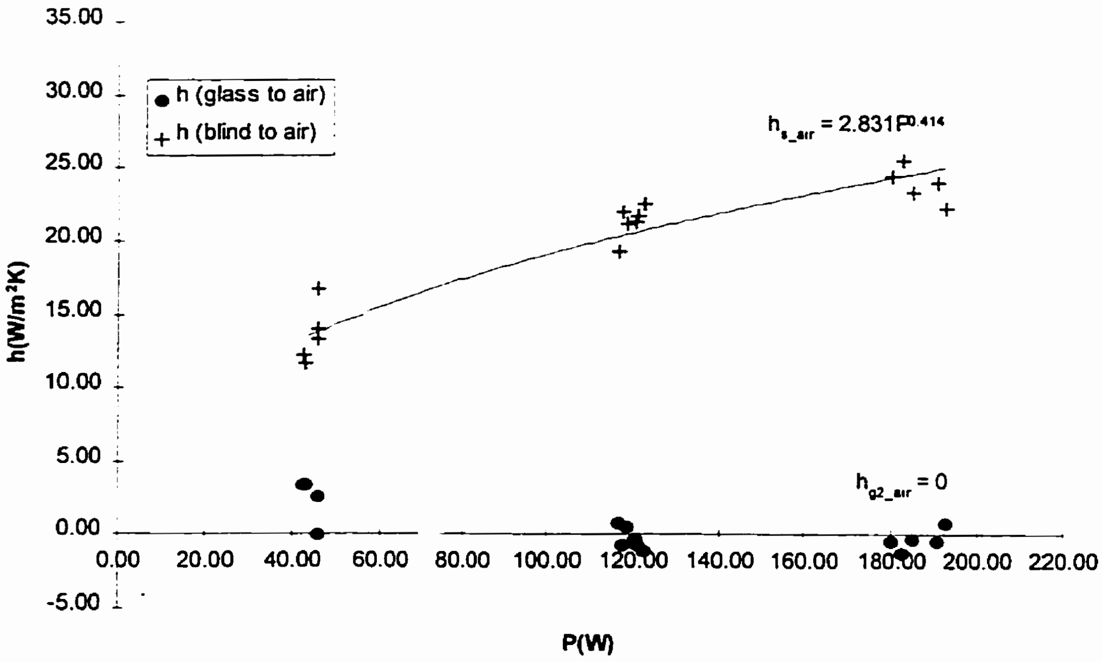

Figure 4-30. Calculated convective heat transfer coefficients for a 70° slat angle as a function of blind power.

CHAPTER 5

DISCUSSION OF RESULTS

The test results presented in Chapter 4 were examined with respect to the various test parameters. The effects of the interior / exterior temperature gradient, outdoor air film coefficient, level of irradiation, and slat angle, and their interaction, were all quantified. In addition, calculated film coefficients were used as input into the model presented by Farber et. al [8] in an effort to compare the model's success in predicting measured N_S data. The results of this analysis are contained in the following sections.

5.1 Steady-State Results

As stated in Section 3.4, a face-centered central composite factorial experiment allows the results to be correlated using linear or quadratic regression. To find a predictor equation, a quadratic fit with interactions was used. A base equation was developed that included the quadratic effects of the four dependent variables (i.e., ΔT, h_O, P, and slat angle), and the interactions between all combinations of two variables excluding the exterior air film coefficient. Also, the cosine of the slat angle was used to better represent the dependence of the natural convection heat transfer coefficient. Data was originally fit to the equation

$$
\begin{aligned}
N_s &= A + B\cdot\Delta T + C\cdot h_o + D\cdot P + E\cdot\cos(\theta) + F\cdot\Delta T^2 + G\cdot h_o^2 + H\cdot P^2 \\
&+ I\cdot\cos^2(\theta) + J\cdot\Delta T\cdot P + K\cdot\Delta T\cdot\cos(\theta) + L\cdot P\cdot\cos(\theta)
\end{aligned}
\tag{5.1}
$$

where the coefficients A-L are given in Table 5-1.

Stepwise regression then aided in determining which variables were important. That is, after every data fit, the ratio of the coefficient magnitude relative to its standard error was examined. The variable producing the lowest ratio was then removed, and the equation was refit. The results of the stepwise regression have been presented in Tables 5-1 and 5-2.

Table 5-1. Coefficients and standard error determined using stepwise regression of inward-flowing fraction data.

	Step 1	Step 2
A - Intercept	1.08533 (0.147625)	1.092671 (0.146297)
B - ΔT	-0.05279 (0.005655)	-0.05291 (0.005619)
C - h_o	-0.002233 (0.003094)	-0.00408 (0.000854)
D - P	0.002355 (0.00052)	0.002272 (0.000499)
E - $\cos(\theta)$	-0.88554 (0.399956)	-0.85295 (0.394196)
F - ΔT^2	0.001688 (0.00037)	0.001717 (0.000365)
G - h_o^2	**-5.2 x 10^{-5} (8.37 x 10^{-5})**	
H - P^2	-7.3 x 10^{-6} (1.85 x 10^{-6})	-7 x 10^{-6} (1.76 x 10^{-6})
I - $\cos^2(\theta)$	0.67915 (0.257846)	0.657512 (0.25399)
J - ΔTP	0.000105 (1.8 x 10^{-5})	0.000106 (1.79 x 10^{-5})
K - $\Delta T\cos(\theta)$	0.0133 (0.005565)	0.013086 (0.005523)
L - $P\cos(\theta)$	0.00079 (0.000379)	**-0.00079 (0.000377)**
N_s	(0.03454)	(0.034229)

Note: Standard error values are shown in brackets. Bolded entries represent the next variable removed by the stepwise regression process. Data reduced only to the lowest standard error for the entire fit.

At the second stage of the regression, the standard error of the fit reached its minimum (i.e., 0.034). The equation of best fit is therefore presented as

$$
\begin{aligned}
N_s &= A + B\cdot\Delta T + C\cdot h_o + D\cdot P + E\cdot\cos(\theta) + F\cdot\Delta T^2 + H\cdot P^2 + I\cdot\cos^2(\theta) \\
&+ J\cdot\Delta T\cdot P + K\cdot\Delta T\cdot\cos(\theta) + L\cdot P\cdot\cos(\theta)
\end{aligned}
\tag{5.2}
$$

where the coefficients are listed in Table 5-1 under the column labeled Step 2. The fit is represented graphically in Fig. 5-1. It should be noted that this fit is only valid for power inputs between 150 and 500 W/m^2, exterior film coefficients between 8 and 30 W/m^{2}K, and temperature gradients between 0 and 10 °C, where the interior is the hot side.

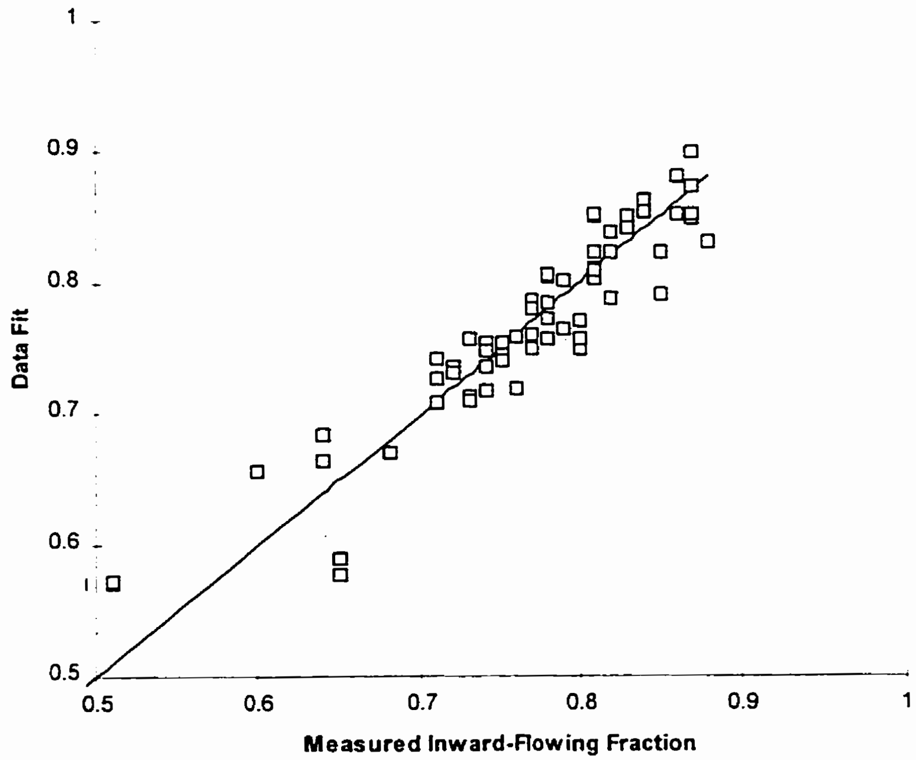

Figure 5-1. Performance of the regression fit, given as Eq. (5.2), on inward-flowing fraction results. Variable coefficients are given in Table 5-1. Dotted lines represent the standard error of the data fit.

Equation (5.2) is useful for detailed calculations when sufficient data is available for input. However, for quick estimations, a simpler form of Eq. (5.2) would be useful. We may continue to reduce the defining equation by stepwise regression. The results of this regression are found in Table 5-2.

If we consider the quality of fit at each of the stages, and the ease of obtaining a given variable, it is possible to produce a predictor equation for inward-flowing fraction. One possibility would be the equation presented by step #8 in Table 5-2. The equation is

$$N_s = A + B \cdot \Delta T + C \cdot h_o + I \cdot \cos^2(\theta) + J \cdot \Delta T \cdot P \tag{5.3}$$

where the boundaries are the same as those described for Eq. (5.2). This equation combines easily determined variables, with an accurate predictor equation. Further reductions by stepwise regression results in an increasingly poor data fit. The fit of Eq. (5.3) is represented graphically in Fig. 5-2.

Table 5-2. Coefficients and standard error determined using stepwise regression of inward-flowing fraction data.

	Step 3	Step 4	Step 5	Step 6	Step 7
A - Intercept	1.15322 (0.147743)	1.109524 (0.151767)	0.795557 (0.032)	0.869242 (0.026925)	0.87501 (0.023415)
B - ΔT	-0.05257 (0.0057880	-0.04409 (0.004549)	-0.04489 (0.004671)	-0.03993 (0.004903)	-0.0405 (0.004699)
C - h_O	-0.00403 (0.00088)	-0.00394 (0.000911)	-0.00379 (0.000936)	-0.00388 (0.001028)	-0.00382 (0.001012)
D - P	0.001778 (0.000453)	0.001727 (0.000469)	0.00173 (0.000483)	**6.27×10^{-5}** **(0.000141)**	
E - $cos(\theta)$	-0.94885 (0.403414)	**-0.88102** **(0.416861)**			
F - ΔT^2	0.001731 (0.000376)	0.001748 (0.00039)	0.001808 (0.0004)	0.001335 (0.000415)	**0.001309** **(0.000408)**
H - P^2	-7.1×10^{-6} (1.81×10^{-6})	-6.9×10^{-6} (1.88×10^{-6})	**-6.9×10^{-6}** **(1.93×10^{-6})**		
I - $cos^2(\theta)$	0.659251 (0.26173)	0.657441 (0.271212)	0.085162 (0.015793)	0.083782 (0.017348)	0.083901 (0.017225)
J - ΔTP	0.000104 (1.84×10^{-5})	0.000104 (1.9×10^{-5})	0.000106 (1.96×10^{-5})	0.000106 (2.15×10^{-5})	0.000113 (1.37×10^{-5})
K - $\Delta T cos(\theta)$	**0.012794** **(0.005689)**				
N_S	(0.035384)	(0.036666)	(0.037784)	(0.041517)	(0.041228)

Note: Standard error values are shown in brackets. Bolded entries represent the next variable removed by the stepwise regression process.

Table 5-2. continued. Coefficients and standard error determined using stepwise regression of inward-flowing fraction data.

	Step 8	Step 9	Step 10	Step 11	Step 12
A - Intercept	0.852995 (0.024083)	0.785589 (0.013724)	0.825914 (0.011057)	0.827137 (0.014341)	0.76 (0.09)
B - ΔT	-0.02702 (0.002257)	-0.02722 (0.002434)	-0.02708 (0.002746)	**-0.01314** **(0.002265)**	
C - h_O	**-0.00358** **(0.001085)**				
I - $cos^2(\theta)$	0.086455 0.018511)	**0.083774** **(0.019956)**			
J - ΔTP	0.000115 (1.47×10^{-5})	0.000118 (1.59×10^{-5})	**0.000118** **(1.79×10^{-5})**		
N_S	(0.044354)	(0.047861)	(0.053989)	(0.070034)	(0.09)

Note: Standard error values are shown in brackets. Bolded entries represent the next variable removed by the stepwise regression process.

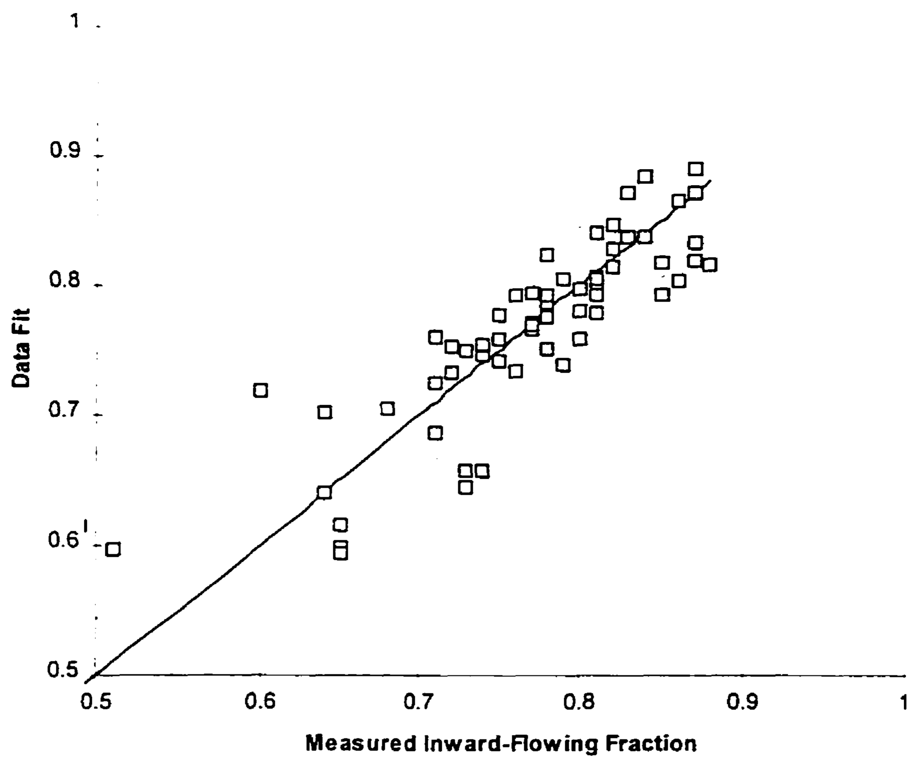

Figure 5-2. Performance of the regression fit, given as Eq. (5.3), on inward-flowing fraction results. Variable coefficients are given in Table 5-2. Dotted lines represent the standard error of the data fit.

5.1.1 Effects of Slat Angle

The inward-flowing fraction was expected to follow some predictable trends when considering blind geometry. Radiative heat flow could be described and quantified by standard heat transfer theory. At 0°, the radiation exchange from the glass to the room would be maximum and from the blind to the glass and absorber at a minimum. As the slat angle was changed (either positively or negatively), the glass-to-room component of radiation would decrease, and the blind-to-glass and blind-to-room components would increase. However, the behavior of the convective heat flow was unknown. The effects of eddies and entrained flows cannot be easily determined, making the prediction of convective flows difficult. The interaction of the radiative and convective heat flow was also unknown.

Figure 5-3 shows the relation of inward-flowing fraction tests conducted using the same test conditions, but with different slat angles. It demonstrates that generally, a decrease in radiative transmission from the blind to the glass and the blind to the absorber resulted in an increase in the inward-flowing fraction. Analysis of Figs. 4-23 to 4-30 provide an explanation for this effect. Calculated radiative heat transmission to the window was highly dependent on the slat angle. However, calculated convective heat transfer from the glass to the room was consistently small. If we consider an energy balance at the glass surface (Eq. (3.18)) we see that the heat energy leaving the window by convection ($Q_{con,g2\_air}$) is small compared to other heat flow paths. The outward-flowing fraction (and therefore the inward-flowing fraction) is then proven to be highly dependent on the level of radiative heat transfer to the glass. In addition, calculated values of N_S remain relatively constant for slat angles of -45°, 45°, and 70°. In the context of *SC* determination, there may only be a small difference between -45° or 70° slat angles.

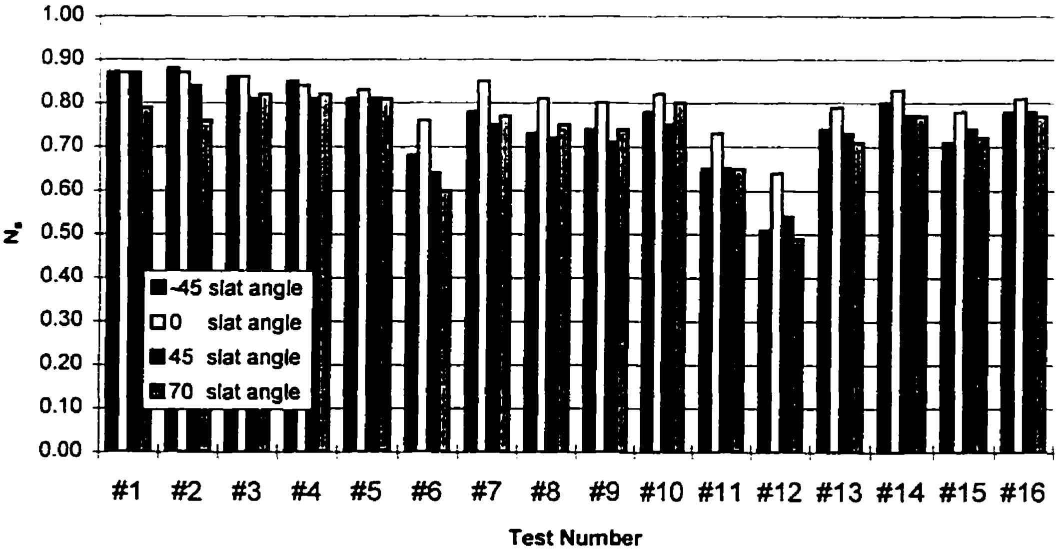

Figure 5-3. Comparison of test results for all angles. Test conditions are described in Table 3-2.

5.1.2 Absorbed Irradiation Effects

Analysis of Figs. 4-8 to 4-13 indicate two trends concerning the effect of irradiation on measured values of inward-flowing fraction. Most importantly, as irradiation level is reduced, measurement uncertainty increases. This result is a characteristic of calorimetry in general. Small amounts of energy are difficult to accurately measure. Secondly, slight upward trending occurred in measured inward-flowing fraction values between low and high power inputs.

The increase in inward-flowing fraction with power level, however, is not confirmed by parametric analysis of Eq. (5.2). Figure 5-4 shows the relative change in N_S between slat angle settings as the power level is varied. Inward-flowing fraction is stable over the entire range of power inputs.

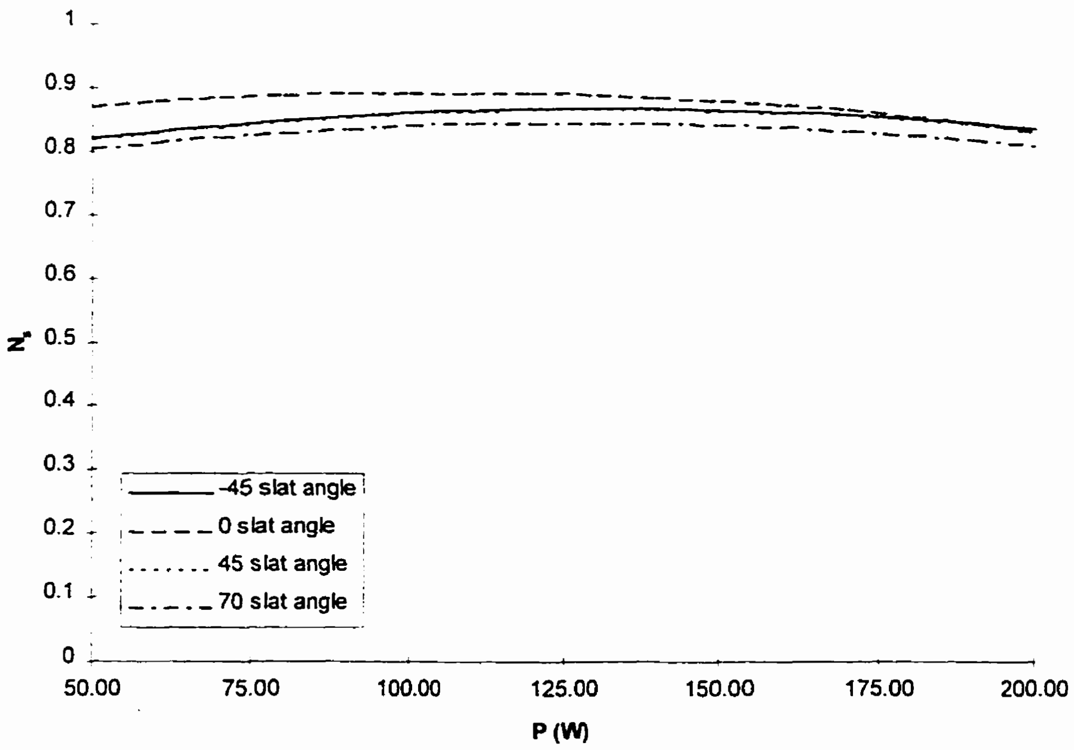

Figure 5-4. Effect of absorbed irradiation for all slat angles by parametric analysis of Eq. (5.2). $\Delta T = 0$ °C, $h_O = 20$ W/m^{2}K.

Results indicate that inward-flowing fraction tests should be performed with at least 250 W per m^2 of projected blind area, to reduce the experimental uncertainty to acceptable limits (i.e., ±0.05). Under these conditions, decreased uncertainty is insured independently from the exterior air film coefficient or the interior / exterior temperature gradient. In addition, because the irradiation level caused no strong trends in the results, values of N_S calculated at moderate power levels would be applicable to blinds irradiated at other power levels

5.1.3 Temperature Gradient Effects

At a 0 °C temperature gradient the data exhibits excellent precision. Conversely, scatter in the data at larger temperature differences is also apparent. Closer analysis shows that this scatter is primarily caused by data taken at low power input levels, and consequently, high uncertainties. Removal of these points from the data shows that the remaining points exhibit a high degree of precision.

Data collected by Klems and Kelley [10] showed no definable trend with respect to an interior / exterior temperature gradient. They stated that "there is no pronounced overall tendency for the difference $(N_s)_{PM}$ - $(N_s)_{AM}$ to be different from zero." However, their data also included changing exterior air film coefficients, irradiation levels, and dynamic effects. The results of this study indicate that it was possible that any trends in their experiment were masked by compensating factors such as the exterior film coefficient or the interior / exterior temperature gradient.

Figures 4-13 to 4-17 show definite trending in calculated inward-flowing fraction results. In all cases, N_S was reduced as the temperature gradient was increased from 0 to 10 °C. This effect is confirmed by the parametric analysis as shown in Fig. 5-5. The inward-flowing fraction is reduced by increases in the temperature gradient.

The reduction of N_S could be explained by considering the surface temperature of the window in relation to other test cell temperatures. As the interior / exterior temperature gradient increased (i.e., the test cell becomes warmer then the environment), the interior surface temperature of the window becomes cooler relative to other interior temperatures. Under these circumstances, radiative heat transfer to the window from the shade and absorber will increase, while blind-to-absorber radiation and blind-to-air convection will remain relatively constant. In addition, convective heat transfer from the window remains relatively small (as shown in Figs. 4-23 to 4-33). Therefore, energy paths which contribute to the outward-flowing fraction increase while paths contributing to the inward-flowing fraction remain constant, thereby causing a reduction in the overall inward-flowing fraction.

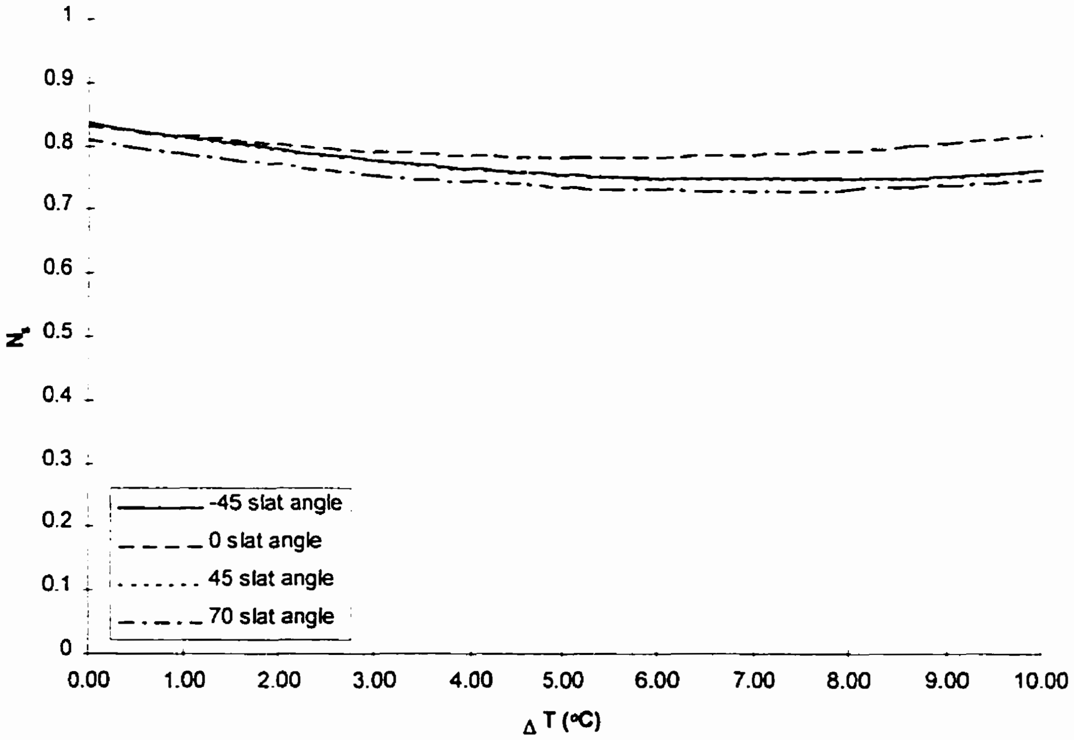

Figure 5-5. Effect of temperature gradient for all slat angles by parametric analysis of Eq. (5.2). $P = 200$ W, $h_O = 20$ W/m^{2}K.

It should be noted that a cool room relative to the environment was not investigated as a part of this study due to limitations with the test apparatus. The reversal of convective flow from the window, and large changes in the inner surface temperature of the window relative to test cell temperatures, may have a profound effect on the calculated value of N_S.

The results of this study indicate that the original assumption that N_S is independent of the interior / exterior temperature difference is not completely correct. It is therefore suggested that N_S tests be performed at a temperature consistent with natural conditions. For example, for a cooling load analysis, a worst case summer scenario should be used (i.e., based on ASHRAE design conditions [1]).

5.1.4 Exterior Air Film Coefficient Effects

The exterior air film coefficient should have a predictable effect on calculated values of N_S. An increase in h_O would result in a lower thermal resistance between the exterior glazing and the environment. In turn, this would increase the U-factor of the window and decrease the inward-flowing fraction of the blind. A lower exterior air film coefficient would have the opposite effect, and increase the inward-flowing fraction. Figures 4-18 to 4-22 show the effect of h_O on results. The magnitude of h_O in relation to the system U-factor is shown by parametric analysis of Eq. (5.2) in Fig. 5-6.

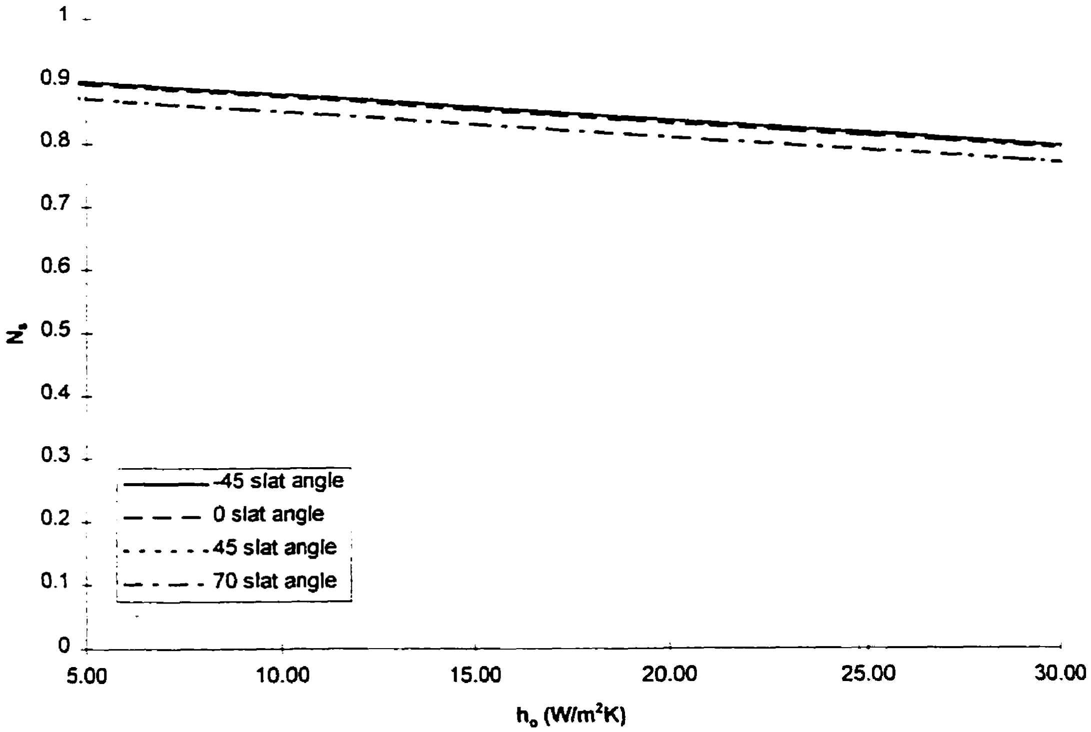

Figure 5-6. Effect of exterior air film coefficient for all slat angles by parametric analysis of Eq. (5.2). $P = 200$ W, $\Delta T = 0$ °C.

Klems and Kelley [10] have stated that the exterior air film coefficient, while not being a strong factor, must still be considered. In this regard, they also raise the question of what exterior air film would be suitable for N_S determination. While the range of air film coefficients investigated were limited, they still represent the range of conditions found in nature. The effect of this variable would suggest that ASHRAE standard design conditions (h_o = 22.7 W/m^{2}K summer and 34.0 W/m^{2}K winter) [1] would be as appropriate as any other condition.

5.2 Interior Heat Transfer Coefficient Results

Radiative heat transfer coefficients followed trends set by view factor input. As the slat angle approached 0°, glass-to-absorber heat transfer increased, and the blind-to-glass, and the blind-to-absorber heat transfer decreased. Table 5-3 shows a summary of calculated radiative heat transfer coefficients. These coefficients were determined by performing a linear regression of the radiative heat transfer coefficients from each test series.

Table 5-3. Calculated radiative heat transfer coefficients around the shading layer as a function of blind input power.

h (W/m^{2}K)	Slat Angle			
	-45°	0°	45°	70°
glass to blind	0.0020P+3.516	0.0024P+3.167	0.0028P+3.449	0.0025P+4.170
glass to absorber	0.0003P+1.134	0.0006P+1.696	0.0004P+1.118	0.310
blind to absorber	0.0012P+3.623	0.0017P+3.066	0.0019P+3.554	0.0012P+4.477

Radiative heat transfer coefficients did not vary significantly despite the fact that the glass-to-blind temperature difference did. This would suggest that the temperature term of Eq. (3.17) also remains relatively unchanged between tests conducted at the same slat angle. Figures 5-7 and 5-8 show that this is the case. While the temperature differences between the glass and the blind were widely variable, the radiative heat transfer coefficient between the glass and the blind, h_{g2_s}, changed only slightly between tests. The implications of this may be significant when considering complex fenestrations with single

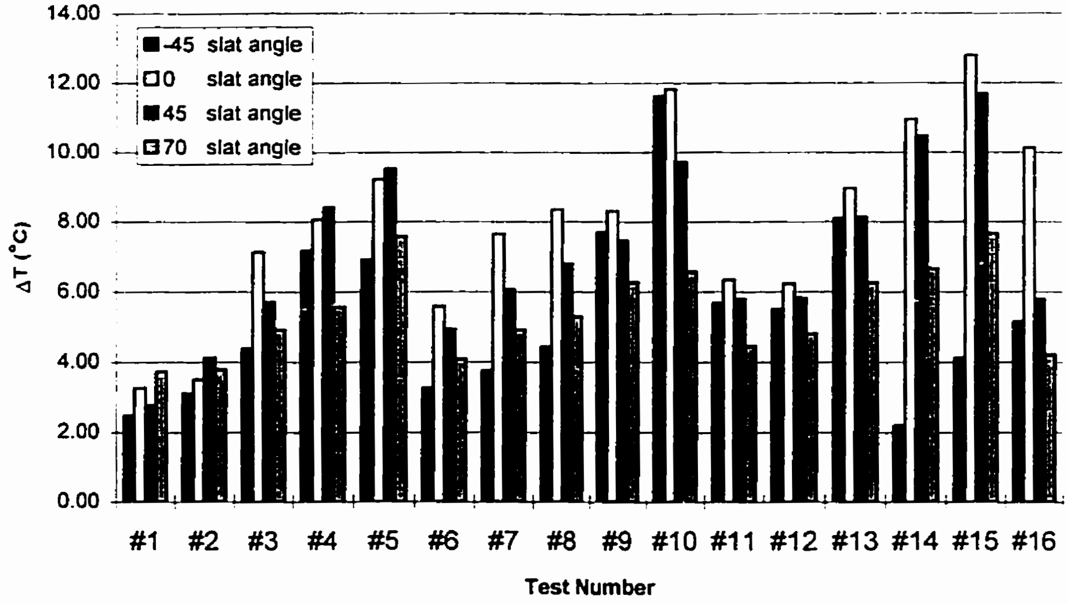

Figure 5-7. Blind to glazing temperature difference for all tests. Test conditions are presented in Table 3-2.

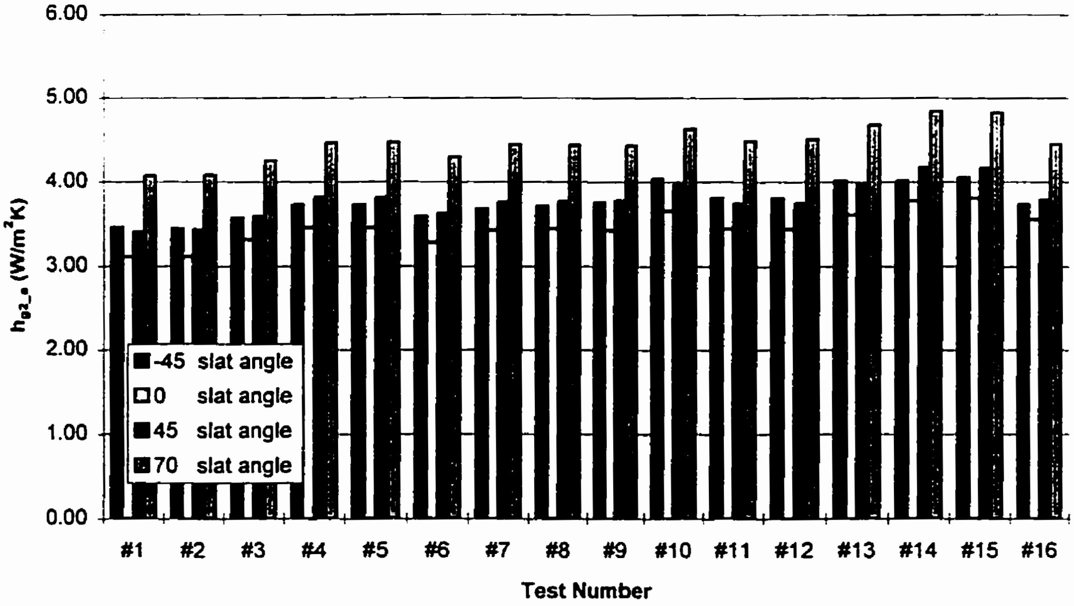

Figure 5-8. Blind to glazing radiative heat transfer coefficient for all tests. Test conditions are presented in Table 3-2.

glazings. Radiative heat transfer coefficients calculated using a double glazing may be suitable for calculating inward-flowing fraction in single glazings with venetian blinds, even though the glass-to-blind temperature difference will change significantly. The use of these heat transfer coefficients in determining inward-flowing fraction for single glazings are examined in Section 5.3.3.

As stated in Section 5.1.1, it was unknown how convective heat transfer coefficients would react to the test variables (i.e., ΔT, h_O, P, and slat angle). A summary of the convective heat transfer coefficients presented in Figs 4-27 to 4-30 is summarized in Table 5-4.

Table 5-4. Calculated convective heat transfer coefficients around the shading layer as a function of blind input power.

h (W/m²K)	Slat Angle			
	-45°	0°	45°	70°
glass to air*	0	0	0	0
blind to air	$2.107P^{0.493}$	$3.108P^{0.363}$	$4.156P^{0.317}$	$2.831P^{0.414}$
50 W	14.50	12.86	14.36	14.30
125 W	22.77	17.93	19.20	20.90
200 W	28.71	21.27	22.29	25.38

*measured convection from the glass was too small to accurately measure with the experimental apparatus

Convective heat transfer from the glass to the air remained relatively small throughout each test series. As shown in Figs. 4-27 to 4-30, calculated values of $h_{con,g2\_air}$ were approximately zero for all blind slat angles. While magnitude of this convective heat transfer coefficient is not surprising (the CTS was framed, and flow was further hampered by the proximity of the blind slats), the uncertainty in this calculation was large. Such a result suggests a problem with the test apparatus and model. For future tests, an increase in the number of temperature measurements over the blind and CTS, would provide a more precise calculation. As well, the air temperature between the glass and the blind may not be the same as the ambient temperature as the model assumes it is.

Convection from the blind acted in a much different manner than convection from the glass. As stated in Section 5.1.2, convective flow was shown to be dependent on the blind input power. As power to the blind increased, so did the convective heat transfer coefficient.

5.3 Modeling Results

5.3.1 Comparison of Previous Models

An analysis of the performance of each model is conducive to this project. Such a comparison would show similarities between predicted N_S values, and the impact of N_S on overall *SC* calculation. Appendix A contains a sample formulation using each model. The reader is referred to the original publications [8, 10, 13-16, 23-24, 28-32] for details on each method.

All models were developed using direct irradiation with no "straight through" transmittance through the shading layer. Profile and incident angles were not input into any of the models. While some did account for this, only direct normal solar incidence was used for this comparison.

Models were developed using identical layer specific optical properties (Table 5-5). Glass optical properties have been obtained from the ASHRAE HOF [1], while blind properties have been estimated. With the given materials, it was expected that a wide range of conditions could be investigated.

Table 5-5. Layer specific optical data for use in model comparison.

Layer	ρ	α	τ
Absorptive Blind	0.15	0.80	0.05
Reflective Blind	0.65	0.20	0.15
Common Glass	0.07	0.16	0.77

The apparent optical properties of each layer were determined using a simplified ray trace with limited inter-reflection, as described by Farber et. al. [8]. Figure 5-9 demonstrates this calculation.

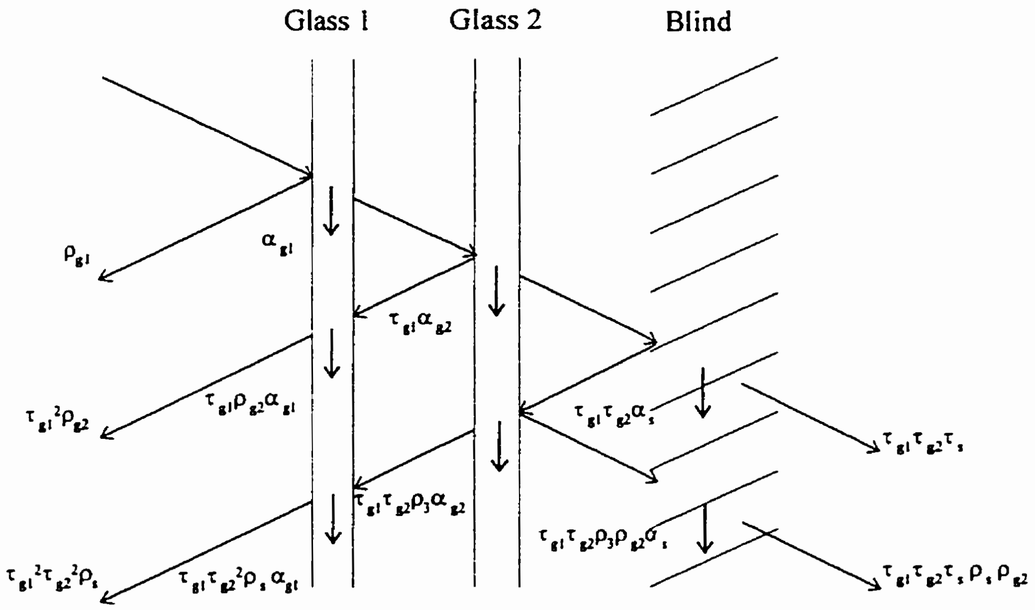

Figure 5-9. Estimated system optical performance [8].

Apparent layer specific and system properties were then determined by

$$\tau_{sys} = \tau_{g1} \cdot \tau_{g2} \cdot \tau_{s}\left(1 + \rho_{s} \cdot \rho_{g2}\right) \tag{5.4}$$

$$\rho_{sys} = \rho_{g1} + \tau_{g1}^{2}\left(\rho_{g2} + \tau_{g2}^{2} \cdot \rho_{s}\right) \tag{5.5}$$

$$\alpha_{g1'} = \alpha_{g1}\left[1 + \tau_{g1}\left(\rho_{g2} + \tau_{g2}^{2} \cdot \rho_{s}\right)\right] \tag{5.6}$$

$$\alpha_{g2'} = \alpha_{g2} \cdot \tau_{g1}\left(1 + \tau_{g2} \cdot \rho_{s}\right) \tag{5.7}$$

$$\alpha_{s'} = \alpha_{s} \cdot \tau_{g1} \cdot \tau_{g2}\left(1 + \rho_{g2} \cdot \rho_{s}\right) \tag{5.8}$$

Radiative and convective heat transfer coefficients were also used consistently through all models. However, in the case of the model by Farber et. al. [8] heat transfer coefficients were identified and used that could not easily be transferred to other models. In that case, original data was used.

The results of this comparison are presented as Table 5-6. Sample calculations of each method can be found in Appendix A.

Table 5-6. Comparison of model calculation of shading coefficient, *SC*, and inward-flowing fraction, N_S, for various fenestration and venetian blind combinations. Values in brackets represent N_S.

Window Specifications	Blind Type	Shading Coefficient (N_S)				
		Parmelee et. al. [14-16]	Farber et. al. [8], Pennington et. al. [22]	Owens [23]	Van Dyck and Konen [24]	Klems et. al. [10,13,28-32]
Single Glazing	Refl Blind	0.39 (0.95)	0.36 (0.79)	0.37 (1)	0.40 (1)	0.35 (0.83)
w/ Interior Blind	Absor Blind	0.67 (0.80)	0.69 (0.82)	0.79 (1)	0.81 (1)	0.68 (0.83)
Double Glazing	Refl Blind	NA	0.39 (0.83)	0.38 (1)	NA	0.43 (0.86)
w/ Interior Blind	Absor Blind	NA	0.64 (0.89)	0.68 (1)	NA	0.66 (0.86)
Heat Abs. / Plate	Refl Blind	NA	0.31 (0.76)	0.28 (1)	NA	0.36 (0.86)
w/ Interior Blind	Absor Blind	NA	0.45 (0.87)	0.45 (1)	NA	0.49 (0.86)

Note: NA - Not Applicable

The importance of inward-flowing fraction is clearly shown when the system has a highly absorbing inner layer. In the extreme case of a single glazings with an absorptive blind, *SC* proves to be highly dependent on N_S. Of these models, those which assume that N_S is equal to 1, predicted a much higher shading coefficient then experimental data from Klems and Kelley [10]. Comparison of experimental results from Klems and Kelley [10] with those calculated using heat transfer coefficients from Farber et. al. [8] do, however, seem to agree. These results help to confirm the validity of the model presented by Farber et. al. [8].

5.3.2 Comparison of Model with Test Results

Studies where experimental results are combined with sufficient data for model input do not exist in the literature. Key inputs such as exterior air film coefficient, system optical data, or geometric details were usually omitted from quoted results. Initial testing of the model was therefore directed towards predicting N_S as calculated using the calorimetric results obtained during this study.

Input data for the model by Farber et. al. [8] was taken from a number of sources. The optical data given in Table 5-5 was used for this analysis, and radiative and convective film coefficients were taken from Tables 5-3 and 5-4. The airspace air film coefficient was substituted with the U-factor of the calibration specimen.

The analysis was conducted within the model's ability. The model by Farber et. al. [8] was only able to calculate convective and radiative gain when no temperature gradient exists. As such, only tests 1 through 5 were modeled. Other variables were easily manipulated. The exterior air film coefficient was changed through direct input into the model. The power level was also easily represented. From the analysis, convective heat transfer from the blind to the air was shown to be directly effected by a change in power input. This coefficient was manipulated to reflect the desired level of irradiation. The results of this analysis are shown in Figs. 5-10 to 5-13.

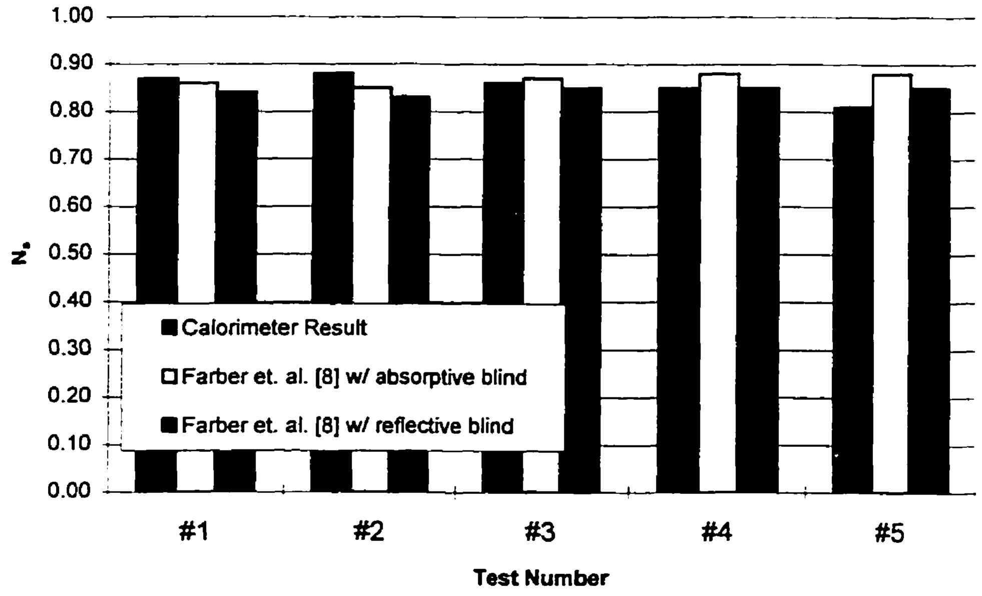

Figure 5-10. Calculated verses measured N_S values for -45° slat angle for two blinds. Model input was taken from experiment results.

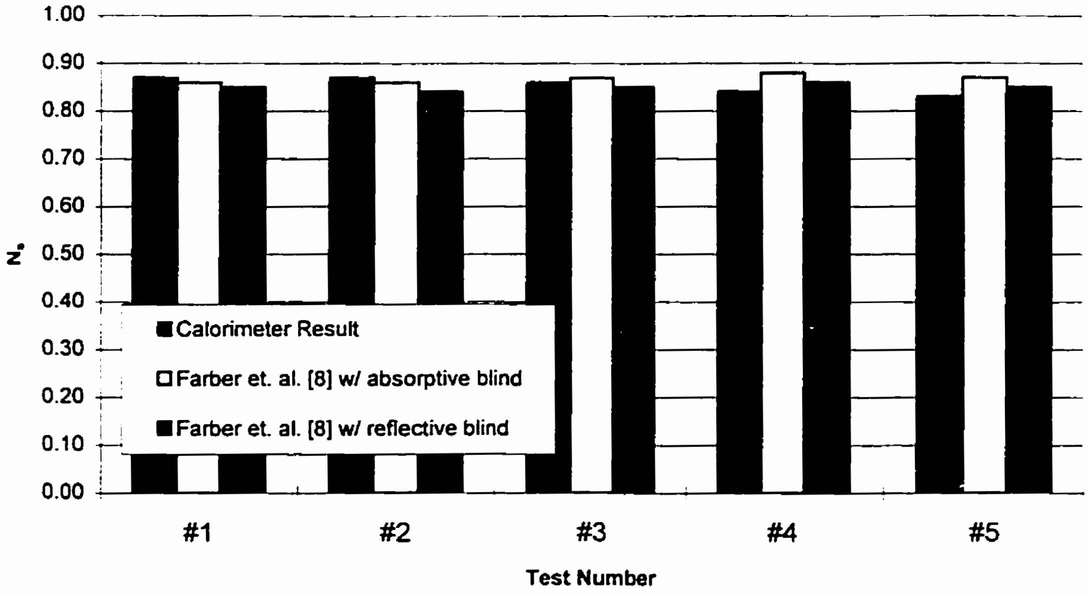

Figure 5-11. Calculated verses measured N_S values for 0° slat angle for two blinds. Model input was taken from experiment results.

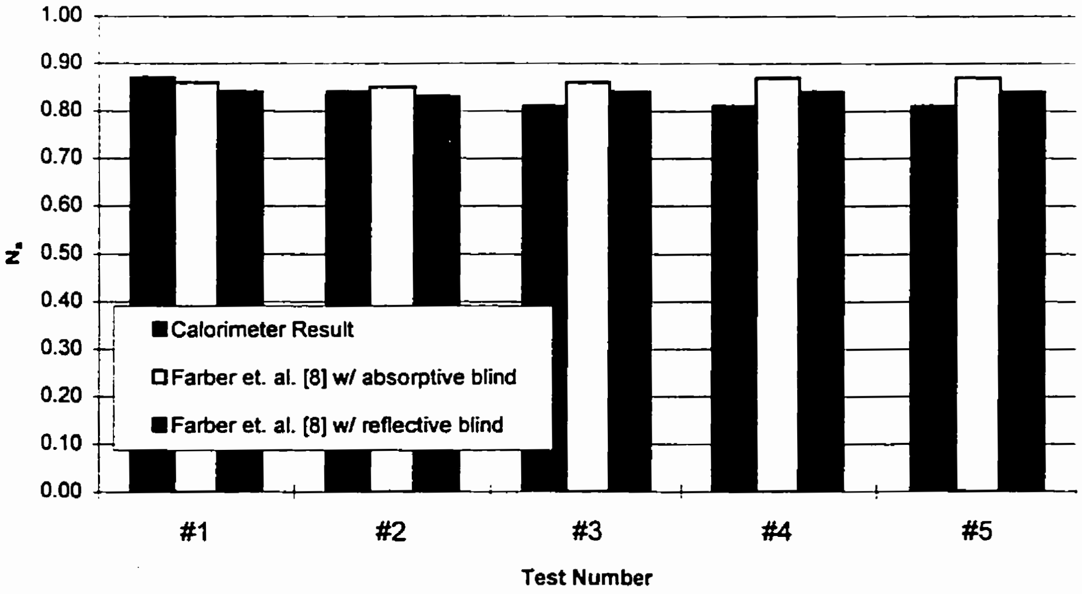

Figure 5-12. Calculated verses measured N_S values for 45° slat angle for two blinds. Model input was taken from experiment results.

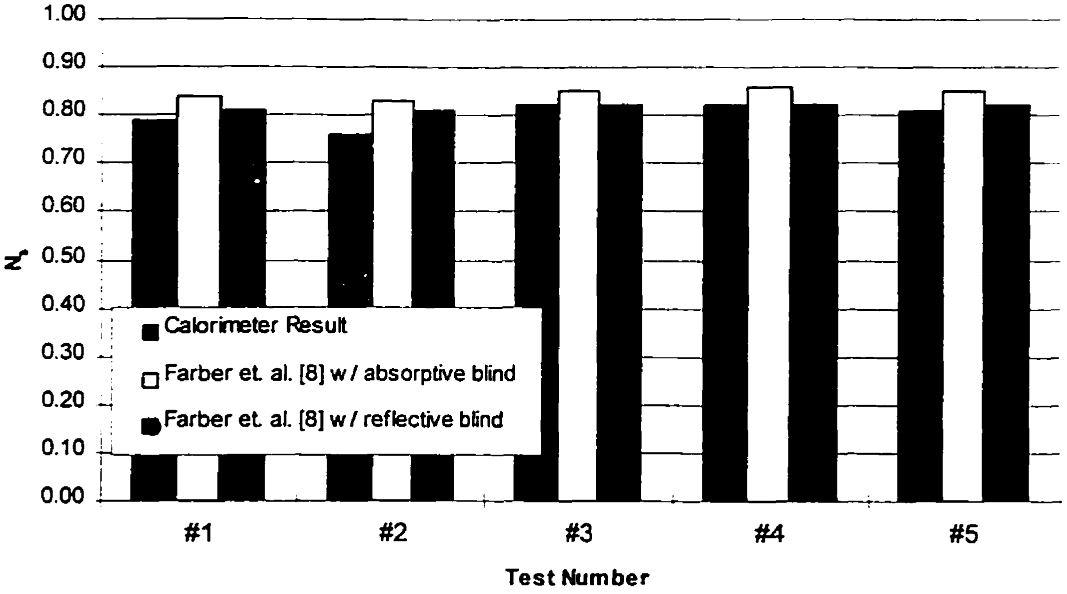

Figure 5-13. Calculated verses measured N_S values for 70° slat angle for two blinds. Model input was taken from experiment results.

The model results correlate well with measured data. If we consider only the reflective blind (which is similar to the blind used in the experiment), we see that the model was very effective in predicting the inward-flowing fraction. This is particularly true for tests 3, 4, and 5, where the calorimeter results had small uncertainties associated with them.

The model consistently predicted a higher inward-flowing fraction for an absorptive blind than for a reflective blind. However, increases were only 1% to 2% in magnitude. Such a result lends support to Klems and Kelleys [10] assumption that inward-flowing fraction is unaffected by the blinds optical properties. Further experimentation with such a blind would be required to verify predicted values.

5.3.3 Comparison of Model with Other Experimental Data

As previously noted in Section 5.3.2, comparison between experimental data and modeled systems was a difficult process. However, experimental data taken using a real window was obtained from Klems and Kelley [10] for comparative purposes. Data included any interior venetian blind regardless of slat angle, and interior shades which could be modeled as closed blinds. The current analysis covers enough angles to model his exact system with one exception: a -30° slat angle was compared to a -45° slat angle. Comparison using original data from Farber et. al. [8] was more difficult because of the few angles estimated. The results of this comparison are as shown in Table 5-7.

Table 5-7. Comparison of experimental N_S results with results from the model by Farber et. al. [8] using original and measured heat transfer coefficients.

System	Klems and Kelley [10]	Farber et. al. [8] using experimentally determined radiative and convective film coefficients	Farber et. al. [8] using original radiative and convective film coefficients
Double Glazing -45° Slat Angle	0.86 ± 0.06	0.85	0.90
Double Glazing Inside Shade[a]	0.85 ± 0.10	0.82	No Data
Single Glazing 45° Slat Angle	0.69 ± 0.05	0.80	0.86
Single Glazing -30° Slat Angle	0.83 ± 0.08	0.81[b]	0.86
Single Glazing Closed Blind	0.72 ± 0.07	0.78	No Data

[a] for comparison with closed blind

[b] estimated from -45° data

With the exception of a single glazing and blind set at a 45° slat angle, all predicted N_S values were within the margin of error quoted by Klems and Kelley [10]. If we consider double glazing and blind combinations, it can be seen that the model accurately predicts inward-flowing fraction for both of the situations analyzed. However, results for the single glazing and blind combinations were less successful. Modeled results for single glazings with blinds at 45° and closed blinds were higher then measured N_S results. The other modeled case, a single glazing and blind at -30°, while accurate, represented the modeling of a blind at -45°. The assumption presented in Section 5.2 (i.e., the increased temperature difference between the glass and the shade may not change the radiative heat transfer coefficient between those two surfaces) may not be completely correct. Further analysis of heat transfer coefficients, focusing on the glass temperature relative to other interior temperatures, may be necessary to refine this calculation.

Inward-flowing fraction results modeled using heat transfer coefficients originally presented by Farber et. al. [8] were 7% larger then those predicted using experimentally determined heat transfer coefficients. While two of these cases remain within the margin of error presented by Klems and Kelley [10], they are both less accurate then results predicted using experimentally determined heat transfer coefficients. The third case (a single glazing and blind at a 45° slat angle) was greatly over predicted when using the original data. Generally, the experimentally determined heat transfer coefficients are more accurate than those presented by Farber et. al. [8].

CHAPTER 6

CONCLUSIONS AND RECOMMENDATIONS

6.1 Conclusions

An experimental apparatus and method was developed and validated for use in determining the inward-flowing fraction of absorbed solar energy in interior venetian blinds. Inward-flowing fraction was also measured for a single blind set at various slat angles and a predictive equation was produced. Measurements taken with the apparatus were examined to provide new input data for a resistance model capable of predicting N_S. The model was an excellent predictor of inward-flowing fraction for double glazings, and only slightly less successful when applied to single glazings.

The results of this study further indicate that:

1) **the level of absorbed irradiation appears to have a minimal effect on the calculated inward-flowing fraction other than to increase measurement accuracy.** However, for modeling purposes, calculated convective heat transfer coefficients from the blind to the air did prove to be highly dependent on input power level,

2) **temperature was shown to have an influence on inward-flowing fraction.** Increases in the interior / exterior temperature difference resulted in a modest reduction in inward-flowing fraction for all tests (i.e., N_S dropped by about 0.10 between 0 and 10 °C). However, these results are limited to the range investigated in this study, i.e., $0 \leq \Delta T \leq 10$ °C. Values outside of this range need to be investigated,

3) **varying the exterior air film coefficient did not significantly effect the calculated inward-flowing fraction.** The range of naturally occurring values of h_O had only a small effect on the overall U-factor of the double glazing system studied.

In addition to the above points, a model to predict N_S was successfully identified. Comparison with experimental data showed that the resistance model for a double glazing and shade combination was an excellent predictor of inward-flowing fraction when using measured heat transfer coefficients as input. The model was only slightly less successful in predicting the inward-flowing fraction for a single glazing and blind combination.

6.2 Recommendations

An indoor calorimetric test of inward-flowing fraction is feasible. Using the method described in this report, a properly installed window and blind combination, where the blind is electrically heated, can be used to determine N_S.

The three variables examined by this experiment provided sufficient data to recommend calorimetric test conditions for the measurement of inward-flowing fraction. It is suggested that the following conditions be applied:

1) a power level of about 250 W per m^2 of blind profile area is suggested as power levels below this contribute little to the *SHG* equation,

2) testing should be conducted under realistic conditions, representative of summer and winter conditions depending on whether summer cooling or winter heating is being evaluated,

3) standard ASHRAE exterior wind speeds of 3.4 m/s (summer) and 6.7 m/s (winter) would be acceptable for testing [1].

The present analysis was primarily aimed at the development and validation of a calorimetric test method. The use of Farber et. al. [8] in modeling was a secondary goal. Considering the success of this model as a predictor, however, further development in this area would be useful. A closer investigation of heat transfer coefficients is needed. Particularly, convective heat transfer from the glass requires refinement. With this, an equipment modification is suggested. A method of controlling the temperature of the inner glazing would allow heat transfer coefficient examination for many systems. For example, cooling of the inner glazing relative to the blind would simulate a single glazing. In this way, the effect of relative blind / glazing temperatures could be determined and applied to many systems. In addition, an analysis of the air temperature between the blind and the glass may be useful. The assumption that this temperature is the same as the ambient temperature may be incorrect.

In addition, more experimental data is needed for model validation. Even though the model's effectiveness was demonstrated during this project, there was a lack of useful data in the literature to provide adequate proof of its usefulness. A full series of inward-flowing fraction tests conducted under natural conditions would provide this data and aid in exploring the versatility of the model. These tests should analyze multiple glazings, special films, and various blinds. This data will also be useful in forming an N_S database.

Analysis of tilted glazings would be useful. Many solar calorimeters currently tilt in an effort to receive direct normal solar irradiation. There is no proof that a tilted complex fenestration has the same inward-flowing fraction as a vertical system. Such an analysis would look solely at film coefficients.

A less intrusive method of heating the blind would be an asset to this analysis. The method used for this experiment made changing the slat angle difficult to accomplish. In addition, the connecting wires not only may have affected convective heat transfer by their presence, but also may have served as their own heat sources. It is recommended that large copper spacers be used to electrically connect the slats. In this way, heat generation in this area would be minimized. A large blind would have to be used to minimize the intrusive nature of the spacers and supporting structure.

REFERENCES

[1] **ASHRAE HANDBOOK - FUNDAMENTALS.** American Society of Heating, Refrigeration, and Air Conditioning Engineers, Inc., Atlanta, (1993)

[2] McCluney, R.: The Death of the Shading Coefficient?. **Passive Solar Journal, 4,** 439 (1987)

[3] Ozisik, N. and Schutrum, L. F.: Solar Heat Gain Factors for Windows With Drapes. **ASHRAE Transactions, 66,** 228 (1960)

[4] Window 4.1, A PC Program for Analyzing Window Thermal Performance. **Windows and Daylighting Group, Lawrence Berkeley Laboratory,** University of California, (1988)

[5] Wright, J.: **VISION4, Glazing System Thermal Analysis Program.** Advanced Glazing System Laboratory, University of Waterloo, Waterloo, ON, Canada, (1994)

[6] Vild, D. J.: Solar Heat Gain Factors and Shading Coefficients. **ASHRAE Journal, 10,** 47 (1964)

[7] Jordan, R. C. and Threlkeld, J. L.: Determination of the Effectiveness of Window Shading Materials on the Reduction of Solar Radiation Heat Gain. **ASHRAE Transactions, 65,** 683 (1959)

[8] Farber, E. A., Smith, W. A., Pennington, C. W., and Reed, J. C.: Theoretical Analysis of Solar Heat Gain Through Insulating Glass with Inside Shading. **ASHRAE Transactions, 69,** 392 (1963)

[9] Machin, A. D., Naylor, D., Harrison, S. J., and Oosthuizen, P. H.: An Interferometric Study of the Effect of Louvers on Free Convection from a Vertical Surface. **Presented at 4th World Conference on Experimental Heat Transfer, Fluid Dynamics, and Thermodynamics,** Brussels, (1997)

[10] Klems, J. H. and Kelley, G. O.: Calorimetric Measurements of Inward-Flowing Fraction for Complex Glazing and Shading Systems. **ASHRAE Transactions, 102,** 947 (1996)

[11] Montgomery, D. C.: **Design and Analysis of Experiments - Second Edition.** John Wiley and Sons, Inc., (1984)

[12] Mason, R. L., Gunst, R. F., and Hess, J. L.: **Statistical Design and Analysis of Experiments.** John Wiley and Sons, Inc., (1989)

[13] Klems, J. H., and Warner, J. L.: Solar Heat Gain Coefficient of Complex Fenestrations with a Venetian Blind for Differing Slat Tilt Angles. **ASHRAE Transactions**, to be published.

[14] Parmelee, G. V. and Aubele, W. W. and Vild, D. J.: The Shading of Sunlit Glass. **ASHVE Transactions, 59**, 221 (1953)

[15] Parmelee, G. V. and Aubele, W. W.: The Shading of Sunlit Glass: An Analysis of the Effect of Uniformly Spaced Flat Opaque Slats. **ASHVE Transactions, 58**, 377 (1952)

[16] Parmelee, G. V. and Vild, D. J.: Design Data for Slat Type Sun Shades for Use in Load Estimating. **ASHVE Transactions, 59**, 403 (1953)

[17] Ozisik, N. and Schutrum, L. F.: Heat Flow Through Glass With Roller Shades. **ASHRAE Transactions, 65**, 697 (1959)

[18] Yellott, J. I.: Drapery Fabrics and their Effectiveness in Solar Heat Control. **ASHRAE Transactions, 71**, 260 (1965)

[19] Moore, G. L., and Pennington, C. W.: Measurement and Application of Solar Properties of Drapery Shading Materials. **ASHRAE Transactions**, **73**, VIII.3.1, (1967)

[20] Ozisik, N. and Schutrum, L. F.: Solar Heat Gains Through Slat-Type Between Glass Shading Devices. **ASHRAE Transactions, 66**, 359 (1960)

[21] Smith, W. A. and Pennington, C. W.: Solar Heat Gain Through Double Glass with Between-Glass Shading. **ASHRAE Journal, 10**, 50 (1964)

[22] Pennington, C. W., Smith, W. A., Farber, E. A., and Reed, J. C.: Experimental Analysis of Solar Heat Gain Through Insulating Glass with Indoor Shading. **ASHRAE Journal, 2**, 27 (1964)

[23] Owens, P. G. T.: Solar Control Performance of Open and Translucent Louver Systems. **ASHRAE Transactions, 80**, 324 (1974)

[24] Van Dyck, R. L. and Konen, T. P.: Energy Conservation Through Interior Shading of Windows: An Analysis, Test and Evaluation of Reflective Venetian Blinds. **Lawrence Berkeley Laboratory**, University of California, (1982)

[25] McCluney, R.: Determining Solar Radiant Heat Gain of Fenestration Systems. **Passive Solar Journal, 4**, 4 (1987)

[26] McCluney, R. and Mills, L.: Effect of Interior Shade on Window Solar Gain. **ASHRAE Transactions, 99**, 565 (1993)

[27] Maeda, B.: Standard Procedures for the Calculation of Shading Coefficient and/or Solar Heat Gain Coefficient. Memorandum to NFRC Members, (1991)

[28] Klems, J. H. and Warner, J. L.: A New Method for Predicting the Solar Heat Gain of Complex Fenestration Systems. **Thermal Performance of the Exterior Envelope of Building Conference V**, Clearwater Beach, FL, (1992)

[29] Klems, J. H.: A New Method for Predicting the Solar Heat Gain of Complex Fenestration Systems - 1. Overview and Derivation of the Matrix Layer Calculation. **ASHRAE Transactions, 100**, 1065 (1994)

[30] Klems, J. H.: A New Method for Predicting the Solar Heat Gain of Complex Fenestration Systems - 2. Detailed Description of the Matrix Layer Calculation. **ASHRAE Transactions, 100**, 1073 (1994)

[31] Klems, J. H. and Warner, J. L.: Measurement of Bi-directional Optical Properties of Complex Shading Devices. **ASHRAE Transactions, 101**, 791 (1995)

[32] Klems, J. H., Warner, J. L. and Kelley, G. O.: A Comparison Between Calculated and Measured SHGC for Complex Glazing Systems. **ASHRAE Transactions**, to be published

[33] Harrison, S. J., Van Wonderen J. L., Wright, J. L., and McLuney, R.: Evaluation of Solar Heat Gain Test Methods. Report Prepared for ASHRAE TC 4.5, Fenestration, Research project 713. Atlanta, Ameriacan Society of Heating, Refrigeration, and Air-Conditioning Engineers (1997)

[34] Parmelee, G. V., Aubele, W. W. and Huebscher, R.G.: Measurements of Solar Heat Transfer Through Flat Glass. **ASHVE Transactions, 54**, 165 (1948)

[35] Harrison, S. J. and Dubrous, F. M.: Measurement of Solar Heat Gain Coefficient Using a Solar Simulator Test Facility. **ISES World Congress**, Denver, (1991)

[36] Dubrous, F. M. and Harrison, S. J.: Development of a Solar Simulator Based Test Method for Evaluating the Thermal Performance of Windows. **ASME International Solar Energy Conference**, San Diego, (1989)

[37] Harrison, S. J. and Dubrous, F. M.: Determination of Window Thermal Characteristics Using Solar-Simulator-Based Test Method. **ASHRAE Transactions, 96**, (1990)

[38] Van Wonderen, S. and Harrison, S. J.: Development of an Improved Calorimeter cell for Window Thermal and Solar Performance Testing. **SESCI Conference**, Edmonton, (1992)

[39] Harrison, S. J. and van Wonderen, S. J.: Determining Window Solar Heat Gain Coefficient. **ASHRAE Journal, 36**, 28 (1994)

[40] Harrison, S. J. and Dubrous, F. M.: Uncertainties in the Evaluation of Window SHGC and U-Values Measured Using an Indoor Solar Simulator Facility. **ASHRAE Meeting**, Baltimore, (1992)

[41] Rennekamp, S. J.: U-Value Testing of Windows Using a Modified Guarded Hot Box Technique. **ASHRAE Transactions, 85**, 527 (1979)

[42] Bowen, R. P.: DBR's Approach for Determining the Heat Transmission Characteristics of Windows. **Division of Building Research, National Research Council Canada**, (1985)

[43] Harrison, S. J. and Barakat, S. A.: A Method for Comparing the Thermal Performance of Windows. **ASHRAE Meeting**, Atlantic City, (1989)

[44] Interim Procedure for Determining Fenestration Product Solar Heat Gain Coefficients at Normal Incidence. **National Fenestration Rating Council**, (1992)

[45] Standard Test Method for Steady-State Thermal Performance of Building Assemblies by Means of a Guarded Hot Box. ASTM C 236-89. **Annual Book of ASTM Standards**, Vol. 04.06, (1992)

[46] The Determination of Fenestration Solar Heat Gain Coefficient Using Simulated Solar Irradiance. **CANMET**, Report by Queen's University, (1993)

[47] **CLORIUS Combimeter P-Series Instructions Manual**. AALTO, Inc., (1990)

[48] **NESLAB Constant Temperature Baths and Circulators - Instruction and Operating Manual**. Neslab Instruments, Inc., (1981)

[49] **Data Aquisition and Control System - Hardware User Guide**. Sciemetric Instruments, Inc., (1991)

[50] **QMON Manual**: Solar Calorimetry Laboratory, Queen's University at Kingston, (1993)

[51] Collins, M. R.: Queen's Solar Calorimeter – Operators Manual. Queen's University at Kingston, (1996)

[52] Kline, S. J., and McClintock, F. A.: Describing Uncertainties in Single-Sample Experiments. **Mechanical Engineering**, (1953)

[53] Rohm and Haas Web Page: http://www.rohmhaas.com/, (1997)

[54] **RADCAD™ Users Manual.**: Cullimore and Ring Technologies, Inc., (1997)

[55] Harrison, S. J., and Van Wonderen, S. J.: Solar Heat Gain Performance Evaluation of Commercial Solar-Control Glazings and Shading Devices. **Buildings Group, CANMET**, (1996)

[56] **The Temperature Handbook**. OMEGA Engineering, Inc., (1992)

[57] Holman, J. P.: **Heat Transfer. Seventh Edition**. McGraw-Hill Inc., (1990)

[58] **Steady-State Heat Transfer Analysis - Interactive Self Demonstration and Introduction**. ALGOR, Inc., (1992)

[59] Mitalas, G. P., and Stephenson, D. G.: FORTRAN IV Programs to Calculate Radiant Energy Interchange Factors. **Division of Building Research, National Research Council Canada,** (1966)

[60] Holman, J. P.: **Experimental Methods for Engineers. Fifth Edition.** McGraw-Hill, New York, (1989)

[61] **Digital Multimeter 3468A - Service Manual**. Hewlet Packard (1981)

APPENDIX A
EMPIRICAL MODEL DEVELOPMENT

The models discussed in Chapter 2 can be found in references [8, 10, 13-32]. However, because of the importance of the model by Farber et. al. [8], it would be prudent to discuss it in more detail. Section A.1 is an excerpt from Appendix B of that reference. The text has been modified to reflect changes in figure and equation numbers, and units only. A formal description of the nomenclature can be found in reference [8]. Non-essential data has been omitted.

The determination of radiative view factors is also important to the analysis. Results of view factor determination using RADCAD™ [54] can be found in Section A.2.

A sample from each model [8, 10, 13-32] is provided in Section A.3.

A.1 Determination of Convection and Radiation Heat Gain from Double Glass and Venetian Blind Fenestrations [8]

The following heat balance equations are derived for the schematic of Fig. A-1.

$$Q_0 = h_0(T_{g1} - T_0) \tag{A.1}$$

$$Q_1 = h_1(T_{g1} - T_{g2}) \tag{A.2}$$

$$Q_2 = h_2(T_{g2} - T_{A1}) \tag{A.3}$$

$$Q_3 = h_3(T_{g2} - T_s) \tag{A.4}$$

$$Q_4 = h_4(T_{g2} - T_i) \tag{A.5}$$

$$Q_5 = h_5(T_s - T_i) \tag{A.6}$$

$$Q_6 = h_6(T_s - \frac{T_{A1} + T_{A2}}{2}) \tag{A.7}$$

$$CR + Q_0 = I(\alpha'_{g1} + \alpha'_{g2} + \alpha'_s) \tag{A.8}$$

$$Q_2 = wC_p(T_{A1} - T_i) \tag{A.9}$$

$$Q_2 + Q_6 = wC_p(T_{A2} - T_i) \tag{A.10}$$

$$Q_0 + Q_1 = I \cdot \alpha'_{g1} \tag{A.11}$$

$$Q_2 + Q_3 + Q_4 = I \cdot \alpha'_{g2} + Q_1 \tag{A.12}$$

$$Q_5 + Q_6 = I \cdot \alpha'_s + Q_3 \tag{A.13}$$

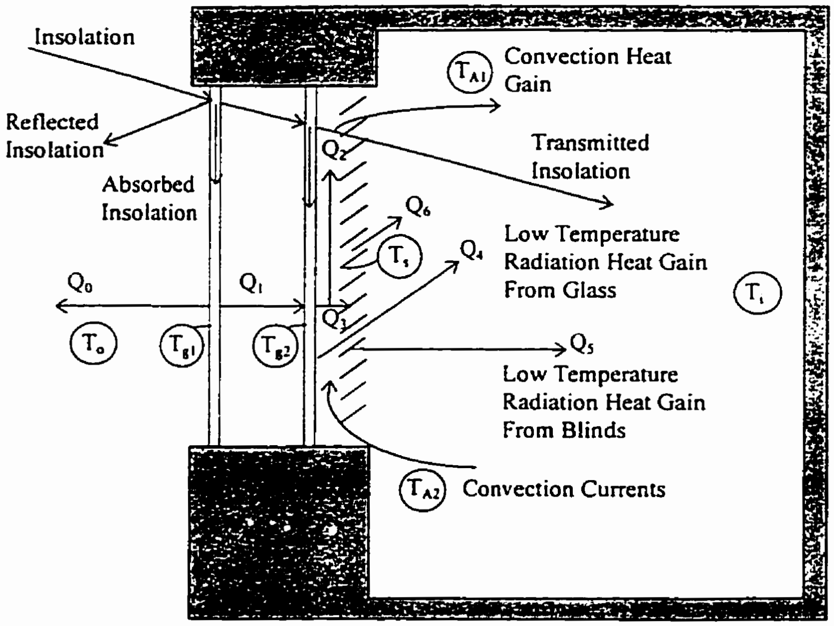

Figure A-1. Heat Transfer Phenomenon for the Convection and Low Temperature Radiation Components of the Total Heat Gain Through a Double Glass and Venetian Blind Fenestration [8].

An assumption is made in Eq. (A.7) that the log mean temperature difference may be simplified to the form shown in Eq. (A.7), in order to avoid logarithmic terms in the algebraic manipulations following. Assuming that all the Q terms, and all the temperature terms except T_S and T_i, are unknown, it is seen that there are sufficient independent equations in the above that these unknowns can be algebraically eliminated to yield an expression for convective and radiative gain (*CR*) as given in Eq. (A.7). However, by simple substitution for the Q terms, Eqs. (A.1) to (A.13) can be reduced to the following

$$h_0 \cdot T_{g1} + CR = h_0 \cdot T_0 + I(\alpha'_{g1} + \alpha'_{g2} + \alpha'_s) \tag{A.14}$$

$$h_2 \cdot T_{g2} - (wC_p + h_2)T_{A1} = -wC_p \cdot T_i \tag{A.15}$$

$$-h_1 \cdot T_{g1} + (h_1 + h_2 + h_3 + h_4)T_{g2} - h_2 \cdot T_{A1} - h_3 \cdot T_s = h_4 \cdot T_i + I \cdot \alpha'_{g2} \tag{A.16}$$

$$(h_0 + h_1)T_{g1} - h_1 \cdot T_{g2} = I \cdot \alpha'_{g1} + h_0 \cdot T_0 \tag{A.17}$$

$$-h_3 \cdot T_{g2} - \frac{h_6 \cdot T_{A1}}{2} - \frac{h_6 \cdot T_{A2}}{2} + (h_3 + h_5 + h_6)T_s = h_5 \cdot T_i + I \cdot \alpha'_s \tag{A.18}$$

$$(wC_p - \frac{h_6}{2})T_{A1} - (wC_p + \frac{h_6}{2})T_{A2} + h_6 \cdot T_s = 0 \tag{A.19}$$

where the unknowns are now T_{g1}, T_{g2}, T_{A1}, T_{A2}, T_S and CR. Further reduction of these equations was considered unnecessary and too complex, since the six equations with their six unknowns could be more easily set up in their determinant form on a PC, where the simultaneous solution for CR would be both rapid and accurate. $C_{p,solar}$ was calculated by setting $I = 1.0$ and $T_o = T_i = 1.0$.

Absorptances of the individual barriers were calculated from the data of the graphs and tables in this paper and in the references and from Eqs. (A.4) to (A.6). Calculation of the heat transfer coefficients for convection and radiation was done from the following familiar equations

$$h_{con} = \frac{C \cdot K}{L}\left(\frac{g \cdot \beta \cdot C_p \cdot \rho^2}{\mu \cdot K} L^3 \cdot \Delta T\right)^d \tag{A.20}$$

$$h_{rad} = \frac{\sigma \cdot F_E \cdot F_A (T_1^4 - T_2^4)}{(T_1 - T_2)} \tag{A.21}$$

The assumptions made in the solution of these equations are

1: h_o =22.7 W/m^{2}K: this is at the request of ASHRAE TAC 2.5.

2: $F_E \cdot F_A$ is as follows:

	deg 0	deg 30	deg 45
h_1	0.82	0.82	0.82
h_3	0.55	0.58	0.62
h_4	0.33	0.30	0.24
h_5	0.48	0.53	0.57

The values of $F_E \cdot F_A$ were estimated for different slat angles by the use of Tables A-1 to A-8 of Reference [12], derived to establish the diffuse radiation transmittance through a slat assembly as a function of slat angle and fraction of slat width irradiated.

3: $w = \rho A V$

A is considered one quarter the area of the glass;

V is considered 0.037 m/s for natural convection;

ρ is P/RT = 1.181 kg/m^3

4: The inside of the room is a blackbody at 27 °C.

5: The shortness factor used in determining convection from the venetian blind is

$$L = \frac{L_H \cdot L_V}{\left(L_H + L_V\right)} \tag{A.22}$$

A.2 RADCAD™ Radiation Shape Factor Results

RADCAD™ [54] was used to calculate radiative shape factors used as model input. The entire calorimeter cell was modeled using this software. In the following pages, each surface is referred to as MAIN. MAIN.1 represents the glass, MAIN.2 represents the shade, and MAIN.3 represents the absorber panel.

0° Shade Angle

Surface to Surface A_1F_{12}

```
-1,      MAIN.3,      SPACE.1,    7.7343
-2,      MAIN.2,      MAIN.3,     0.51828
-3,      MAIN.2,      MAIN.4,     0.36080
-4,      MAIN.2,      MAIN.1,     0.60477
-5,      MAIN.3,      MAIN.4,     0.16961
-6,      MAIN.3,      MAIN.1,     0.29850
-7,      MAIN.4,      MAIN.1,     0.10224
C
C        MAIN.2   to self,     1.1657
C        MAIN.3   to self,     11.943
C        MAIN.4   to self,    0.044540
C
C        MAIN.3 to inactive surfaces,     0.36330
C
C Summary data
C             node    area     rays    sum      emiss    %kept
C
C          MAIN.2 2.6560   10000  2.6496   1.0000  99.758
C          MAIN.3 21.000   10000  20.663   1.0000  98.397
C          MAIN.4 0.68000  10000  0.67719  1.0000  99.586
C          MAIN.1 1.0000   10000  1.0055   1.0000  100.55
```

45° (-45°) shade angle

Surface to Surface A_1F_{12}

```
-1,      MAIN.3,       SPACE.1,    7.6608
-2,      MAIN.2,        MAIN.3,    0.61957
-3,      MAIN.2,        MAIN.4,    0.27986
-4,      MAIN.2,        MAIN.1,    0.68293
-5,      MAIN.3,        MAIN.4,    0.20081
-6,      MAIN.3,        MAIN.1,    0.18593
-7,      MAIN.4,        MAIN.1,    0.12917
C
C        MAIN.2   to self,     0.84907
C        MAIN.3   to self,      11.932
C        MAIN.4   to self,    0.067864
C
C        MAIN.3 to inactive surfaces,      0.40320
C
C Summary data
C            node      area     rays     sum      emiss    %kept
C
C          MAIN.2  2.4183    10000   2.4314   1.0000   100.54
C          MAIN.3  21.000    10000   20.599   1.0000   98.092
C          MAIN.4 0.68000    10000  0.67771   1.0000   99.663
C          MAIN.1  1.0000    10000  0.99803   1.0000   99.803
```

70° shade angle

Surface to Surface A_1F_{12}

```
-1,      MAIN.3,       SPACE.1,    7.6797
-2,      MAIN.2,        MAIN.3,    0.76656
-3,      MAIN.2,        MAIN.4,    0.27037
-4,      MAIN.2,        MAIN.1,    0.82564
-5,      MAIN.3,        MAIN.4,    0.19939
-6,      MAIN.3,        MAIN.1,    0.047943
-7,      MAIN.4,        MAIN.1,    0.12677
C
C        MAIN.2   to self,     0.63476
C        MAIN.3   to self,      11.886
C        MAIN.4   to self,    0.083436
C
C        MAIN.3 to inactive surfaces,      0.35700
C
C Summary data
C            node      area     rays     sum      emiss    %kept
C
C          MAIN.2  2.4893    10000   2.4973   1.0000   100.32
C          MAIN.3  21.000    10000   20.580   1.0000   97.998
C          MAIN.4 0.68000    10000  0.67996   1.0000   99.994
C          MAIN.1  1.0000    10000  1.00003   1.0000   100.03
```

A.3 Sample Model Calculations

Representing the calculation procedure for each model would be an extensive undertaking. Instead, sample calculation sheets have been provided. If information is required about a specific model, it is suggested that the original publications be consulted.

Models were developed using identical layer specific optical properties. System optical data was determined using a ray trace with limited inter-reflection which was borrowed from Farber et. al. [8].

Where possible, film coefficients have been used consistently through all models. However, in the case of Farber et. al. [8], film coefficients were identified and used that could not easily be transferred to other models. In this case, original data was used.

All models were developed using direct solar irradiation with no straight through transmittance through the shading layer. Profile and incident angles were not input into any of the models.

A.3.1 Double Glazing Models

Farber et. al. [8]

Material Properties	
τ_{g1}	0.770
τ_{g2}	0.770
τ_s	0.150
α_{g1}	0.160
α_{g2}	0.160
α_s	0.200
ρ_{g1}	0.070
ρ_{g2}	0.070
ρ_s	0.650
α'_{g1}	0.216
α'_{g2}	0.185
α'_s	0.124
τ_{gs}	0.093
ρ_{gs}	0.340
α_{gs}	0.567

Input Data	
h_0	4.00
h_1	1.50
h_2	0.57
h_3	0.79
h_4	0.36
h_5	1.51
h_6	1.80
w_{cp}	1.90
T_i	1.00
T_o	1.00
I	1.00
U	0.64

Matrix Formulation

$$\begin{vmatrix} 4.00 & 0.00 & 0.00 & 0.00 & 0.00 & 1.00 \\ 0.00 & 0.57 & -2.47 & 0.00 & 0.00 & 0.00 \\ -1.50 & 3.22 & -0.57 & 0.00 & -0.79 & 0.00 \\ 5.50 & -1.50 & 0.00 & 0.00 & 0.00 & 0.00 \\ 0.00 & -0.79 & -0.90 & -0.90 & 4.10 & 0.00 \\ 0.00 & 0.00 & 1.00 & -2.80 & 1.80 & 0.00 \end{vmatrix} \begin{vmatrix} T_{g1} \\ T_{g2} \\ T_{A1} \\ T_{A2} \\ T_s \\ CR \end{vmatrix} \begin{matrix} 4.5249 \\ -1.9000 \\ 0.5449 \\ 4.2161 \\ 1.6340 \\ 0.0000 \end{matrix}\Bigg|$$

$$\begin{vmatrix} 0.0000 & -0.0382 & 0.1118 & 0.2123 & 0.0251 & -0.0081 \\ 0.0000 & -0.1401 & 0.4100 & 0.1118 & 0.0920 & -0.0296 \\ 0.0000 & -0.4372 & 0.0946 & 0.0258 & 0.0212 & -0.0068 \\ 0.0000 & -0.2738 & 0.1140 & 0.0311 & 0.2081 & -0.4240 \\ 0.0000 & -0.1831 & 0.1248 & 0.0340 & 0.3120 & -0.1003 \\ 1.0000 & 0.1528 & -0.4473 & -0.8493 & -0.1003 & 0.0323 \end{vmatrix} \begin{matrix} 4.5249 \\ -1.9000 \\ 0.5449 \\ 4.2161 \\ 1.6340 \\ 0.0000 \end{matrix}\Bigg|$$

T_{g1}	1.07
T_{g2}	1.11
T_{A1}	1.03
T_{A2}	1.05
T_s	1.07
CR	0.25
N_i	0.43

Results	
SC	0.39
F	0.34
$N\alpha_{sys}$	0.25
$N\alpha_{g1}$	0.03
$N\alpha_{g2}$	0.11
N_s	0.83

Owens [23]

Material Properties

τ_{g1}	0.770
τ_{g2}	0.770
τ_s	0.150
α_{g1}	0.160
α_{g2}	0.160
α_s	0.200
ρ_{g1}	0.070
ρ_{g2}	0.070
ρ_s	0.650
SCSW	0.11
SCLW	0.27
SC	0.38

Input Data

h_i	8.90
h	8.60
h_e	22.72
U	2.60

Optical Properties

$$\begin{vmatrix} 0.111 & -0.054 \\ 0.770 & -0.955 \end{vmatrix} \quad \begin{vmatrix} 0.054 \\ 0.000 \end{vmatrix}$$

$$\begin{vmatrix} 14.776 & -0.834 \\ 11.920 & -1.721 \end{vmatrix} \quad \begin{vmatrix} 0.054 \\ 0.000 \end{vmatrix}$$

$\Phi 0$	1.000	$\Psi 0$	0.361		
$\Phi 1$	0.796	$\Psi 1$	0.377	A'1	0.220
$\Phi 2$	0.642	$\Psi 2$	0.418	A'2	0.194
$\Phi 3$	0.096			A'3	0.128

Matrix Formulation

$$\begin{vmatrix} 31.32 & -8.60 & 0.00 \\ -8.60 & 17.50 & -8.90 \\ 0.00 & -8.90 & 17.80 \end{vmatrix} \quad \begin{vmatrix} 0.2204 \\ 0.1942 \\ 0.1285 \end{vmatrix}$$

$$\begin{vmatrix} 0.0390 & 0.0257 & 0.0128 \\ 0.0257 & 0.0936 & 0.0468 \\ 0.0128 & 0.0468 & 0.0796 \end{vmatrix} \quad \begin{vmatrix} 0.2204 \\ 0.1942 \\ 0.1285 \end{vmatrix} \qquad \begin{vmatrix} 0.0152 \\ 0.0298 \\ 0.0221 \end{vmatrix}$$

Results

SC	0.38
F	0.33
$N\alpha_{sys}$	0.23
$N\alpha_{g1}$	0.03
$N\alpha_{g2}$	0.08
N_s	1.00

Klems et. al. [10,13,28-32]

Material Properties	
τ_{g1}	0.770
τ_{g2}	0.770
τ_{s}	0.150
α_{g1}	0.160
α_{g2}	0.160
α_{s}	0.200
ρ_{g1}	0.070
ρ_{g2}	0.070
ρ_{s}	0.650
α'_{g1}	0.216
α'_{g2}	0.185
α'_{s}	0.124
τ_{gs}	0.093
ρ_{gs}	0.340
α_{gs}	0.567

Results	
SC	0.43
F	0.37
$N\alpha_{sys}$	0.28
$N\alpha_{g1}$	0.05
$N\alpha_{g2}$	0.13
N_{s}	0.86

A.3.2 Single Glazings

Parmelee [14-16]

Material Properties

τ_{gl}	0.770
τ_s	0.150
α_{gl}	0.160
α_s	0.200
ρ_{gl}	0.070
ρ_s	0.650
α'_{gl}	0.240
α'_s	0.161
τ_{gs}	0.121

Input Data

h_0	4.00
h_2	0.57
h_3	0.79
h_4	0.36
h_5	1.51
h_6	1.80
h_i	1.36
U	1.13

Results

SC	0.39
F	0.34
$N\alpha_{sys}$	0.22
$N\alpha_{gl}$	0.07
$N\alpha_s$	0.15
N_s	0.95

Farber et. al. [8]

Material Properties

τ_{g1}	1.000
τ_{g2}	0.770
τ_s	0.150
α_{g1}	0.000
α_{g2}	0.160
α_s	0.200
ρ_{g1}	0.000
ρ_{g2}	0.070
ρ_s	0.650
α'_{g1}	0.000
α'_{g2}	0.240
α'_s	0.161
τ_{gs}	0.121
ρ_{gs}	0.455
α_{gs}	0.424

Input Data

h_0	8.00
h_1	8.00
h_2	0.57
h_3	0.79
h_4	0.36
h_5	1.51
h_6	1.80
w_{cp}	1.90
T_i	1.00
T_o	1.00
I	1.00

Matrix Formulation

$$\left|\begin{array}{rrrrrr} 8.00 & 0.00 & 0.00 & 0.00 & 0.00 & 1.00 \\ 0.00 & 0.57 & -2.47 & 0.00 & 0.00 & 0.00 \\ -8.00 & 9.72 & -0.57 & 0.00 & -0.79 & 0.00 \\ 16.00 & -8.00 & 0.00 & 0.00 & 0.00 & 0.00 \\ 0.00 & -0.79 & -0.90 & -0.90 & 4.10 & 0.00 \\ 0.00 & 0.00 & 1.00 & -2.80 & 1.80 & 0.00 \end{array}\right| \begin{array}{l} T_{g1} \\ T_{g2} \\ T_{A1} \\ T_{A2} \\ T_s \\ CR \end{array} \left|\begin{array}{r} 8.4011 \\ -1.9000 \\ 0.6001 \\ 8.0000 \\ 1.6710 \\ 0.0000 \end{array}\right|$$

$$\left|\begin{array}{rrrrrr} 0.0000 & -0.0319 & 0.0935 & 0.1092 & 0.0210 & -0.0067 \\ 0.0000 & -0.0639 & 0.1870 & 0.0935 & 0.0419 & -0.0135 \\ 0.0000 & -0.4196 & 0.0432 & 0.0216 & 0.0097 & -0.0031 \\ 0.0000 & -0.2526 & 0.0520 & 0.0260 & 0.1942 & -0.4196 \\ 0.0000 & -0.1599 & 0.0569 & 0.0285 & 0.2967 & -0.0954 \\ 1.0000 & 0.2556 & -0.7479 & -0.8740 & -0.1678 & 0.0539 \end{array}\right| \begin{array}{r} 8.4011 \\ -1.9000 \\ 0.6001 \\ 8.0000 \\ 1.6710 \\ 0.0000 \end{array}\Bigg|$$

T_{g1}	1.03
T_{g2}	1.05
T_{A1}	1.01
T_{A2}	1.04
T_s	1.06
CR	0.19
N_i	0.46

Results

SC	0.36
F	0.32
$N\alpha_{sys}$	0.19
$N\alpha_{g1}$	0.07
$N\alpha_s$	0.13
N_s	0.79

Owens [23]

Material Properties

τ_{gl}	0.770
τ_s	0.150
α_{gl}	0.160
α_s	0.200
ρ_{gl}	0.070
ρ_s	0.650
SCSW	0.14
SCLW	0.23
SC	0.37

Input Data

h_i	8.90
h_e	22.72
U	3.72

Optical Properties

Φ0	1.00	Ψ0	0.47		
Φ1	0.81	Ψ1	0.52	A'1	0.24
Φ2	0.12			A'2	0.16

Matrix Formulation

$$\begin{vmatrix} 31.62 & -8.90 \\ -8.90 & 17.80 \end{vmatrix} \quad \begin{vmatrix} 0.2439 \\ 0.0000 \end{vmatrix}$$

$$\begin{vmatrix} 0.0368 & 0.0184 \\ 0.0184 & 0.0654 \end{vmatrix} \quad \begin{vmatrix} 0.2439 \\ 0.0000 \end{vmatrix} \qquad \begin{vmatrix} 0.0090 \\ 0.0045 \end{vmatrix}$$

Results

SC	0.37
F	0.32
$N\alpha_{sys}$	0.20
$N\alpha_{gl}$	0.04
$N\alpha_s$	0.16
N_s	1.00

Van Dyck et. al. [24]

Material Properties		**Results**	
τ_{gl}	0.770	SC	0.40
τ_s	0.150	F	0.35
α_{gl}	0.160	$N\alpha_{sys}$	0.23
α_s	0.200	$N\alpha_{gl}$	0.07
ρ_{gl}	0.070	$N\alpha_s$	0.16
ρ_s	0.650	N_s	0.99
α'_{gl}	0.240		
α'_s	0.161		
τ_{gs}	0.121		

Klems et. al. [10,13,28-32]

Material Properties		Results	
τ_{gl}	0.770	SC	0.35
τ_s	0.150	F	0.30
α_{gl}	0.160	$N\alpha_{sys}$	0.18
α_s	0.200	$N\alpha_{gl}$	0.05
ρ_{gl}	0.070	$N\alpha_s$	0.13
ρ_s	0.650	N_s	0.83
α'_{gl}	0.240		
α'_s	0.161		
τ_{gs}	0.121		

APPENDIX B
CALORIMETER CALIBRATION

B.1 Component Calibration

Full calibration was performed on all metered components of the calorimeter. Flow meters, thermocouples, and thermopiles were all analyzed. Voltage inputs into the DA system was also calibrated by the manufacturer. Calibration results have either been incorporated into data analysis spreadsheet, or directly within the QMON program.

B.1.1 Thermocouple / Thermopile Calibration

Type T copper-constantan thermocouples were used to measure temperatures in the system. Thermocouple correlation was based on data taken from the Omega temperature handbook [56]. To convert temperature into measured voltage (V), in mV,

$$V = -0.0012 + T(0.038619 + T(4.3656 \cdot 10^{-5} + T(-2.0671 \cdot 10^{-8}))) \qquad \text{(B.1)}$$

To convert a voltage to a temperature measurement (T)

$$T = -0.009 + V(25.8827 + V(-0.69646 + V(0.02613))) \qquad \text{(B.2)}$$

Thermopile voltage signals were calibrated in the form of gain amplifier corrections. For example: a voltage signal in the 8 mV range uses the 500 Gain amplifier. Calibration showed that this amplifier gives a gain of 503.3. Therefore, all voltage signals of this range have a slope of 0.9934. See the Sciemetrics calibration sheets, located in the Solar Laboratory, for details.

Thermocouples were calibrated using a precision temperature bath. Thermocouples were electrically isolated and immersed in a propylene glycol filled test tube. This was then immersed into the temperature bath. The bath was controlled to 10, 15, 17.5, 20, 22.5, 25, 30, 40, and 50 °C. Readings were recorded at 10 minute intervals after steady-state was achieved. The data was fit using a third order polynomial for the error in both temperature and voltage readings. Tables B-1 and B-1a shows this data and Figs. B-1 and B-2 show the data fit.

Table B-1. Calibration data for thermocouples.

Therm	10C	0.391mV	15C	0.589mV	17.5C	0.688mV	20C	0.789mV	22.5C	0.890mV
10	9.96	0.000388	14.98	0.000587	17.43	0.000685	19.97	0.000787	22.45	0.000887
11	9.98	0.000389	14.99	0.000587	17.47	0.000687	20.00	0.000789	22.42	0.000886
12	9.95	0.000387	14.94	0.000585	17.43	0.000685	19.97	0.000787	22.46	0.000888
13	9.98	0.000388	14.97	0.000587	17.43	0.000685	19.97	0.000787	22.44	0.000887
14	9.98	0.000388	14.94	0.000586	17.44	0.000685	19.97	0.000787	22.46	0.000888
15	9.98	0.000389	14.98	0.000587	17.43	0.000685	19.97	0.000787	22.45	0.000888
16	9.95	0.000387	14.94	0.000585	17.42	0.000685	19.93	0.000786	22.42	0.000887
17	9.95	0.000387	14.97	0.000586	17.46	0.000686	19.96	0.000787	22.45	0.000887
18	9.95	0.000387	14.97	0.000587	17.47	0.000687	19.96	0.000787	22.47	0.000888
19	9.97	0.000388	15.00	0.000588	17.47	0.000687	19.99	0.000788	22.48	0.000889
20	9.95	0.000387	14.97	0.000587	17.47	0.000687	19.95	0.000787	22.46	0.000888
Avg.	9.96	0.000388	14.97	0.000587	17.46	0.000686	19.97	0.000787	22.45	0.000888
Corr.	10.00	0.000389	15.00	0.000588	17.50	0.000688	20.00	0.000788	22.50	0.00089
Err.	0.04	0.000001	0.03	0.000001	0.04	0.000002	0.03	0.000001	0.05	0.000002

Table B-1a. Calibration data for thermocouples (continued).

Therm	25C	0.992mV	30C	1.196mV	40C	1.611mV	50C	2.035mV
10	24.90	0.000987	29.91	0.001192	39.93	0.001609	49.97	0.002035
11	24.93	0.000988	29.92	0.001193	39.93	0.001609	49.98	0.002035
12	24.90	0.000987	29.91	0.001192	39.93	0.001609	49.98	0.002035
13	24.90	0.000987	29.91	0.001193	39.93	0.001609	49.98	0.002035
14	24.90	0.000987	29.91	0.001193	39.93	0.001609	49.98	0.002035
15	24.90	0.000987	29.91	0.001193	39.93	0.001609	49.98	0.002035
16	24.87	0.000986	29.90	0.001192	39.93	0.001609	49.92	0.002033
17	24.92	0.000988	29.90	0.001192	39.93	0.001609	49.96	0.002035
18	24.92	0.000988	29.90	0.001192	39.93	0.001609	49.97	0.002035
19	24.92	0.000988	29.94	0.001194	39.93	0.001609	49.96	0.002035
20	24.90	0.000987	29.90	0.001192	39.93	0.001609	49.97	0.002035
Avg.	24.91	0.000987	29.91	0.001192	39.93	0.001609	49.97	0.002035
Corr.	25.00	0.000991	30.00	0.001196	40.00	0.001612	50.00	0.002036
Err.	0.09	0.000004	0.09	0.000004	0.07	0.000003	0.03	0.000001

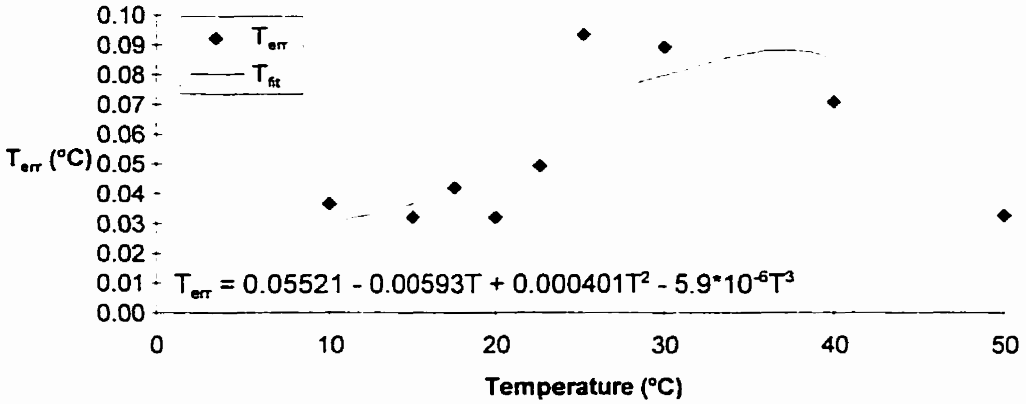

Figure B-1. Plot of thermocouple temperature calibration.

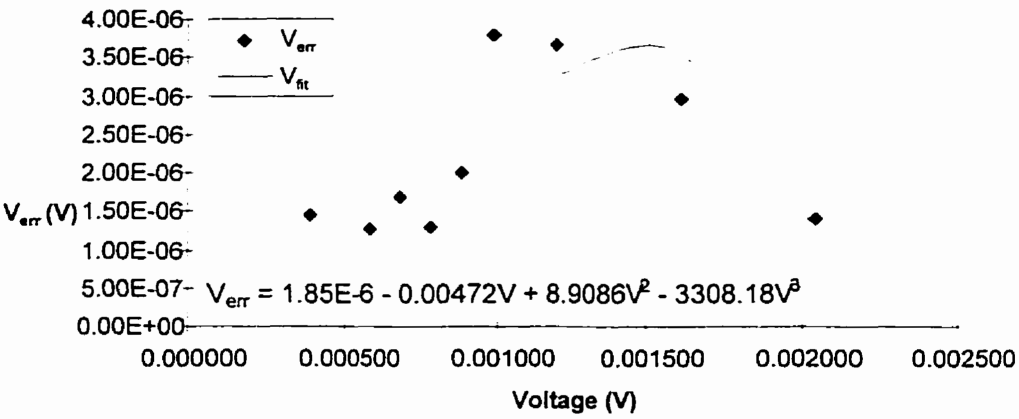

Figure B-2. Plot of thermocouple voltage signal calibration.

B.1.2 Flowmeter Calibration

The flow meter was calibrated using a gravimetric method. For the calibration test, the flowmeter was connected to a constant head tank filled with 30%/70% by volume propylene glycol and water. This was the proposed working fluid of the calorimeter. An amount of fluid was collected in a bucket, and then weighed to determine the exact volume using density data. The flowmeter was also connected to the data aquisition system which recorded the pulse output. Table B-2 shows this data. Figure B-3 shows the best fit.

Table B-2. Calibration data for flowmeter.

Test	Mass (kg)	Volume (L)	Pulse	Volume (fit) (L)	Error (%)
4kg	4.028	3.9126	36	3.879	0.86
5kg	5.03	4.8859	45	4.849	0.76
6kg	6.037	5.8640	54	5.819	0.77
7kg	7.013	6.8120	63	6.789	0.34
7.5kg	7.529	7.3133	68	7.328	0.20
8kg (slow)	8	7.7708	72	7.759	0.15
8kg	8.023	7.7931	73	7.867	0.01
8.5kg	8.59	8.3439	78	8.405	0.73

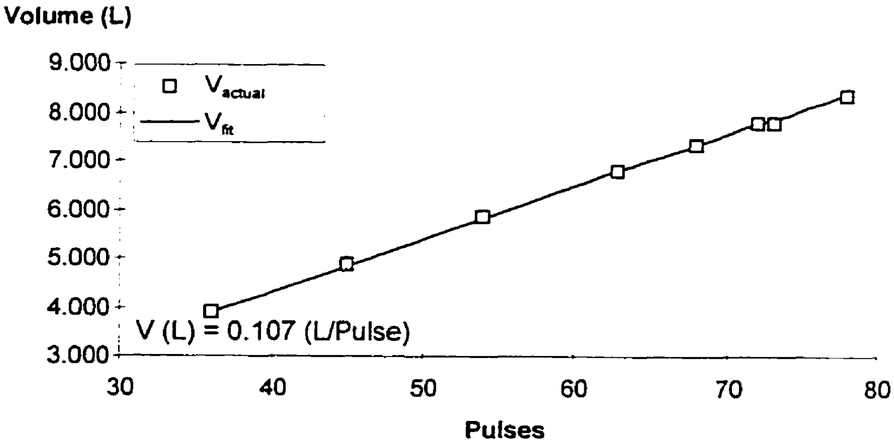

Figure B-3. Plot of best fit volume rate equation for flowmeter.

B.1.3 Pump / Fan Calibration

Power metering in the internal pump and fan requires calibration only in the DA system. These calibrations were implemented using the systems gain amplifiers as discussed in Section B.1.1.

B.1.4 Glycol Properties

Glycol Properties were determined using the Fluidfile™ program. Density and specific heat data was taken for a range from 0 to 30 °C using 30%/70% by volume propylene glycol and water. Table B-3 presents the data taken. Correlations are shown in Figs. B-4 and B-5.

Table B-3. Temperature effects on 30%/70% propylene glycol and water.

Temp	ρ (kg/m^3)	C_ρ (KJ/kgK)	ρ (kg/m^3) Fit	C_ρ (KJ/kgK) Fit
0	1037.40	3.793	1037.40	3.793
1	1037.05	3.796	1037.05	3.796
2	1036.70	3.799	1036.70	3.799
3	1036.34	3.802	1036.34	3.802
4	1035.98	3.804	1035.98	3.804
5	1035.61	3.807	1035.62	3.807
6	1035.24	3.810	1035.24	3.810
7	1034.89	3.813	1034.87	3.813
8	1034.48	3.815	1034.49	3.815
9	1034.10	3.818	1034.10	3.818
10	1033.71	3.821	1033.71	3.821
11	1033.31	3.824	1033.31	3.824
12	1032.91	3.826	1032.91	3.826
13	1032.50	3.829	1032.50	3.829
14	1032.09	3.832	1032.09	3.832
15	1031.67	3.835	1031.67	3.835
16	1031.25	3.837	1031.25	3.837
17	1030.82	3.840	1030.82	3.840
18	1030.38	3.843	1030.38	3.843
19	1029.95	3.846	1029.95	3.846
20	1029.50	3.848	1029.50	3.848
21	1029.05	3.851	1029.05	3.851
22	1028.60	3.854	1028.60	3.854
23	1028.14	3.857	1028.14	3.857
24	1027.68	3.859	1027.68	3.859
25	1027.21	3.862	1027.21	3.862
26	1026.74	3.865	1026.73	3.865
27	1026.26	3.868	1026.25	3.868
28	1025.77	3.870	1025.77	3.870
29	1025.28	3.873	1025.28	3.873
30	1024.79	3.876	1024.79	3.876

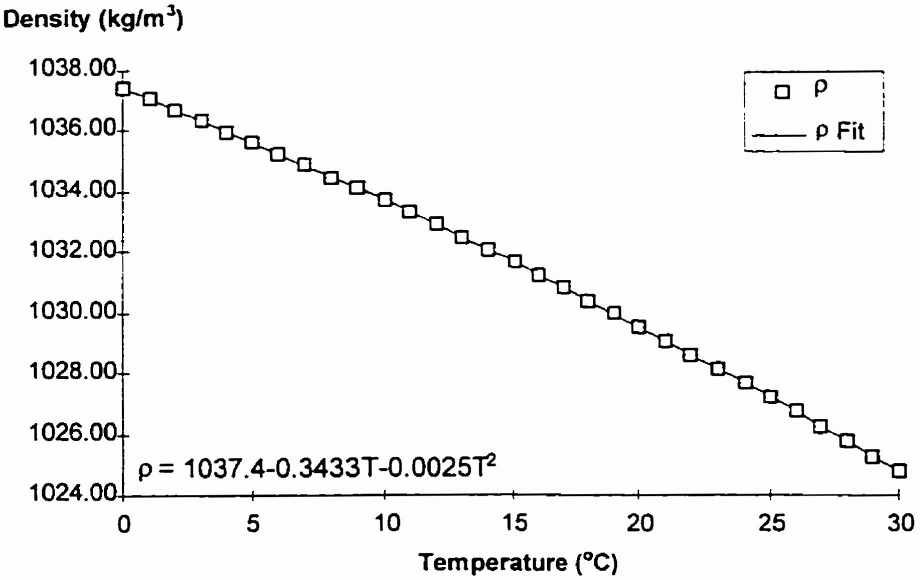

Figure B-4. Density-temperature relation in 30%/70% by volume propylene glycol and water.

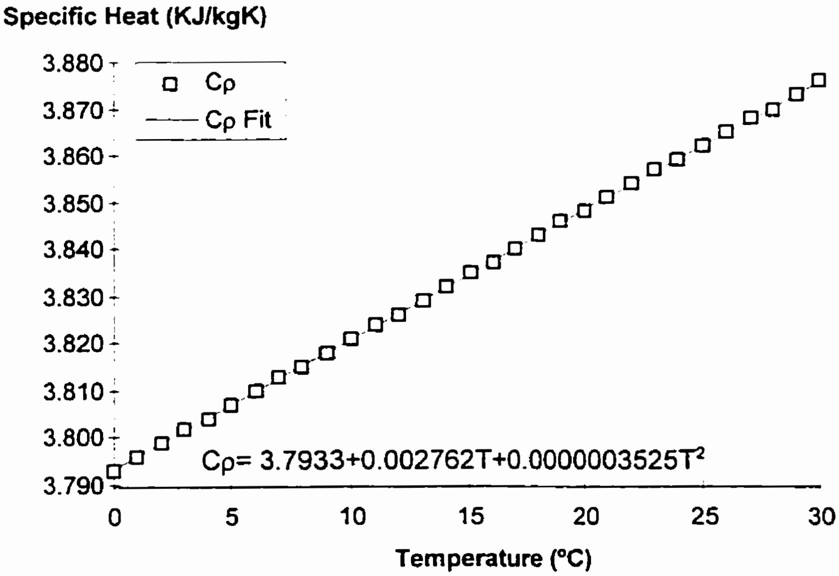

Figure B-5. Specific heat-temperature relation in 30%/70% by volume propylene glycol and water.

B.2 Test Cell Calibration

Calibration of the solar calorimeter was performed with the intent of determining running parameters, system performance, accuracy, and repeatability and reproducibility of results. A description and summary of these tests are as shown here.

The calibration test method is the same as that described in Section 3.5 with some minor exceptions: 1) the mask wall was installed without any mounted specimen. In this form, the wall would be highly insulated, and the geometry would be simple. Losses through a planer surface are more easily and accurately quantified than through a more complex surface. 2) energy input was provided through a series of heat lamps. Lamps were chosen because they would provide both radiative, and convective heat sources in the calorimeter. They were set to face the absorber panel so as to be representative of an irradiated sample scenario. By changing the bulbs, a test range of 50 to 600 W was easily achieved. It was felt that this range describes the range of absorbed energy found during testing.

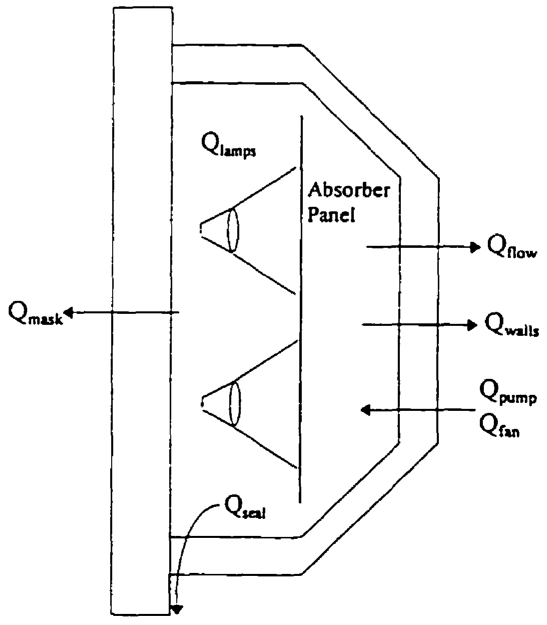

Figure B-6. Calorimeter calibration energy balance.

The error, E, in the system was determined by

$$E = Q_{flow} - Q_{pump} - Q_{fan} + Q_{loss} - Q_{lamps} \tag{B.3}$$

The calibration energy balance is shown in Fig. B-6.

B.2.1 Time Constant

Initial tests were run in order to determine the time constant or system response of the calorimeter. System response was needed to determine the time required to reach equilibrium for any given test.

The time constant, τ, is determined in the following manner. Thermal systems generally have 1st order characteristics. Common heat transfer theory for a 1st order system response [57] states that when the time after a step input equals the thermal time constant (τ_t) the calculated energy will have reached 63.2% of its full reading. This is determined by the equation

$$\frac{Q}{Q_{tot}} = 1 - \exp\left(-\frac{t}{\tau_t}\right) \tag{B.4}$$

when $t = \tau_t$

$$\frac{Q}{Q_{tot}} = 1 - \exp(-1) = 0.632 \tag{B.5}$$

In a similar manner, 5 time constants would be required to reach 99% of full reading.

Two different step inputs (about 300 and 400 W) were used, each with a heat up and cool down calculation of time constant. Input power was metered and compared with calculated power. The time taken to reach 63.2% of full scale was then determined from the data. An example of data taken can be seen in Fig. B-7.

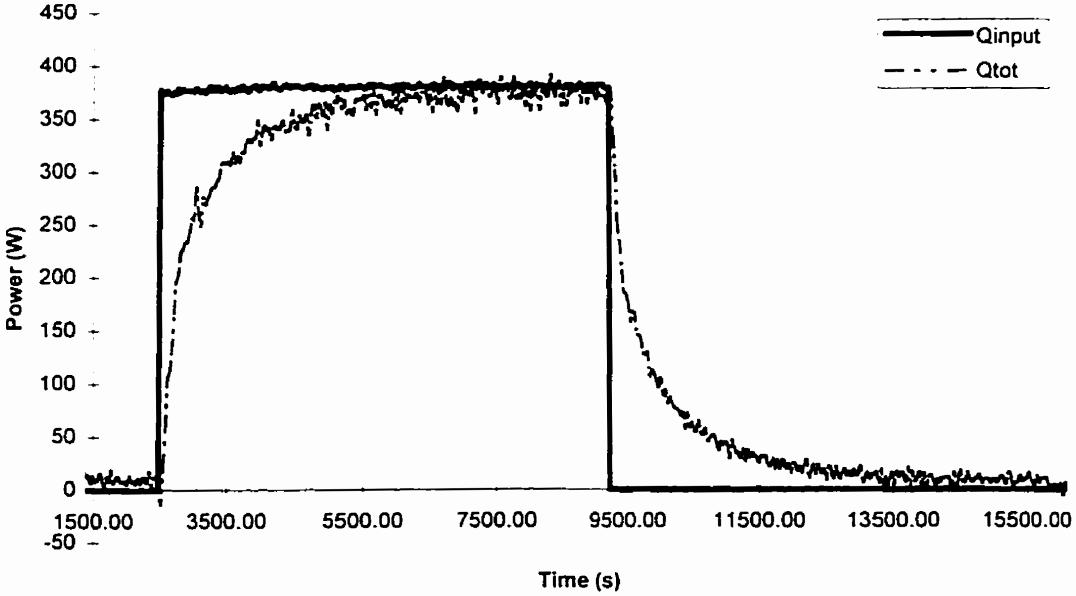

Figure B-7. Calorimeter response to step input.

The average time constant was calculated to be about 7.4 minutes for heating and cooling of the calorimeter. From this, 5 time constants would be about 37 minutes. Calculated time constants can be seen in Table B-4.

Table B-4. Calculated calorimeter time constants.

	Heat Up	Cool Down
380 W Step	7.1 min	7.9 min
287 W Step	7.2 min	7.3 min

B.2.3 Zero Loss Analysis

One series of tests was aimed at holding ambient conditions within the calorimeter under a range of power inputs. Such an analysis will reduce the loss term to a negligible quantity, and aid in the verification of the other metered systems. The range covered was 50, 100, 150, 200, 250, 300, 350, 400, 500, 550, and 600 W.

Based on the calculated time constant, each test setting was given about 45 minutes to reach steady state conditions. Data was then collected for an additional 75 minutes. Visual inspection of the data was performed to identify any trends in the measurements.

Figures B-8 and B-9 show the accuracy and calculated error and percent error of the results respectively. All of the results correlate well with actual inputs. As expected, the absolute error increases as the power input increases while percent error remains within a 2% region. Tests show that results are centered about zero.

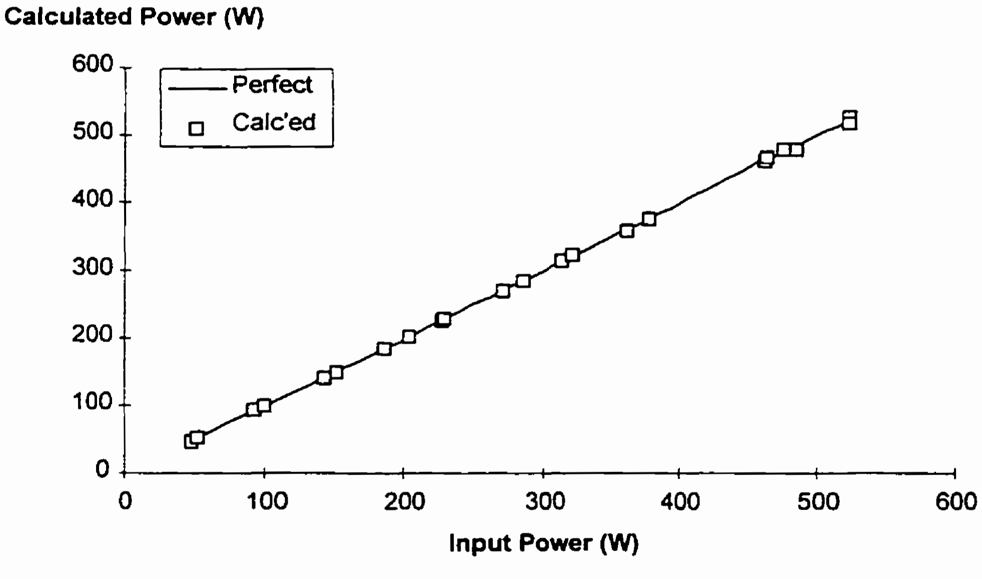

Figure B-8. Calorimeter test accuracy based on calibration data.

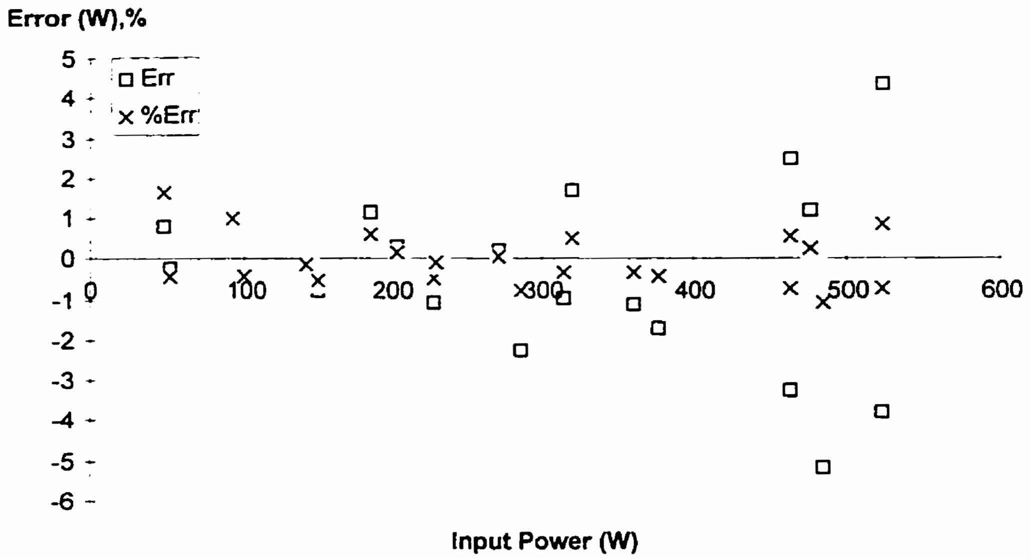

Figure B-9. Error in calorimeter data based on calibration results.

B.2.4 Loss Analysis

Losses exist in three areas: wall, mask, and seal losses. Wall losses are perhaps the smallest concern of the three types. The active thermal guard reduces heat flow through the walls to a negligible quantity. The mask is highly insulated and geometrically simple. Losses through it are easily determined using basic heat transfer theory. Seal losses occur at the connection of the mask wall with the calorimeter wall. Due to the geometry and construction of this area, it is a legitimate concern when determining losses. The effects of thermal bridging and heating from the ends of the active thermal guard make this area a necessary point of analysis.

Seal losses were estimated using the finite element analysis software ALGOR [58]. Table B-5 gives the results of the Analysis. The coefficient S was defined as the heat loss per meter length of seal (4.9 m total), per degree change in temperature. It was determined by dividing calculated flux by the associated temperature difference. Loss was then calculated by

$$Q = S \cdot L \cdot \Delta T \qquad \text{(B.6)}$$

Table B-5. Modeled seal losses within the calorimeter.

	Active Guard	No Guard
Q (W/m) @ΔT = 10 °C	0.20	0.50
S (W/mK)	0.02	0.05

A second test series was performed in order to examine temperature induced losses in the calorimeter. This series was the same as the 'zero loss' analysis with one exception: the temperature differences across the calorimeter walls were allowed to increase.

Figure B-10 shows how error increased as the temperature difference increased. Comparison of this data, with data taken from the first two test series, suggests that calculated error is temperature driven. Where this loss is occurring is unknown. The error fit shown in Fig. B-10 was incorporated into the data analysis spreadsheet.

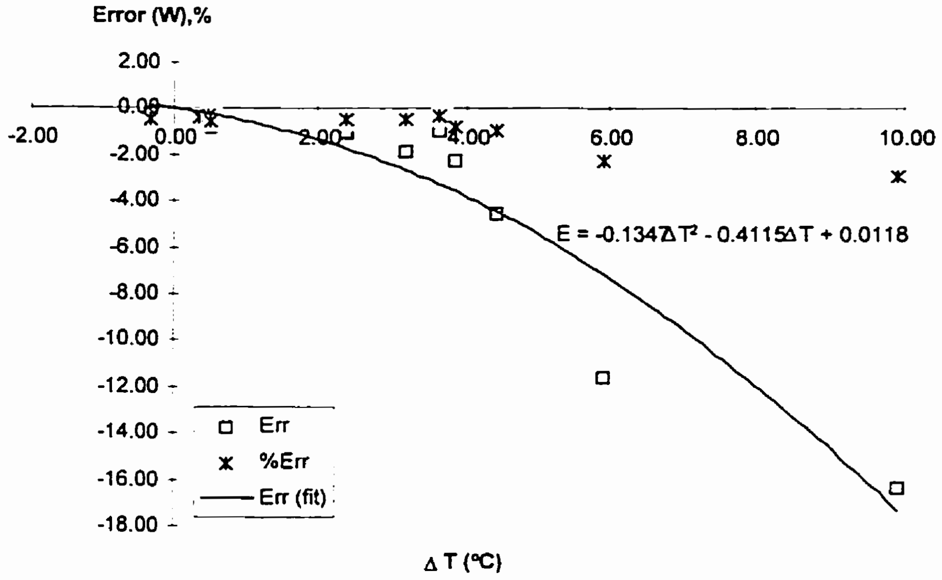

Figure B-10. Loss induced power measurement error.

B.2.5 Air Film Coefficient Test Setup

Interior and exterior air heat transfer coefficients are important variables in calorimetric analysis. Internal heat transfer coefficients are necessary as model input in the determination of losses. External values were calculated in order to determine the operating parameters of the wind generator. Fig. B-11 shows the basis of the following analysis.

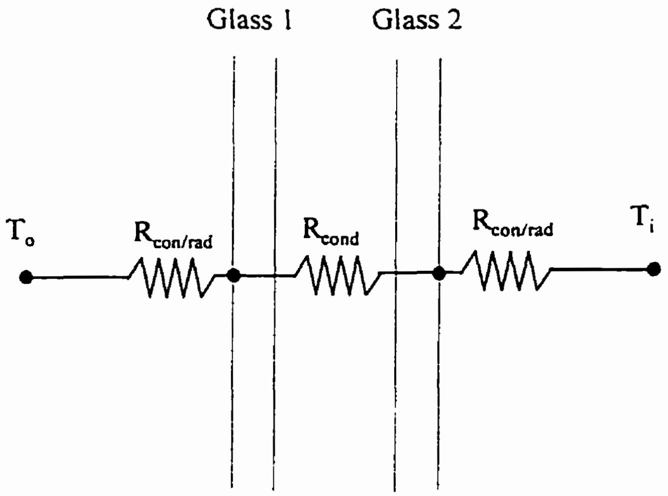

Figure B-11. Thermal circuit for calibration specimen.

Q_{spe}, as calculated in Eq. (3.12), is equal to the flow of heat to the interior surface of the specimen. Therefore

$$Q_{spe} = Q_{rad} + Q_{con} \tag{B.7}$$

and

$$Q_{rad} = F_{g2\_ap} \cdot \sigma \cdot A_{spe}(T_{ap}^4 - T_{g1}^4) \tag{B.8}$$

$$Q_{con} = D \cdot A_{spe}(T_h - T_{g1})^B \tag{B.9}$$

where D and B are calibration constants.

The radiant interchange factor was determined using the calorimeter geometry, emissivities (estimated at 0.84 for glass, and 0.96 for the absorber plate), and a program developed at the National Research Council [59]. It was estimated that F_{g2_ap} was approximately equal to 0.826.

Using the values determined by the previous equations, h_O, the interior film coefficient, f_i, h_{rad}, and h_{con} can be determined for a series of temperature gradients using

$$h_{rad} = \frac{Q_{rad}}{A_{spe}(T_{ap} - T_1)} \tag{B.10}$$

$$h_{con} = \frac{Q_{con}}{A_{spe}(T_i - T_1)} = D(T_i - T_1)^{B-1} \tag{B.11}$$

$$h_O = \frac{Q_{spe}}{(A_{spe}(T_2 - T_o))} \tag{B.12}$$

$$f_i = \frac{Q_{spe}}{(A_{spe}(T_i - T_1))} \tag{B.13}$$

For these tests, many systems did not need to be run or monitored. The active guard and all associated metering equipment were not used. In addition, flow metering was not necessary. Tests were performed using only the absorber plate for internal temperature control. Thermocouples metered the air temperature at six locations within the chamber. Two other thermocouples measured the absorber plate temperature.

Initial testing was performed to determine the internal heat transfer coefficient. This value is seen to be temperature dependent. Therefore, tests were performed over a number of temperature differentials. Ideal conditions would dictate that the interior of the calorimeter remain close to room temperature while the exterior air temperature was varied. The design of the calorimeter, however, made interior temperature manipulation easier to accomplish. Tests were run using a compromise of the two: room temperature was held in the calorimeter while an attempt was made to reduce the ambient temperature, interior temperature was increased relative to ambient conditions, and calorimeter temperature was increased while the ambient temperature was decreased.

The results of the first test series is shown in Fig. B-12. The radiative heat transfer coefficient remained relatively constant at 5.092 W/m^{2}K. The convective portion is calculated using Eq. (B.11) where B and D were calculated to be 1.348 and 0.628 respectively. The scatter in the low temperature region of the data was expected. The low temperature difference is directly responsible for high uncertainty in these numbers.

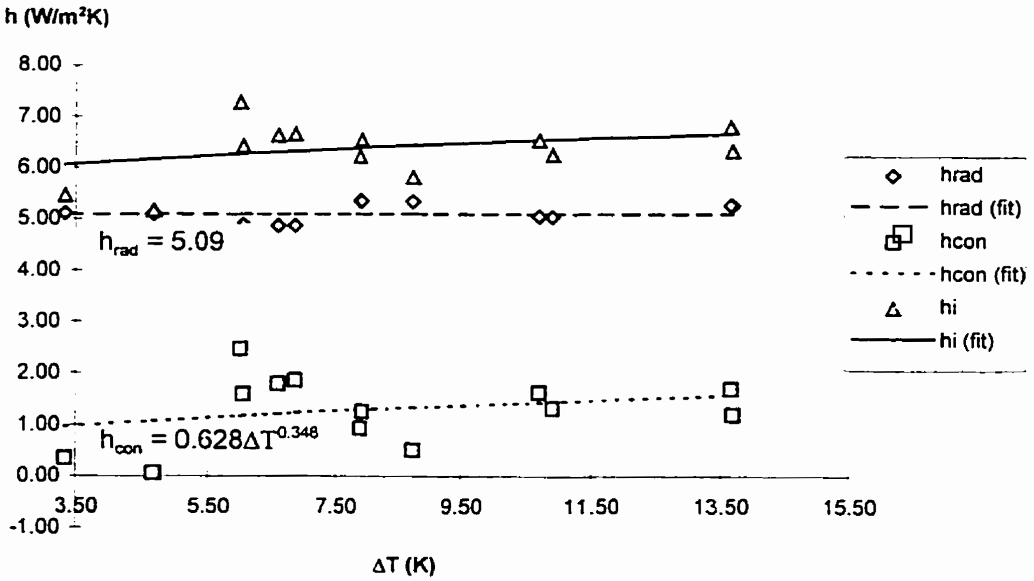

Figure B-12. Internal radiative and convective heat transfer coefficient results.

A series of tests were run in order to provided some values of the exterior air film coefficients as they correlate with fan input power. This data was used to help determine fan settings during testing. Tests were run using a large interior / exterior temperature difference to increase data accuracy and stability. The room was left at room temperature, while the calorimeter was heated to 35 °C. Table B-6 shows the approximate wind speed and air film coefficient as a function of input fan power.

Table B-6. Generated wind speeds and exterior air film coefficients based of fan input power.

Fan Power	20 Hz	30 Hz	40 Hz
Wind Speed (m/s)	≈ 3	≈ 5	≈ 7
Film Coeff. (W/m²K)	20.73	23.02	27.52

APPENDIX C
UNCERTAINTY ANALYSIS

C.1 General Notes on Uncertainty

Calculated results are often determined from combinations of values obtained from experimental measurements. Each primary measurement is subject to experimental error, taking into account such factors as instrument accuracy, etc. The primary errors in each measurement must be combined to calculate the uncertainty in the final result. To increase the accuracy of the final result, it is necessary to reduce the error in each component to an acceptable value.

Measurement error may be defined as the difference between the true value and the measured value of a quantity. The types of errors that occur in an experiment usually includes inaccurate readings, fixed errors or systematic errors, and random errors. Fixed errors will cause repeated readings to be in offset by a fixed amount. Random errors are created by electronic noise, or user interaction. The range of possible values the error might have is defined as the uncertainty of the measurement results [60].

Each measurement can be defined as the best estimate of the value for the variable plus the uncertainty interval of the measurement.

$$x_i = \overline{x_i} \pm \delta x_i \qquad \text{(C.1)}$$

where x_i is the variable, x_i is the best estimate of the variable, and δx_i is the uncertainty.

Uncertainty analysis was accomplished using a method presented by Kline and McClintock [52]. Assuming a function of independent variables $F(x_1,x_2,x_3\ldots)$, the uncertainty in F can be expressed as

$$\delta F = \pm\left[\left(\frac{\partial F}{\partial x_1}\delta x_1\right)^2 + \left(\frac{\partial F}{\partial x_2}\delta x_2\right)^2 + \ldots\ldots\left(\frac{\partial F}{\partial x_n}\delta x_n\right)^2\right]^{0.5} \qquad \text{(C.2)}$$

C.2 Inward-Flowing Fraction Uncertainty

An analysis was performed on each component of the energy balance in order to determine their uncertainties. This was then applied to the overall equation to find N_S and the uncertainty associated with it. A complete example can be seen in Appendix D.

For energy removed by the flow loop, we analyze the components of Eq. (C.3). The partial derivative of this equation with respect to each of its variables is given as Eqs. (C.3a-d).

$$Q_{flow} = m \cdot \rho \cdot C_p (T_{in} - T_{out}) \tag{C.3}$$

$$\frac{\partial Q_{flow}}{\partial m} = \rho \cdot C_p (T_{in} - T_{out}) \tag{C.3a}$$

$$\frac{\partial Q_{flow}}{\partial \rho} = m \cdot C_p (T_{in} - T_{out}) \tag{C.3b}$$

$$\frac{\partial Q_{flow}}{\partial C_p} = m \cdot \rho (T_{in} - T_{out}) \tag{C.3c}$$

$$\frac{\partial Q_{flow}}{\partial \Delta T} = m \cdot \rho \cdot C_p \tag{C.3d}$$

For energy added by the internal fans and pump, we consider Eq. (C.4). This equation represents the calculation of power using a voltage divider circuit. The partial derivative of this equation with respect to each of its variables is given as Eqs. (C.4a-e).

$$Q_{fan/pump} = R_A \cdot V_A \cdot V_S - R_S \cdot V_A^2 + R_B \cdot V_A \cdot V_S - \frac{R_S \cdot R_B \cdot V_A^2}{R_A} \tag{C.4}$$

$$\frac{\partial Q_{fan/pump}}{\partial R_A} = V_A \cdot V_S + \frac{R_S \cdot R_B \cdot V_A^2}{R_A^2} \tag{C.4a}$$

$$\frac{\partial Q_{fan/pump}}{\partial R_B} = V_A \cdot V_S - \frac{R_S \cdot V_A^2}{R_A} \tag{C.4b}$$

$$\frac{\partial Q_{fan/pump}}{\partial R_S} = -V_A^2 - \frac{R_B \cdot V_A^2}{R_A} \tag{C.4c}$$

$$\frac{\partial Q_{fan/pump}}{\partial V_A} = R_A \cdot V_S - 2R_S \cdot V_A + R_B \cdot V_S - \frac{2R_S \cdot R_B \cdot V_A}{R_A} \tag{C.4d}$$

$$\frac{\partial Q_{fan/pump}}{\partial V_S} = R_A \cdot V_A + R_B \cdot V_A \tag{C.4e}$$

Loss analysis involves more basic equations. For energy transfer through mask and the calorimeter walls, we analyze Eq. (C.5). The partial derivative of this equation with respect to each of its variables is given as Eqs. (C.5a-c).

$$Q = \frac{A \cdot \Delta T}{R} \tag{C.5}$$

$$\frac{\partial Q}{\partial A} = \frac{\Delta T}{R} \tag{C.5a}$$

$$\frac{\partial Q}{\partial \Delta T} = \frac{A}{R} \tag{C.5b}$$

$$\frac{\partial Q}{\partial R} = -\frac{A \cdot \Delta T}{R^2} \tag{C.5c}$$

Loss through the seal is given by Eq. (C.6) with Eq. (C.6a) representing its partial derivative.

$$Q_{seal} = 0.098 \cdot \Delta T \tag{C.6}$$

$$\frac{\partial Q_{seal}}{\partial \Delta T} = 0.098 \tag{C.6a}$$

The uncertainty of each variable and source from which each is estimated, are given in Table C-1.

All of these parts are then assembled to find the total uncertainty of the calculated inward-flowing fraction. Eq. (C.7) gives base equation, with its partial derivatives given as Eqs. (C.7a-d).

$$N_s = \frac{\left(Q_{flow} + \sum Q_{loss} - Q_{fan} - Q_{pump}\right)}{P_s} \tag{C.7}$$

$$\frac{\partial N_s}{\partial Q_{flow}} = \frac{1}{P_s} \tag{C.7a}$$

$$\frac{\partial N_s}{\partial Q_{loss}} = \frac{1}{P_s} \qquad \text{(C.7b)}$$

$$\frac{\partial N_s}{\partial Q_{fan/pump}} = \frac{-1}{P_s} \qquad \text{(C.7c)}$$

$$\frac{\partial N_s}{\partial P_s} = \frac{-\left(Q_{flow} + \sum Q_{loss} - Q_{fan} - Q_{pump}\right)}{P_s^2} \qquad \text{(C.7d)}$$

The uncertainty of each variable in these equations has been calculated using Eq. (C.2) and Eq. (C.3-6)

Table C-1. Variable Uncertainties

Variable	Uncertainty	Source of Uncertainty Estimate
δm	1.5%	Calibration results
$\delta \rho$	1%	Estimated using data sheet
δC_p	0.1%	Estimated using data sheet
$\delta \Delta T$	0.10°C[a]	Thermopile analysis
δR_A	0.016% + 2 counts	HP 3468A Digital Multimeter [61]
δR_B	0.016% + 2 counts	HP 3468A Digital Multimeter
δR_S	0.017% + 5 counts	HP 3468A Digital Multimeter
δV_A	0.1% + 2 digits	Calibrated DA system accuracy
δV_S	0.1% + 2 digits	Calibrated DA system accuracy
δA	0.03 m^2	Estimated using ±0.02 m in measured dimensions
δR (m^2K/W)	5%	Estimated based on knowledge of wall composition

[a] Thermopiles were calculated to ±0.03 °C. Increased to ±0.10 °C to account for fluctuations and thermal capacitance.

APPENDIX D
EXPERIMENTAL RESULTS

D.1 Example Data Set

Test #16 for a 45° slat angle was examined in Section 4.1. The full data set will be shown here.

Input Data - Steady State Conditions

Flow

Time	ΔTime	Pulse	ΔPulse	Flow
42100.66	0.00	1956	0	
42139.88	39.22	1961	5	0.0138
42179.15	39.27	1967	6	0.0165
42218.37	39.22	1972	5	0.0138
42257.64	39.27	1978	6	0.0165
42296.69	39.05	1983	5	0.0138
42335.8	39.11	1988	5	0.0138
42374.96	39.16	1994	6	0.0165
42414.01	39.05	1999	5	0.0138
42453.06	39.05	2005	6	0.0166
42492.55	39.49	2011	6	0.0164
42531.88	39.33	2016	5	0.0137
42571.1	39.22	2022	6	0.0165
42611.74	40.64	2027	5	0.0133
42650.96	39.22	2033	6	0.0165
42690.07	39.11	2038	5	0.0138
42729.45	39.38	2044	6	0.0165
42768.83	39.38	2049	5	0.0137
42808.21	39.38	2055	6	0.0165
42847.26	39.05	2061	6	0.0166
42886.31	39.05	2066	5	0.0138
42925.37	39.06	2071	5	0.0138
42964.64	39.27	2077	6	0.0165
43003.91	39.27	2082	5	0.0138
			Average	0.0151 L/s
T_{out}	25.90			0.9040 L/min
ΔT	1.51			
T_{avg}	25.15			
T_i	24.39			

Temperature

	Therm	Temp	Temp (cor)	ΔTemp
in air	T11	27.14	27.22	
in air	T12	28.58	28.65	
in air	T13	26.66	26.73	
in air	T14	27.12	27.19	
abs	T15	27.60	27.67	
abs	T16	26.25	26.31	
in mask	T17	25.89	25.96	
in mask	T18	28.85	28.93	
blind	T19	41.29	41.37	
blind	T20	38.12	38.20	
out air		21.70	21.76	
out mask		21.41	21.46	
out mask		22.18	22.24	
in win cen		33.96	34.04	
in win edg		32.81	32.89	
ot win cen		24.67	24.74	
ot win edg		25.88	25.95	
	T1		26.51	0.09
	T2		25.71	-0.10
	T3		26.11	0.03
	T4		26.51	-0.08
	T5		29.32	0.08
	T6		28.46	0.08
	T7		26.73	0.05
	T8		25.71	-0.31
	T9		26.18	0.60
	Average		26.81	0.05

Power

	V_l (V)	V_s (V)	Blind (W)
	3.5007	0.002784	1.2189
	3.464	0.002809	1.199
	3.4948	0.002803	1.2288
	3.5305	0.002785	1.2189
	3.4809	0.002807	1.2189
	3.5067	0.002807	1.2288
	3.469	0.002797	1.2189
	3.4908	0.002799	1.2189
	3.465	0.002782	1.209
	3.5276	0.002805	1.209
	3.4888	0.002807	1.209
	3.4938	0.002778	1.2288
	3.4938	0.002799	1.199
	3.469	0.002787	1.199
	3.464	0.002778	1.2189
	3.466	0.002807	1.2189
	3.4858	0.002795	1.209
	3.5296	0.002809	1.209
	3.5057	0.002805	1.2189
	3.5206	0.002789	1.209
	3.466	0.00278	1.199
	3.5305	0.002778	1.2189
	3.464	0.002803	1.209
	3.4978	0.002797	1.199
Average	3.491892	0.002795	121.3104

FLOW UNCERTAINTY

m =	1.51E-05 m^3/s	+/- 1.5% =	2.26E-07 m^3/s	Calibrated
ρ =	1027.19 kg/m^3	+/- 1% =	10.27187 kg/m^3	Data Sheet
$C\rho$ =	3862.97 J/kgK	+/- 0.1% =	3.862973 J/kgK	Data Sheet
ΔT =	1.51 °C	+/- 0.03 °C =	0.1 °C	Thermopile Analysis

Q_{flow}	$= m\rho C\rho \Delta T$	90.28
$\delta Q_{flow}/\delta m$	$= \rho C\rho \Delta T$	5991674
$\delta Q_{flow}/\delta r$	$= mC\rho \Delta T$	0.087888
$\delta Q_{flow}/\delta C\rho$	$= m\rho \Delta T$	0.02337
$\delta Q_{flow}/\delta \Delta T$	$= m\rho C\rho$	59.78654
w_{Qflow}	$= ((\delta Q_{flow}/\delta m * w_m)^2 + (\delta Q_{flow}/\delta r * w_\rho)^2 + (\delta Q_{flow}/\delta C\rho * w_{cp})^2$	
	$+(\delta Q_{flow}/\delta \Delta T * w_{\Delta t})^2)^{0.5}$	6.20

Flow Uncertainty	
w_{Qflow} =	6.20
uncertainty	6.86%

LOSS UNCERTAINTY

A =	3.401 m^2	+/- 0.03m^2 =	0.03 m^2	Measured
R =	1.27 m^2K/W	+/- 5% =	0.0635 m^2K/W	Measured
ΔT =	0.05 °C	1.98%	0.1 °C	Thermopile Analysis

Q_{loss}	$= A\Delta T/R$	0.024239
$\delta Q_{loss}/\delta A$	$= \Delta T/R$	0.068241
$\delta Q_{loss}/\delta R$	$= -A\Delta T/R^2$	-0.01909
$\delta Q_{loss}/\delta \Delta T$	$= A/R$	0.279685
w_{Qloss}	$= ((\delta Q_{loss}/\delta A * w_A)^2 + (\delta Q_{loss}/\delta R * w_R)^2 + (\delta Q_{loss}/\delta \Delta T * w_{\Delta T})^2)^{0.5}$	0.03

-0.0268	0.007225	-0.02354	0.019212	0.02552	0.024649
-0.07546	0.020341	-0.06627	0.063976	0.063976	0.042323
0.021105	-0.00569	0.018536	-0.01513	-0.02009	-0.01941
0.279685	0.279685	0.279685	0.236457	0.314094	0.458583
0.03	0.03	0.03	0.02	0.03	0.05
-0.09842	0.140889	0.668917	0.449569	3.072935	3.70359
-0.24672	0.46916	-2.39317	-3.97537		
0.077493	-0.11094	0.353974	0.587997		
0.314094	0.236457	0.14791	0.14791		
0.03	0.03	0.08	0.13		0.174345

Loss Uncertainty	
w_{Qloss} =	0.17
uncertainty	4.71%

POWER UNCERTAINTY

R_1 =	2001 W	0.016% + 2 counts =	0.36 W	HP 3468A Dig. Mult.
R_2 =	12020 W	0.016% + 2 counts =	2.16 W	HP 3468A Dig. Mult.
R_s=	0.010 W	0.017% + 5 counts =	0.000002 W	HP 3468A Dig. Mult.
V_1 =	3.492 V	+/- 0.1% + 0.001 V=	0.004492 V	Calibrated / DA acc.
V_s =	0.002795 V	+/- 0.1% + 0.000001 V=	3.8E-06 V	Calibrated / DA acc.

P	$= R_1V_1V_s - R_sV_1^2 + R_2V_1V_s - R_sR_2V_1^2/R_1$	6.80
$\delta P/\delta R_1$	$= V_1V_s + R_sR_2V_1^2/R_1^2$	0.010127
$\delta P/\delta R_2$	$= V_1V_s - R_sV_1^2/R_1$	0.0097
$\delta P/\delta R_s$	$= -V_1^2 - R_2V_1^2/R_1$	-61.0518
$\delta P/\delta V_1$	$= R_1V_s - 2R_sV_1 + R_2V_s - 2R_sR_2V_1/R_1$	38.70518
$\delta P/\delta V_s$	$= R_1V_1 + R_2V_1$	48959.81
w_P	$= ((\delta P/\delta R_1 * w_{R1})^2 + (\delta P/\delta R_2 * w_{R2})^2 + (\delta P/\delta R_s * w_{Rs})^2$	
	$+ (\delta P/\delta V_1 * w_{V1})^2 + (\delta P/\delta V_s * w_{Vs})^2)^{0.5}$	0.26

Power Uncertainty	
w_P =	0.26
uncertainty	3.76%

TEST UNCERTAINTY

Q_{flow} =	90.28 W	6.86%	6.20 W	Flow Analysis
P =	6.80 W	3.76%	0.26 W	Power Analysis
Q_{loss} =	3.64 W	4.80%	0.00 W	Loss Analysis
Q_{blind} =	121.31 W	1.00%	1.21 W	Power Analysis

N_i	$= (Q_{flow} - P + Q_{loss})/Q_{blind}$	0.72	0.77
$\delta N_i/\delta Q_{flow}$	$= 1/Q_{blind}$		0.008243
$\delta N_i/\delta P$	$= -1/Q_{blind}$		0.008243
$\delta N_i/\delta Q_{loss}$	$= 1/Q_{blind}$		0.008243
$\delta N_i/\delta Q_{blind}$	$= -(Q_{flow} - P + Q_{loss})/Q_{blind}^2$		-0.00592
w_{Qblind}	$= ((\delta N_i/\delta Q_{flow} * w_{Qflow})^2 + (\delta N_i/\delta P * w_p)^2 + (\delta N_i/\delta Q_{loss} * w_{Qloss})^2$		
	$+ (\delta Ni/\delta Q_{blind} * w_{Qblind})^2)^{0.5}$		0.05

Test Uncertainty	
w_{Qblind} =	0.05
uncertainty	7.19%

FILM DATA

			U_r g-b	U_r g-a	U_r b-a
air in	300.61				
air out	294.92		0.208193	0.06814	0.213966
absorber	300.15				
T_1^*	307.02	q_s		23.20	
T_2^*	298.09	T_b		312.95	
T_1	307.16				
T_2	297.95				

h_o
7.65

h_{g2_s}	h_{g2_ap}	h_{s_ap}	h_{g2_air}	h_{s_air}
3.79	1.16	3.76	-1.44	20.78

Q_{g2_s}	Q_{g2_ap}	Q_{s_ap}	Q_{g2_air}	Q_{s_air}
8.14	-3.03	-17.89	-3.51	95.28

D.2 Data Result Summary

-45° slat angle results

Test	P	ΔT	h_o	N_s	Err	h_{g2_b}	hr_{g2_ap}	hr_{s_ap}	h_{g2_air}	h_{s_air}
1	46.48	-0.98	22.45	0.87	0.13	3.46	1.10	3.49	-0.56	14.67
2	44.50	-0.26	18.82	0.88	0.18	3.44	1.09	3.48	-0.06	13.01
3	117.92	0.77	17.86	0.86	0.07	3.57	1.11	3.57	-1.02	24.53
4	197.04	1.77	14.81	0.85	0.04	3.73	1.13	3.69	-0.62	27.43
5	191.43	1.44	21.50	0.81	0.04	3.73	1.14	3.69	-0.84	26.55
6	54.20	4.93	19.51	0.68	0.15	3.59	1.14	3.65	-2.95	18.66
7	114.26	4.65	17.21	0.78	0.07	3.67	1.16	3.70	-2.44	31.00
8	123.40	4.40	19.87	0.73	0.07	3.71	1.16	3.73	-2.00	28.90
9	119.38	3.84	22.40	0.74	0.07	3.76	1.16	3.78	0.70	19.25
10	193.38	3.40	20.95	0.78	0.04	4.04	1.20	3.99	0.68	18.22
11	48.14	10.02	17.73	0.65	0.17	3.81	1.21	3.90	-3.56	12.02
12	46.78	9.11	23.20	0.51	0.18	3.80	1.20	3.89	-3.02	11.43
13	119.78	11.59	18.50	0.74	0.07	4.01	1.24	4.05	-1.85	18.59
14	192.31	8.80	15.23	0.80	0.04	4.01	1.24	3.92	-4.22	34.14
15	191.44	7.92	21.72	0.71	0.04	4.05	1.23	3.95	-3.52	27.92
16	114.54	5.74	1.51	0.78	0.06	3.73	1.16	3.74	0.72	25.84

0° slat angle results

Test	P	ΔT	h_o	N_s	Err	h_{g2_b}	hr_{g2_ap}	hr_{s_ap}	h_{g2_air}	h_{s_air}
1	44.09	-0.13	20.16	0.87	0.14	3.11	1.64	2.97	-0.64	13.39
2	48.01	-0.25	15.46	0.87	0.17	3.11	1.64	2.97	-0.28	14.21
3	121.18	0.94	17.44	0.86	0.07	3.32	1.69	3.11	-0.71	18.18
4	193.89	0.49	15.19	0.84	0.05	3.46	1.73	3.21	-1.10	23.75
5	189.82	0.05	19.12	0.83	0.05	3.45	1.73	3.22	-0.31	22.82
6	46.82	6.02	21.00	0.76	0.10	3.29	1.73	3.15	-1.28	11.26
7	122.63	5.15	22.50	0.85	0.07	3.43	1.75	3.23	-1.37	19.35
8	120.29	3.87	23.06	0.81	0.07	3.45	1.75	3.25	-0.65	17.11
9	115.22	3.92	35.35	0.80	0.07	3.43	1.75	3.23	-0.60	16.92
10	197.11	5.22	19.69	0.82	0.04	3.66	1.81	3.41	-0.46	19.72
11	47.07	11.07	15.60	0.73	0.19	3.44	1.81	3.33	-8.66	12.56
12	47.43	10.19	22.47	0.64	0.18	3.44	1.81	3.32	-6.60	12.17
13	123.10	10.21	19.52	0.79	0.07	3.61	1.85	3.43	-1.80	18.73
14	197.17	10.37	16.27	0.83	0.05	3.78	1.88	3.53	-1.64	21.79
15	202.61	9.85	22.56	0.78	0.04	3.81	1.88	3.56	-0.82	19.86
16	114.97	5.40	6.80	0.81	0.06	3.56	1.78	3.33	0.18	13.12

45° Slat Angle Results

Test	P	ΔT	h_o	N_s	Err	h_{g2_b}	hr_{g2_ap}	hr_{s_ap}	h_{g2_air}	h_{s_air}
1	48.30	-0.15	13.26	0.87	0.13	3.41	1.08	3.44	-0.06	17.31
2	49.66	-0.34	13.14	0.84	0.12	3.43	1.08	3.47	1.69	13.23
3	120.31	-0.73	30.17	0.81	0.07	3.59	1.10	3.56	-0.27	20.44
4	192.12	0.94	19.70	0.81	0.03	3.82	1.14	3.73	-0.53	21.91
5	193.01	0.17	27.15	0.81	0.03	3.81	1.13	3.73	0.11	20.93
6	52.49	4.87	20.52	0.64	0.13	3.63	1.14	3.68	-0.07	13.96
7	119.83	4.88	19.70	0.75	0.05	3.75	1.16	3.74	-1.51	20.90
8	119.82	5.15	21.23	0.72	0.05	3.77	1.16	3.76	-1.02	19.96
9	120.06	4.79	24.85	0.71	0.05	3.78	1.16	3.77	-0.46	18.76
10	191.27	6.59	18.83	0.75	0.03	3.96	1.18	3.90	-0.82	21.46
11	47.91	9.58	21.33	0.65	0.14	3.74	1.19	3.83	-3.69	13.26
12	47.51	9.12	23.17	0.51	0.14	3.74	1.18	3.83	-2.13	12.44
13	118.94	11.26	19.54	0.73	0.06	3.98	1.23	4.00	-1.83	19.23
14	197.22	11.04	16.31	0.77	0.04	4.18	1.25	4.12	-1.19	21.47
15	192.26	10.09	22.77	0.74	0.05	4.16	1.24	4.12	-0.31	19.75
16	121.31	5.69	7.65	0.78	0.05	3.79	1.16	3.76	-1.44	20.78

70° slat angle results

Test	P	ΔT	h_o	N_s	Err	h_{g2_b}	hr_{g2_ap}	hr_{s_ap}	h_{g2_air}	h_{s_air}
1	42.03	1.62	13.02	0.79	0.15	4.07	0.30	4.29	3.28	12.20
2	42.60	0.97	20.45	0.76	0.15	4.08	0.30	4.30	3.34	11.72
3	118.73	0.44	19.15	0.82	0.07	4.25	0.30	4.37	0.48	21.26
4	190.72	0.54	16.08	0.82	0.05	4.46	0.31	4.48	-0.43	24.14
5	192.95	-0.17	23.27	0.81	0.05	4.47	0.31	4.51	0.73	22.36
6	45.54	4.55	19.57	0.60	0.14	4.30	0.31	4.55	2.46	14.01
7	121.01	4.95	15.73	0.77	0.07	4.44	0.31	4.57	-0.80	21.79
8	120.56	4.56	19.35	0.75	0.07	4.44	0.31	4.57	-0.41	21.35
9	116.69	3.99	22.45	0.74	0.07	4.43	0.31	4.58	0.74	19.23
10	184.94	3.85	19.20	0.80	0.05	4.63	0.32	4.69	-0.35	23.44
11	45.58	9.75	16.71	0.65	0.17	4.48	0.33	4.78	-7.86	16.70
12	45.71	8.66	23.27	0.49	0.16	4.50	0.33	4.79	-0.03	13.30
13	122.27	10.35	18.82	0.71	0.07	4.68	0.33	4.87	-1.21	22.64
14	182.38	10.08	16.34	0.77	0.05	4.84	0.34	4.95	-1.31	25.58
15	180.03	9.21	21.80	0.72	0.05	4.82	0.34	4.95	-0.44	24.47
16	117.73	5.21	6.67	0.77	0.06	4.45	0.32	4.57	-0.83	22.05

IMAGE EVALUATION TEST TARGET (QA-3)

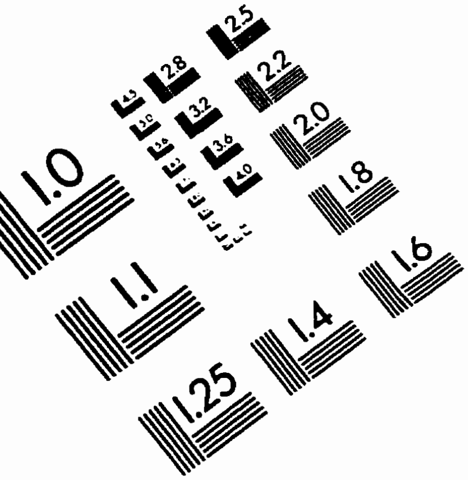

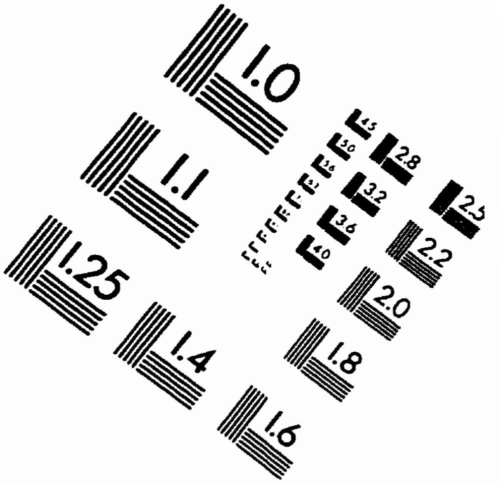

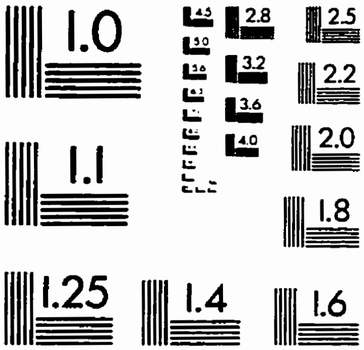

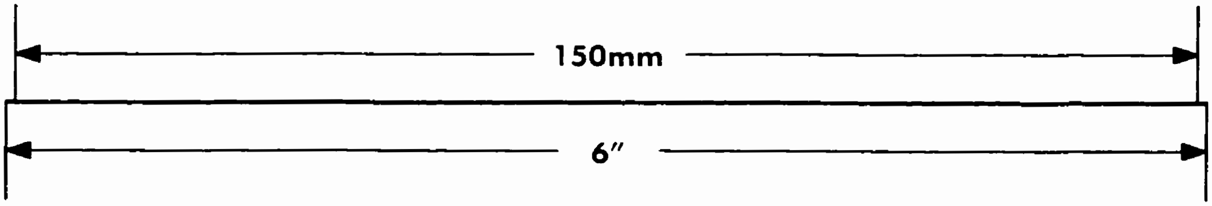

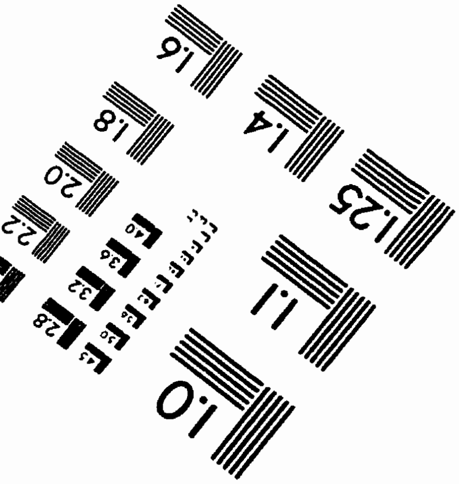

APPLIED IMAGE . Inc
1653 East Main Street
Rochester, NY 14609 USA
Phone: 716/482-0300
Fax: 716/288-5989